Leiden University Physics and Astronomy

Bachelor Research Project, February - July 2014

Towards a polarization-induced dOTF wavefront sensor

Author:
Martijn Simon Soen Liong Oei

Supervisors:
Dr. Matthew Kenworthy
Dr. Martin van Exter

Title page background:
Night sky stars revolve around the south celestial pole at the Southern African Large Telescope, Africa's *Giant Eye on the Universe*. This observatory is located on a hilltop in a nature reserve in North Cape Province, South Africa. One day, a polarization-induced dOTF wavefront sensor might be tested here.

Contact the author:

Martijn Oei
Leiden University
m.s.s.l.oei@umail.leidenuniv.nl

This document was published on: July 18, 2014

Contents

1 Introduction **3**
- 1.1 The problem of large ground-based telescopes . . . 3
- 1.2 Turbulence . . . 3
- 1.3 Adaptive optics . . . 4
- 1.4 Wavefront sensors . . . 4
- 1.5 Differential optical transfer function wavefront sensing . . . 4
  - 1.5.1 Merits . . . 5
  - 1.5.2 Astronomical application . . . 5
  - 1.5.3 Polarizing beamsplitter design . . . 5
- 1.6 Thesis outline . . . 5

2 Theory **6**
- 2.1 Complex amplitudes: from pupil to focal plane . . . 6
- 2.2 Complex amplitudes: the Airy disc . . . 7
- 2.3 Complex amplitudes: retrieving intensity and phase . . . 8
- 2.4 Intensity: the Airy disc . . . 8
- 2.5 Point spread functions . . . 9
- 2.6 Optical transfer functions . . . 10
- 2.7 Differential optical transfer function wavefront sensing . . . 10
  - 2.7.1 General dOTF WFS . . . 10
  - 2.7.2 Polarization-induced dOTF WFS . . . 11
- 2.8 Phase maps and wavefronts . . . 11
  - 2.8.1 Phase map: absolute value interpretation . . . 11
  - 2.8.2 Phase map: relative value interpretation . . . 11
  - 2.8.3 Difference between phase map and wavefront . . . 12
  - 2.8.4 From phase map to wavefront . . . 12
- 2.9 Wavefront flattening . . . 12

3 Simulations **14**
- 3.1 Simulating a point spread function . . . 14
  - 3.1.1 Creating the pupil plane amplitude map . . . 14
  - 3.1.2 Creating the pupil plane phase map . . . 17
  - 3.1.3 Creating the point spread function . . . 18
- 3.2 Simulating an electron map . . . 19
  - 3.2.1 From PSF to realization . . . 19
  - 3.2.2 Modelling thermal excitations . . . 20
- 3.3 Simulating a digital image . . . 20

3.3.1 From chip to circuit . . . 20
3.3.2 Bias . . . 20
3.3.3 Thermodynamic motion . . . 20
3.3.4 Amplification . . . 20
3.3.5 Read-out noise . . . 21
3.3.6 Digitization . . . 21
3.4 dOTF pupil plane phase map recovery . . . 21
3.4.1 Retrieving a raw dOTF PPPM . . . 22
3.4.2 Selecting a disk . . . 22
3.4.3 Aligning the maps . . . 22
3.5 dOTF pupil plane phase map quality . . . 23
3.5.1 The difference map . . . 23
3.5.2 Root mean square . . . 24
3.5.3 Phase wrapping . . . 24
3.6 Finding the best fixed obscuration radius . . . 26
3.6.1 General considerations . . . 26
3.6.2 Atmospheric wavefronts . . . 28
3.6.3 Bright star limit . . . 31
3.6.4 Dimmer star targets . . . 35
3.7 Adaptive dOTF wavefront sensing . . . 38
3.7.1 Adapting the obscuration radius as r_0 changes . . . 38
3.7.2 Adapting the obscuration radius for a given r_0 . . . 38
3.7.3 Quality estimation of a reconstruction . . . 40
3.7.4 Adaptive dOTF WFS algorithm . . . 41

4 Laboratory experiments **44**
4.1 Overview . . . 44
4.2 Imaging the Airy pattern . . . 44
4.2.1 Initial setup . . . 44
4.2.2 Outlining the setup . . . 46
4.2.3 Data reduction . . . 47
4.3 dOTF PPPM recovery: general . . . 51
4.3.1 Computing A_{dOTF} and ϕ_{dOTF} . . . 52
4.3.2 ϕ_{dOTF} gradient removal . . . 52
4.3.3 Finding the aperture center . . . 53
4.3.4 Obtaining the final ϕ_{dOTF} . . . 53
4.3.5 Validating the technique . . . 53
4.4 dOTF PPPM recovery: metal obscuration . . . 55
4.4.1 Focused setup . . . 55
4.4.2 Defocused setup . . . 56
4.5 dOTF PPPM recovery: rotating polarizer . . . 57
4.5.1 Rotating polarizer design . . . 57
4.5.2 High-speed dOTF wavefront sensing . . . 59
4.6 dOTF PPPM recovery: polarizing beamsplitter . . . 59
4.6.1 Setup . . . 61
4.6.2 Outlining the setup . . . 62
4.6.3 Reconstruction algorithm . . . 63
4.6.4 Results . . . 63

5 Future prospects **66**
5.1 Simulations . . . 66
5.2 Lab experiments . . . 67
5.3 Field experiments . . . 67

6 Summary and conclusion **69**
6.1 Main simulation results . . . 69
6.2 Main laboratory results . . . 70
6.3 Conclusions . . . 70

7 Acknowledgements **71**
7.1 People . . . 71
7.2 Software . . . 72

A Simulations of instrumental aberrations **73**

B Code library **77**
B.1 Simulations . . . 77
B.2 Laboratory experiments . . . 78

C List of abbreviations **80**

D List of mathematical symbols **82**

Chapter 1

Introduction

1.1 The problem of large ground-based telescopes

Exoplanet science is an important branch of contemporary astronomy. To probe deeper into planetary systems, it is desirable to have a high angular resolution telescope with a formidable light-collecting surface. In principle, both the angular resolution and the light-collecting capabilities of a telescope improve as its diameter increases. The intensity of a point source on the detector of an imaging device therefore ideally scales $\propto D^4$, where D is the telescope diameter. This is the reason that continuous efforts are made to build telescopes that dwarf current installations; the construction of the E-ELT in Chile is one of the most noticeable endeavors in this regard.

Unfortunately though, the performance of large ground-based telescopes is in all realistic situations limited by the atmosphere. Although large telescopes harvest more photons than smaller telescopes ($\propto D^2$), their angular resolution becomes independent of the aperture diameter and determined by atmospheric turbulence instead. Without any assistance, point sources emerge as diffuse speckles on the detector, and the telescope is heavily impaired in its capabilities.

1.2 Turbulence

Atmospheric turbulence is the chaotic merging of patches of air of different temperatures via convective heat transfer. This is a familiar phenomenon for everyone who's ever had experience working in a dusty room on a sunny day - particles can be seen floating gently in rotating streams of mixing air. Meteorologically, low-altitude turbulence arises from (among other factors) varying cloud coverage, differences in surface albedo, and the location-dependent angle between incident solar rays and Earth's surface. Huge temperature gradients are present in the atmosphere as a whole - from sea level to a height of 10 kilometers, temperatures fall off from about 15 °C to roughly -70 °C. Vicious winds introduce chaotic motions of air patches throughout the atmosphere.
These factors leave the air in a state of perpetual motion: temperature fluctuations are never completely ironed out. For understanding the basics of turbulence, we momentarily assume the (false) theory of geometrical optics. Hot patches of air have lower density than cold patches, and therefore also possess lower refractive indices. The refractive index of the atmosphere thus changes with position; and for every position, it changes with time, making it therefore appro-

priate to think of it as a function of the form $n(\mathbf{r}, t)$. We could take a snapshot of the refractive index function at some time t_0. Assume the existence of a star whose parallel rays arrive at the atmosphere at this moment, spread out over some area. Using Snell's law and knowledge of $n(\mathbf{r}, t_0)$ alone, we could in principe track the paths of these rays up to Earth's surface, where a telescope is busy observing the star. Some rays will end in the telescope aperture, while others will not. The rays entering the telescope will do so at slightly different incident angles. When performing the same ray tracing some moment later, say at t_1, the new atmosphere's refractive index structure $n(\mathbf{r}, t_1)$ will most likely give rise to another number of rays hitting the telescope and, for the ones doing so, the distribution of incident angles will differ from the distribution at t_0. It is straightforward to see in this way that the star's apparent brightness and position will change in time (the phenomena of *scintillation* and *image motion*, respectively).
Moreover, rays that arrived at the top of the atmosphere simultaneously will not all reach Earth's surface at the same instant due to variations in optical path length. By switching over to wave optics now, which reminds us that we can assign a phase value to all points in a light wave, it is easily seen that turbulence also leads to the reduction of the spatial coherence of the incoming wavefront. This effect is called *image blurring* or *seeing*. Due to the chaotic phase pattern that turbulence generates at the aperture of the telescope, constructive and destructive interference will lead our stellar point source to appear as a speckle pattern on the telescope's detector.

1.3 Adaptive optics

Adaptive optics (AO) systems provide partial correction for the seeing effects induced by the atmosphere. AO is the collective name for all technology employed in the effort to mitigate optical wavefront distortions that vary in time. [6] Adaptive optics can be roughly split up in two groups: devices that sense wavefront distortions, and technology that can correct them.
In this research, we will only consider wavefront sensors. Deformable mirrors, that play a critical role in modern-day aberration correction systems, are a whole story in their own right.

1.4 Wavefront sensors

To keep up with the changing state of the atmosphere, fast wavefront sensors are required. Ideally, the wavefront is sensed $\sim$ 1,000 times per second. For this reason, most wavefront sensors require bright stars to operate. It has turned out that it is not always possible to find a star that is luminous enough for wavefront sensing in the proximity of the science target of the main telescope. To remedy this, astronomers and engineers have built *laser beacons* or *laser guide stars*, which are employed to create artificial stars at a limited altitude in the night sky in cases where natural stars are not bright enough for the proper functioning of wavefront sensing instruments. These laser guide star systems are very expensive though and have problematic drawbacks, so other technologies for wavefront sensing (WFS) that do not rely on them are still of much interest.

1.5 Differential optical transfer function wavefront sensing

Differential optical transfer function wavefront sensing (dOTF WFS) might serve as an alternative to expensive WFS methods that require laser guide stars. dOTF WFS is a relatively new technique, that was first publicly described by Johanan Codona in 2012. [12] [13]

1.5.1 Merits

Apart from the photon efficiency of dOTF wavefront sensors, the approach has other advantages. One of the greatest strengths of dOTF WFS is its simplicity. Two images of the same source are made, where for one image the camera aperture is modified. Straightforward mathematical operations lead to a reconstruction of the wavefront. Due to this simplicity, the instruments might be inexpensive to fabricate. Also, as only a few components are necessary, compact commercial devices can be envisaged that could be used to detect wavefront aberrations in setups of optical laboratories.
It is also good to note that dOTF WFS can detect arbitrary phase aberrations - in stark contrast with some other wavefront sensing techniques.
Finally, another noteworthy feature is the potential of designs that contain no moving parts. This makes the device less prone to mechanical defects and wear.

1.5.2 Astronomical application

The eventual application of dOTF wavefront sensing would be to combine the power of thousands of these devices to perform wavefront sensing for a large telescope like the E-ELT. The dOTF sensors would circumvent the telescope, and all probe the wavefront of the telescope's cylindrical beam along a slightly different line-of-sight. The wavefront is subsequently reconstructed by solving a complex tomographic puzzle. As there are many redundancies in the data of thousands of dOTF wavefront sensors, it would not be a problem if some fraction of them would not be operating every night. Small, light-weight designs should make them easy to displace and transport.

1.5.3 Polarizing beamsplitter design

The specific design under interest in this research, is a configuration involving a polarizing beamsplitter. Apart from the static design, this approach allows for the simultaneous creation of the two images required for wavefront reconstruction.

1.6 Thesis outline

In this thesis, polarization-induced dOTF wavefront sensing is explored.

First, in Chapter 2, some pivotal physical concepts are explained on which the simulations and laboratory experiments rely.

Chapter 3 starts with a discussion detailing the generation of a point spread function, electron map and digital image. Then it is shown how two digital images can be used to reconstruct a wavefront. Next, the determination of the quality of such a reconstruction is assessed. The chapter is continued by the determination of the best obscuration radius for atmospheric wavefront sensing using the polarizing beamsplitter design. The results are established for observations with a bright target star. Next, the performance of dimmer target stars is evaluated for the identified best obscuration. Finally, adaptive dOTF WFS is discussed.

In Chapter 4, dOTF wavefront sensing with a metal obscuration is demonstrated. Then, dOTF wavefront sensing with rotating polarizers is described. Finally, a polarizing beamsplitter design is built and tested.

Chapter 2

Theory

Fourier optics is the branch of classical physics that studies the properties of light using Fourier analysis. With Fourier optics, the intensity (or flux) in the focal plane of an imaging instrument can be found given functions describing the amplitude and phase of the light waves in the pupil plane.

2.1 Complex amplitudes: from pupil to focal plane

Let us consider the simplest imaging instrument possible: light enters through a circular aperture, falls through a convex lens and a detector is placed in the thus created focal plane. We use a Cartesian coordinate system in which the z-axis coincides with the optical axis, so that the pupil plane and the focal plane are given by equations of the form $z = z_P$ and $z = z_F$, respectively. Let $\Psi_P(x, y)$ denote the complex amplitude in the pupil plane. This single-valued complex function of two variables is defined as

$$\Psi_P(x, y) \equiv A_P(x, y)e^{i\phi_P(x,y)} \tag{2.1}$$

Here, $A_P(x, y)$ represents the amplitude of the electric field and $\phi_P(x, y)$ the phase of the light wave, both in the pupil plane.
To find the complex amplitude in the focal plane, one just Fourier transforms Ψ_P.[1] In concreto,

$$\Psi_F(X, Y) = \mathscr{F}(\Psi_P(x, y)) = \int_{-\infty}^{\infty}\int_{-\infty}^{\infty} A_P(x, y)e^{i\phi_P(x,y)}e^{-2\pi i(xX+yY)}\mathrm{d}x\mathrm{d}y \tag{2.3}$$

[1] It is quite remarkable that the complex amplitude in the focal plane of a simple imaging system can be found just by Fourier transforming the complex amplitude in the pupil plane. We can regard the Fourier transform as the operator representing Fraunhofer diffraction in combination with the propagation of light waves through the convex lens. The fact that the complex amplitude in the pupil plane can also be fully recovered from the focal plane complex amplitude by means of an inverse Fourier transform, reflects the physical fact from optics that any path of light propagation can also be traced in the opposite direction. Mathematically, this is very straightforward:

$$\mathscr{F}^{-1}(\Psi_F) = \mathscr{F}^{-1}(\mathscr{F}(\Psi_P)) = \Psi_P \tag{2.2}$$

For light falling through a circular aperture, it is convenient to switch to polar coordinates to evaluate the integral. The coordinate transforms are simply

$$x = r\cos\theta \tag{2.4a}$$
$$y = r\sin\theta \tag{2.4b}$$
$$X = R\cos\Theta \tag{2.4c}$$
$$Y = R\sin\Theta \tag{2.4d}$$

Because the aperture has some finite radius r_P, $A_P(r,\theta) = 0$ for $r > r_P$. The focal plane complex amplitude therefore becomes

$$\Psi_F(R,\Theta) = \int_0^{2\pi}\int_0^{r_P} A_P(r,\theta)e^{i\phi_P(r,\theta)}e^{-2\pi i r R(\cos\theta\cos\Theta+\sin\theta\sin\Theta)}r\mathrm{d}r\mathrm{d}\theta \tag{2.5}$$

The expression in the exponent containing the goniometric functions can be simplified using the relation

$$\cos(\theta-\Theta) = \cos\theta\cos\Theta + \sin\theta\sin\Theta \tag{2.6}$$

Thus, the most developed expression for the focal plane complex amplitude without specifying $A_P(r,\theta)$ and $\phi_P(r,\theta)$ any further, is

$$\Psi_F(R,\Theta) = \int_0^{2\pi}\int_0^{r_P} A_P(r,\theta)e^{i\phi_P(r,\theta)}e^{-2\pi i r R\cos(\theta-\Theta)}r\mathrm{d}r\mathrm{d}\theta \tag{2.7}$$

2.2 Complex amplitudes: the Airy disc

The complex amplitude in the focal plane can be explicitly calculated for the idealized situation of a point source at infinity whose light waves are undisturbed before entering our imaging device. In this case, we can assume that A_P is constant over the aperture, so that $A_P(r,\theta) = A_P$ for $r < r_P$. Also, as the wavefront will be coherent, $\phi_P(r,\theta) = \phi_P$. The focal plane complex amplitude becomes in this particular situation

$$\Psi_F(R,\Theta) = A_P e^{i\phi_P}\int_0^{2\pi}\int_0^{r_P} e^{-2\pi i r R\cos(\theta-\Theta)}r\mathrm{d}r\mathrm{d}\theta \tag{2.8}$$

Then, by noting that the result of the integral will now be independent on the value of Θ, we can as well replace $\cos(\theta-\Theta)$ by $\cos\theta$. Also, $A_P e^{i\phi_P}$ represents the constant complex amplitude Ψ_P within the aperture, and this last symbol will be used in the following for notational simplicity. Thus, we obtain

$$\Psi_F(R) = \Psi_P\int_0^{2\pi}\int_0^{r_P} e^{-2\pi i r R\cos\theta}r\mathrm{d}r\mathrm{d}\theta \tag{2.9}$$

To proceed, Bessel functions are needed. The Bessel function of the first kind of order 0 is a symmetric complex single-valued function given by

$$J_0(u) = \frac{1}{2\pi}\int_0^{2\pi} e^{iu\cos(v)}\mathrm{d}v \tag{2.10}$$

Substituting this Bessel function in Equation 2.9, yields

$$\Psi_F(R) = 2\pi\Psi_P\int_0^{r_P} J_0(-2\pi r R)r\mathrm{d}r \tag{2.11}$$

To solve the integral, we perform the change of variables $\xi \equiv 2\pi rR$, and obtain

$$\Psi_F(R) = \frac{\Psi_P}{2\pi R^2} \int_0^{2\pi r_P R} J_0(\xi)\xi \mathrm{d}\xi \tag{2.12}$$

The various Bessel functions of the first kind are related by

$$\frac{\mathrm{d}}{\mathrm{d}u}(u^n J_n(u)) = u^n J_{n-1}(u) \tag{2.13}$$

We can obtain a useful expression for solving Equation 2.12 by setting $n = 1$ and taking a definite integral at both sides:

$$\tilde{u}J_1(\tilde{u}) = \int_0^{\tilde{u}} J_0(u)u\mathrm{d}u \tag{2.14}$$

Now we can advance Equation 2.12 to

$$\Psi_F(R) = S_P\Psi_P \frac{2J_1(2\pi r_P R)}{2\pi r_P R} \tag{2.15}$$

where $S_P \equiv \pi r_P^2$ has been introduced to denote the surface area of the pupil.

2.3 Complex amplitudes: retrieving intensity and phase

Once one has found an expression for the complex amplitudes in some plane (this can be the pupil plane as well), it is straightforward to find the corresponding intensity and phase patterns. Complex amplitudes are complex numbers, id est $\Psi \in \mathbb{C}$. Their positions in the Argand plane can be fully described by their distance from the origin (the *modulus*) and the angle subtended with the positive real axis in the counterclockwise direction (the *argument*).
The squared modulus of Ψ gives the intensity

$$I(R, \Theta) = |\Psi|^2 \tag{2.16}$$

Whilst the principle value of the argument of Ψ gives the reduced phase

$$\phi(R, \Theta) = \text{Arg } \Psi \tag{2.17}$$

2.4 Intensity: the Airy disc

The intensity of the Airy disc is called the Airy pattern and can be computed from Equation 2.15. Using $|\Psi_P|^2 = I_P$, and absorbing all constants in the focal plane peak intensity I_0, we obtain

$$I_F(R) = |\Psi_F(R)|^2 = I_0 |\frac{2J_1(2\pi r_P R)}{2\pi r_P R}|^2 \tag{2.18}$$

The Airy pattern represents the best possible focus of a point source on the detector of an imaging system and consists of several concentric rings that fall off rapidly in brightness. Exemplum gratia, the intensity maximum of the first ring is just 1.75% of the intensity at the center of the focal plane I_0, which is attained at $R = 0$. [5]
Although the Airy pattern, which is the result of diffraction at the aperture and subsequent interference, is a clear demonstration of the wave nature of light, the pattern can also be interpreted as a statistical distribution for photons. In concreto, given appropriate normalization the

Airy pattern is a probability density function (PDF) expressing for every coordinate pair in the focal plane the probability density that an arriving photon ends its trajectory there. The Airy pattern will be treated in this way in the next Chapter.

Due to the wave nature of light, the angular resolution $\Delta\theta$ of imaging systems like telescopes is limited: whenever multiple point sources are imaged, their Airy patterns will overlap, and it can become hard to find out which signal[2] originated from which source. Lord Rayleigh, a famous British physicist, once formulated a quantitative rule for the minimum angular distance between two point sources to still be regarded distinguishable from each other in the focal plane of an imaging system. This criterion, now known as the Rayleigh criterion, states that two point sources are just resolved when the Airy peak of one source coincides with a point in the first minimal intensity ring of the other source's Airy pattern.
It is important to remember that the distinguishability of two objects is a matter of taste, and therefore the Rayleigh criterion no more than an often-used convention to express the angular resolution of imaging systems. The Rayleigh criterion is

$$\Delta\theta = 1.220\frac{\lambda}{D} \tag{2.19}$$

where $D \equiv 2r_P$, the telescope's pupil diameter. The numerical factor of 1.220 originates from finding the first zero of the Bessel function J_1. For an object at infinity, geometrical optics yields us for the spatial resolution Δl

$$\Delta l = f \tan \Delta\theta \tag{2.20}$$

Under the paraxial approximation, where we regard $\Delta\theta$ to be small, the trigonometric function can be replaced by its first degree Maclaurin polynomial to obtain

$$\Delta l \approx f\Delta\theta \tag{2.21}$$

2.5 Point spread functions

Having examined the Airy pattern, which forms the basis of all focal plane intensity patterns that are generated in this research, it is time to introduce more general terminology.

The Point Spread Function (PSF) is defined in this research as the equivalent of the Airy pattern, but now for arbitrary pupil plane amplitude and phase maps. I follow a more general though often-used definition of the PSF here.
More concisely, the PSF is the statistical distribution for the photon flux (in photon numbers per unit area per unit time) at the focal plane of an imaging system at one specific instant in time. While this definition allows for the PSF to change over the period of integration, the eventual digital images will be generated in the simulations by assuming a static PSF during the whole exposure time.

The following algorithm can be used to find the PSF.

1. Start with functions for the pupil plane amplitude A_P and phase ϕ_P.
2. Compute the pupil plane complex amplitude Ψ_P ($\equiv A_P e^{i\phi_P}$).
3. Find the focal plane complex amplitude Ψ_F by Fourier transformation.

[2] Id est, the photons captured by the detector.

4. The PSF is now given by the square of the modulus of Ψ_F.

Mathematically, the PSF is thus given by

$$\text{PSF} \equiv |\mathscr{F}(A_P e^{i\phi_P})|^2 \tag{2.22}$$

2.6 Optical transfer functions

The optical transfer function (OTF) is defined as the Fourier transform of the PSF:

$$\text{OTF} \equiv \mathscr{F}(\text{PSF}) \tag{2.23}$$

Therefore, generally speaking, the OTF is a single-valued complex function of two variables. As it is a Fourier transform, which is an invertible operation, it contains the same information as the PSF.

2.7 Differential optical transfer function wavefront sensing

The mathematical principle behind differential optical transfer function wavefront sensing (dOTF WFS) has been extensively described before in various papers. [12][14][15] For this reason, only the relevant results will be discussed.

2.7.1 General dOTF WFS

dOTF WFS is based on recovering a large fraction of some pupil plane phase map ϕ_P by means of subtracting two slightly different OTFs from each other.
As discussed, OTFs are equally informative representations of PSFs, which are in turn generated by a pupil plane amplitude map and ϕ_P. To make the OTFs different from each other while using the same ϕ_P, one requires the two PSFs to be generated from two different pupil plane amplitude maps A_P and A'_P. We could define A_P as a regular aperture, e.g. representing just a circular hole in an otherwise opaque pupil plane. A'_P represents a slightly modified version of A_P, where an obscuration[3] is introduced to cut the pupil transmittance in a part of the aperture. The differential optical transfer function is defined by

$$\text{dOTF} \equiv \text{OTF} - \text{OTF}' \tag{2.24}$$

Or, in terms of A_P, A'_P and ϕ_P,

$$\text{dOTF} = \mathscr{F}|\mathscr{F}(A_P e^{i\phi_P})|^2 - \mathscr{F}|\mathscr{F}(A'_P e^{i\phi_P})|^2 \tag{2.25}$$

Logically, as the OTF is a single-valued complex function of two variables, the dOTF is as well.

It is now claimed that the dOTF is a function that approximates the pupil plane complex amplitude Ψ_P. If this is true, then it is not hard to accept that A_{dOTF} and ϕ_{dOTF}, defined by

$$A_{\text{dOTF}} \equiv |\text{dOTF}| \tag{2.26a}$$

$$\phi_{\text{dOTF}} \equiv \text{Arg dOTF} \tag{2.26b}$$

will be, in some sense, approximations of A_P and ϕ_P respectively.

[3] This obscuration is sometimes also called a *diversity*.

2.7.2 Polarization-induced dOTF WFS

The two designs that are of particular interest in this research are based on the polarization property of light. The polarization direction of a light wave is the direction that the electric field oscillates in.
Polarizers are optical devices from which only light waves with a certain polarization direction can emerge. By making clever use of polarizers and polarizing material, we might be able to build robust dOTF wavefront sensors. Their operation principle is based on Malus's Law:

$$I = I_0 \cos^2 \theta \tag{2.27}$$

where I_0 and I represent the intensity of the light waves before and after they come across a polarizer, respectively. θ is the initial angle between the polarization direction of the light waves and the polarizer direction.
For example, when considering light waves whose electric field vectors make an angle $\theta = \frac{\pi}{4}$ rad with the polarizer direction, Malus's Law tells us that $I = \frac{1}{2} I_0$.

Unpolarized light generally is an equal mixture of linearly polarized light of all polarization directions. The intensity left after unpolarized light passes a polarizer, is therefore given by multiplying the original intensity by the average $\langle \cos^2 \theta \rangle$:

$$I = I_0 \langle \cos^2 \theta \rangle = I_0 \int_0^{\pi} cos^2\theta \rho(\theta) \mathrm{d}\theta = I_0 \int_0^{\pi} \frac{1}{\pi} cos^2\theta \mathrm{d}\theta = \frac{1}{2} I_0 \tag{2.28}$$

Here $\rho(\theta)\mathrm{d}\theta$ represents the infinitesimal probability that the polarization direction of a wave in the incoming unpolarized light beam makes an angle $\in [\theta, \theta + \mathrm{d}\theta]$ with the transmission direction of the polarizer. We can conclude that half the intensity is lost by passing through the device and that the remaining light is now linearly polarized in the polarizer direction.

2.8 Phase maps and wavefronts

2.8.1 Phase map: absolute value interpretation

The phase map for a certain plane denotes for each position in this plane the local phase value of the light wave that passes through it. As one might note, this phase value varies very quickly in time: at a fixed point in space, the number of oscillations of the electric and magnetic field per unit time is given by $\nu = \frac{c}{\lambda}$, which yields frequencies in the order of 10^{14} Hz for optical wavelengths. As each oscillation corresponds to a phase increase of 2π rad, the angular frequency (loosely 'the number of radians swept through in a second') therefore equals $2\pi\nu$ rad, and so is very large.
It would therefore be correct to say that any time-independent phase map $\phi(x, y) \in [0, 2\pi \text{ rad}\rangle$ will only give the correct phase values in the plane during a single infinitesimal time step of every oscillation. These moments of correctness are logically $\frac{1}{\nu}$ separated in time.

2.8.2 Phase map: relative value interpretation

For our purposes though, the concept of absolute phase is unimportant, as the PSF generated by light waves is independent of global phase shifts.[4] We are thus only interested in phase

[4] These phase shifts, which amount to adding the same constant phase value to all existing phase values, are often called *pistons*. Physically, a phase map undergoing a piston yields the absolute phase map at the same plane for constant wave disturbances at a later (or earlier) moment in time.

differences between points. Luckily, $\phi(x, y)$ can also be understood as giving for each point the relative phase value with respect to an arbitrary reference point in the map. If we limit our scope to monochromatic light waves only, the angular frequency at each location on the map is equal. This means that the increase of phase at each point of the plane occurs at the same pace, resulting in time-independent relative phase values - unless the phase disturbances induced by the atmosphere or imaging optics undergo a temporal change, of course.

2.8.3 Difference between phase map and wavefront

If we want to be accurate, we should distinguish the concepts of phase maps and wavefronts from each other. The night sky is filled with electromagnetic radiation and thus we can attribute a phase value $\phi(x, y, z)$ to every point of it. A phase map generally gives different phase values at one slice through three-dimensional space, while a wavefront is the locus of points of a given constant phase - generally a curved surface in $\mathbb{R}^3$. As their mathematical descriptions differ from each other only by a fixed scaling factor, 'phase map' and 'wavefront' are often used in natural language as if they were interchangeable, just like people tend to use 'frequency' and 'angular frequency' as synonyms.

2.8.4 From phase map to wavefront

If $\phi(x, y)$ is determined at a plane perpendicular to the Poynting vector[5], the wavefront is found readily. Let the z-direction coincide with the direction of the Poynting vector, so that the plane under interest is given by $z = z_0$. Suppose e.g. we want to construct the surface containing all points with phase $\phi = 0$, the value attained in the reference point of the relative phase map. Now consider the phase $\phi(x, y) \in [0, 2\pi \text{ rad}\rangle$ at some other point (x, y) in the plane. This phase value is generally larger than 0. To find the point (x, y, z) where the phase is 0, we should trace the light wave in the opposite direction of the Poynting vector for $\frac{\phi(x,y)}{2\pi}$ oscillations. As every oscillation corresponds to a spatial distance of wavelength λ, we conclude that the wavefront for $\phi = 0$ is given by

$$z_W(x, y) = -\frac{\phi(x, y)}{2\pi}\lambda = -\frac{1}{k}\phi(x, y) \tag{2.29}$$

where k is the magnitude of the wave vector. Wavefronts for other phase values are obtained by the addition of a constant. We assume here that the wavefront shape remains constant in the z-direction.

2.9 Wavefront flattening

Once a phase map $\phi(x, y)$ has been measured and the wavefront $z_W(x, y)$ computed, flexible mirrors are used to flatten the wavefront. Suppose this sheet of reflective material is installed in the plane of $\phi(x, y)$, so that the mirror surface coincides with it whenever the adaptive optics system is disabled.[6] Then the surface of the mirror should be given by

$$z_M(x, y) = \frac{1}{2}z_W(x, y) = -\frac{1}{2k}\phi(x, y) \tag{2.30}$$

[5] The Poynting vector points in the direction of propagation of electromagnetic energy. It is defined by $\vec{S} \equiv \frac{1}{\mu_0}\vec{E} \times \vec{B}$.

[6] When no adaptive optics technology is used to reduce atmospheric effects, astronomers tend to say they look at the 'open atmosphere'.

The mirror surface follows the contours of the wavefront, to make sure that wavefront points spatially further along the optical axis have to travel a longer distance to a point on the mirror. The light travels back in the same direction as it came from, so any additional distance these points travel, counts twice. By introducing the factor $\frac{1}{2}$, the initially curved wavefront $z_W(x, y)$ is turned into a flat surface, under ideal circumstances.

The flatness of the outgoing wavefront is therefore limited by our ability to

1. accurately measure $\phi(x, y)$, and
2. build wavefront correcting optics like flexible mirrors.

In the simulations, it will be inquired to what degree the quality of dOTF-reconstructed pupil plane phase maps limits the attainable wavefront flattening. In this way, I assume that the dOTF wavefront sensor comes with perfect wavefront correcting optics.

Chapter 3

Simulations

The first necessary step to analyse the quality of an image-based wavefront sensing technique, is the ability to generate digital images from a given parameter set. Therefore, in the coming sections, a description will follow how the digital images - the output of CCD- or CMOS-detectors - have been quantitatively simulated.[1]

First, it will be discussed how from pupil plane amplitude and phase maps the point spread function (PSF) can be obtained.[2] Then I explain how from the PSF a realization of an electron-filled detector chip can be obtained. Lastly, I will describe the steps that lead from an electron map to a digital image.

3.1 Simulating a point spread function

As outlined in the preceding theory chapter, the PSF can be generated using a pupil plane amplitude map (PPAM) and phase map (PPPM). The regular aperture will be denoted by $A_P(x, y)$, the obscured aperture with $A'_P(x, y)$ and the phase by $\phi_P(x, y)$.

3.1.1 Creating the pupil plane amplitude map

The regular aperture A_P is represented by a two-dimensional array[3] of M rows and N columns containing the value of 0 outside the aperture, and 1 inside the aperture. The aperture is modelled as a disk of some radius r_P centered on the middle of the map. To model A'_P, the pupil with diversity, a disk-shaped region of radius r_O on the edge of the aperture was obscured.

Creating the aperture

An even number of rows can be split up in two groups of equal size. Now add one row - the subdivision in two equally sized parts becomes impossible. A central row remains. Therefore, only when both M and N are odd (so that there is a central row *and* a central column) the map has a definite central pixel. It is readily verified that in all of the other geometries (M odd and

[1] All code for the simulations was written in Python 2.7. See `python.org` for more information on this increasingly popular programming language.

[2] Under a 'map', I understand any real single-valued function of two variables, so that the function can be represented graphically by a color image or height profile.

[3] We will use the word *pixel* as a synonym for an array element.

N even, M even and N odd and both M and N even), no such central pixel exists.
However, this does not have to be a problem for generating a circular aperture that lies exactly in the middle of the map. Suppose we designate the index numbers $0, 1, \ldots, M-1$ to the rows and $0, 1, \ldots, N-1$ to the columns. In terms of these index numbers, the coordinates of the center of the map are

$$x_C = \frac{N-1}{2} \tag{3.1a}$$

$$y_C = \frac{M-1}{2} \tag{3.1b}$$

Note that x_C and y_C are integers only for even M and N.
For reasons that become clear in a moment, we must differentiate between the map center (x_C, y_C) and the pupil center (x_P, y_P). For now, let these two points coincide: $(x_P, y_P) = (x_C, y_C)$.

The mathematical prescription for A_P is

$$r(x,y) = \sqrt{(x-x_P)^2 + (y-y_P)^2} \tag{3.2a}$$

$$A_P(x,y) = \begin{cases} 1 & \text{if } r(x,y) < r_P \\ 0 & \text{if } r(x,y) \geqslant r_P \end{cases} \tag{3.2b}$$

In the simulations, x and y are integers, as they represent pixel index numbers.[4]

Also without a central pixel, e.g. when M and N are both even, the aperture disk extends symmetrically over all four quadrants of the map. In that case, x_P and y_P are half-integers, and the four pixels with coordinates $(x_P \pm \frac{1}{2}, y_P \pm \frac{1}{2})$ circumvent the pupil center (x_P, y_P). Their distance to the pupil center is equal (namely, $r(x_P \pm \frac{1}{2}, y_P \pm \frac{1}{2}) = \frac{1}{2}\sqrt{2}$), so they collectively lie within the aperture or outside of it. By extending this line of reasoning, it can be glanced that the four quadrants of A_P are exactly the same if they were rotated by multiples of $\frac{\pi}{2}$ radians to match: if the pixel $(x_P + a, y_P + b)$ in the first quadrant lies within the aperture, so does $(x_P - b, y_P + a)$, $(x_P - a, y_P - b)$ and $(x_P + b, y_P - a)$ in the second, third and fourth quadrant, respectively.

Shifting the aperture

As outlined in the theory Chapter, the focal plane complex amplitude will be found by Fourier transforming the pupil plane complex amplitude. `NumPy`, a `Python` package for scientific computing, can perform the required discrete Fourier transform (DFT) by means of an efficient algorithm called fast Fourier transform (FFT). To prepare A_P for the DFT, `NumPy` requires that the aperture center lies at the origin $\mathcal{O}$ of the map - id est, the pixel with index numbers $(0, 0)$.

- For odd M and N, the aperture has a central pixel, and the map can be shifted accordingly. During the process of shifting, rows and columns disappear at one side of the map and

[4] Equation 3.2 shows my choice to exclude pixels from the aperture that lie exactly on a distance r_P from (x_P, y_P). At first sight, one could equally well argue that pixels on the edge of the aperture should be included instead. In reality this is a non-issue of course, but due to the quantization of space in digital computers (*pixellation*), we have to make a choice. Incorporating borderline pixels into the pupil disk has the consequence that an aperture radius of 0 pixels would still give rise to a single translucent pixel. As this might seem confusing, I decided to settle on excluding borderline cases from the aperture. The same convention is used in defining the obscuration in Equation 3.3.

reappear at the other. The result is a map that could be repeated in a tile grid suitable for periodic boundary conditions, while having an aperture centered at $\mathscr{O}$.

- For even M and N, the aperture cannot have a central pixel if it is required to lie exactly at the center of the map. This means that no appropriate shift exists to prepare the map for the DFT. Therefore, if one would like to use even dimensions for the PPAM, the aperture should not be created at the map center, but at one of the pixels that surround it.[5] This is not a problem though - there is no physical requirement that the aperture should be located at the map center.

The intermediate conclusion is that both even and odd map dimensions are allowed as long as the aperture center is a definite pixel.

The aperture radius

Under the aforementioned condition of integer coordinates (x_P, y_P), the diameter measured along the x- and y-axis will be an odd number of pixels regardless of the value of the aperture radius.[6] The diameter measured along any other axis is ill-determined due to the pixellated structure of the simulated PPAM.
r_P is thus unconstrained, and can be either an integer or a float.

Introducing the obscuration

To do dOTF wavefront sensing, it should also be possible in the simulations to add an obscuration to A_P to obtain A'_P, the modified PPAM. The obscuration that is used in my simulations is disk-shaped, whose center (x_O, y_O) lies on the edge of the aperture. In principle, as the aperture is radially symmetric (deviations occur only due to pixellation), it does not matter where on the edge the center of the obscuration is located. Therefore, an arbitrary location can be chosen without loss of generality. My choice has been to place the obscuration center in the same column as the aperture center and r_P pixels away from (x_P, y_P) in the negative y direction. Mathematically, $(x_O, y_O) = (x_P, y_P - r_P)$. Beware: as r_P does not have to be an integer, the obscuration center might not coincide with a pixel. The obscuration radius is denoted by r_O and can have any arbitrary nonnegative value.

The mathematical prescription for A'_P is thus

$$r(x, y) = \sqrt{(x - x_O)^2 + (y - y_O)^2} \tag{3.3a}$$

$$A'_P(x, y) = \begin{cases} 0 & \text{if } r(x, y) < r_O \\ A_P(x, y) & \text{if } r(x, y) \geqslant r_O \end{cases} \tag{3.3b}$$

Relative aperture size and zero padding

With an aperture and a possible obscuration in place, we have constructed a pupil plane amplitude map. We could still wonder though what the effect would be of increasing the size of the aperture while fixing the map dimensions. Additionally, we could ask ourselves whether

[5] To make use of the convenient `numpy.fft.ifftshift` routine, the pixel of choice should be $(x_C + \frac{1}{2}, y_C + \frac{1}{2})$.

[6] For any sensible aperture radius, Equation 3.2 dictates that (x_P, y_P) is part of the aperture. Also, when $(x_P + a, y_P)$ is close enough to the aperture center to be part of the aperture, so will $(x_P - a, y_P)$ (along with $(x_P, y_P + a)$ and $(x_P, y_P - a)$ for that matter).

increasing the map dimensions whilst keeping the aperture unchanged would bring us any merits.

By increasing the aperture size only, the PSF generated using this PPAM will decrease in spatial extent. The effect of diffraction becomes less dominant, and the wave nature of light is gradually concealed. Geometrical optics becomes increasingly adequate in describing the PSF.[7] Although in the idealized world of mathematics the new point spread function PSF$'$ would still contain the same information as the old one (PSF$'(x,y)$ = PSF$(\xi x, \xi y)$ where $\xi > 1$), this is not the case in simulations. As the intensity profile must be stored using a fewer number of pixels, the sampling of the PSF decreases, and information on high spatial frequency intensity variations is lost. On the upside, increasing the pupil size improves the circularity of the aperture as the stains of pixellation diminish.

Increasing the map dimensions while keeping the aperture fixed brings in a lot of zeroes in the space around the aperture, and is therefore also called *zero padding*. It has the effect of increasing the sampling of the PSF, as if it divides spatial unit cells (pixels) into smaller units of space. This is understandable: in a Fourier transformed map with M rows, the probed spatial frequencies are given by $0, \frac{1}{M}, \frac{2}{M}, ..., \frac{M-1}{M}$. If the map had its dimensions doubled, the spatial frequencies would become $0, \frac{1}{2M}, \frac{1}{M}, \frac{3}{2M}, \frac{2}{M}, ..., \frac{M-1}{M}, \frac{2M-1}{2M}$. In order words, doubling the map dimensions also doubles the amount of detectable spatial frequencies, giving rise to a more refined image.

3.1.2 Creating the pupil plane phase map

dOTF WFS is a technique that enables one to reconstruct the pupil plane phase map $\phi_P(x,y)$. There are two main applications for the technique, and for each I implemented suitable phase patterns.

1. *Finding aberrations $\phi'_P(x,y)$ in optical instruments.* The dOTF WFS should be able to measure tip-tilt and defocus. A tip-tilt aberration amounts to a flat wavefront whose wave vector $\vec{k}$ makes a non-zero angle with the Poynting vector $\vec{S}$. In terms of the PPPM, tip-tilt translates to a gradient. The tip-tilt in the simulations is quantified with a gradient vector $\vec{\nabla}\phi'_P$. It points in the direction of strongest increase in phase and its length $||\vec{\nabla}\phi'_P||$ expresses the steepness of the slope. The tip-tilt aberration is given by

$$\phi'_P(x,y) = \vec{\nabla}\phi'_P \cdot \vec{r} = (\vec{\nabla}\phi'_P)_x x + (\vec{\nabla}\phi'_P)_y y \tag{3.4}$$

   The defocus aberration is implemented as a paraboloid having the aperture center as the position of its extremum.[8] It is given by

$$\phi'_P(x,y) = \xi((x-x_P)^2 + (y-y_P)^2) \tag{3.5}$$

   where ξ is a measure of the strength of curvature of the paraboloid.

2. *Measuring atmospheric turbulence.* In adaptive optics systems, a dOTF wavefront sensor will measure the wavefront of light that has passed through the turbulent atmosphere. For

[7] Consider for instance the Airy pattern, the intensity profile that results from light of a fixed wavelength falling through a circular aperture having a planar wavefront oriented perpendicular to the pupil plane. Increasing r_P squeezes the Airy pattern into a smaller region of space. For the untrained eye, eventually it will seem as if all flux goes through a single point in the focal plane (the *focal point*), as geometrical optics predicts for light rays.

[8] Although the aberration was implemented in this way, there is no reason to restrict the position of the defocus paraboloid center to the aperture center.

this reason, I also enabled the possibility to generate PSFs using atmospheric PPPMs. For this, I used a Kolmogorov phase map implementation from Emiel Por, BSc.[9] The main parameter for the phase map is the Fried parameter r_0, which can be specified in my simulations in terms of $\frac{D}{r_0}$ (where, just like in the theory Chapter, $D \equiv 2r_P$). By increasing the Fried parameter, the resulting phase map corresponds to a less turbulent atmosphere.

3.1.3 Creating the point spread function

Armed with a PPAM and a PPPM, the PSF is readily found. The maps are combined to form a complex amplitude map, which is fast Fourier transformed. The squared modulus of the resulting map gives us the PSF.

PSF normalization

Now, proper normalization needs to be done.[10] The mathematical, continuous PSF described in the theory Chapter, can be regarded as a probability density function. The PSF in our simulations is discretized due to pixellation of otherwise real space. Therefore, the simulated PSF can be normalized to represent a probability mass function (PMF):

$$\mathrm{PSF}_{\mathrm{PMF}}(x,y) = \frac{1}{\sum_{i=0}^{M-1}\sum_{j=0}^{N-1}\mathrm{PSF}_{ij}}\mathrm{PSF}(x,y) \tag{3.6}$$

This PMF can be regarded as a statistical distribution. We could envisage this as if every photon that arrives at the detector chip decides to end its journey at a random pixel, where the probability to end at some pixel (x,y) is given by $\mathrm{PSF}_{PMF}(x,y)$. Next, there are two convenient ways to continue:

- One could define the camera's integration time and the mean number of photons that reach the detector per unit of time. These numbers could then be multiplied to form the expected number of photons that reach the detector during this integration time, which we can denote with E_γ.[11] The expected number of photons per pixel is given by

$$\mathrm{PSF}_{\gamma}(x,y) = E_\gamma \mathrm{PSF}_{\mathrm{PMF}}(x,y) \tag{3.8}$$

- One could normalize the PSF in such a way that the expected number of photons at the PMF maximum equals some value $\mathrm{PSF}_\gamma(x_{\max}, y_{\max})$. Under this normalization, the expected number of photons per pixel is given by

$$\mathrm{PSF}_{\gamma}(x,y) = \frac{\mathrm{PSF}_\gamma(x_{\max},y_{\max})}{\mathrm{PSF}_{\mathrm{PMF}}(x_{\max},y_{\max})}\mathrm{PSF}_{\mathrm{PMF}}(x,y) \tag{3.9}$$

[9] Por implemented three different algorithms to generate Kolmogorov phase maps: one by Yao, one by Glindemann and Lane, and a fractal-based approach. In this research, the fractal algorithm was used to generate the PPPMs. For more information, contact Por via `por@strw.leidenuniv.nl`.

[10] In reality, the PSF is 'normalized' by adjusting the *initial* light intensity, which would be equivalent to adjusting the PPAM in the simulations. As Fourier transformation is a linear operation in the sense that $\mathscr{F}(af(\xi)+bg(\xi)) = a\mathscr{F}(f(\xi)) + b\mathscr{F}(g(\xi))$, and the PSF is retrieved by taking the squared modulus of a Fourier transformed function, using a normalization factor a for the PPAM would amount to using a normalization factor $|a|^2$ for the PSF. So although it might seem unnatural, scaling the PSF is just another way of scaling the PPAM.

[11] It can be shown easily that E_γ indeed is the expectation value of the total number of photons arriving at the detector per exposure when used as in Equation 3.8:

$$\mathbb{E}\Big(\sum_{y=0}^{M-1}\sum_{x=0}^{N-1}\mathrm{PSF}_\gamma(x,y)\Big) = \sum_{y=0}^{M-1}\sum_{x=0}^{N-1}\mathbb{E}(\mathrm{PSF}_\gamma(x,y)) = E_\gamma\sum_{y=0}^{M-1}\sum_{x=0}^{N-1}\mathrm{PSF}_{\mathrm{PMF}}(x,y) = E_\gamma \tag{3.7}$$

Both normalization methods were implemented. The simulation results presented in this thesis all use the former method.

PSF' normalization

For dOTF wavefront sensing simulations, two images are necessary. The PSFs will be different, as one is some mathematical combination of A_P and ϕ_P, while the other is made by applying the same operations on A'_P and ϕ_P. Only the pupil *transmittance* should differ - the intensity of the incident light waves should be constant. Therefore, if the normalization constant that scales the raw PSF to PSF_γ is determined for the image taken using the regular aperture, the same normalization constant must be applied in scaling PSF' to PSF'_γ.

3.2 Simulating an electron map

3.2.1 From PSF to realization

Photon shot noise

The normalized PSF is the blueprint for simulating digital images. But due to photon shot noise, not every image that is based on a given pair of PPAM and PPPM will be the same. As electromagnetic energy does not reach the detector in a continuous way, but in discrete packages, no light source can have a power output that *really* stays constant in time. As a Gedanken experiment, we could focus our attention on the photon emission of some light source and descend to lower and lower time scales until we can discern time intervals in which either one or no photon was emitted. Considering the time interval between emission of two photons cannot be perfectly constant for any real physical light source, the origin of photon shot noise is understood.

Creating the photon map

Whenever we image a light source that is said to have a constant flux, we mean that the *expectation value* of the number of photons reaching the telescope per unit time is time-independent. The actual photon numbers that hit each detector pixel are always realizations of a Poisson distribution with mean $\mathrm{PSF}_\gamma(x, y)$.

We thus create a new map N_γ, that contains realizations of Poisson distributions whose means are given by PSF_γ. In concreto,

$$\mathbb{P}(N_\gamma(x, y) = k) = \frac{1}{e^\lambda} \frac{\lambda^k}{k!} \text{ where } \lambda \equiv \mathrm{PSF}_\gamma(x, y) \tag{3.10}$$

Note that while N_γ only contains integers, $\mathbb{E}(N_\gamma(x, y)) \equiv \mathrm{PSF}_\gamma(x, y)$ is generally a float.

From photons to electrons

Every photon that hits a pixel of a CCD chip excites one electron in the detector material. A known fraction of these electrons is subsequently pulled into electric field traps that are set up at every pixel before they have the chance to recombine with an ionized atom.[12] Charges

[12] This fraction stays approximately constant in time as it is the result of the CCD design, depending on the geometry and materials. It can be determined in the lab using a light source of a known strength.

accumulate here until the CCD is read-out. Under the assumption of an ideal detector design in which all photons that hit the CCD will cause a trapped electron, the basic electron map given some photon map is obtained very easily: $N_e = N_\gamma$.

3.2.2 Modelling thermal excitations

Unfortunately, every CCD image will suffer from thermal excitations in the crystal lattice that give rise to ionized atoms and free electrons in the same fashion as incoming photons do. This phenomenon will result in the unfortunate situation that a part of the electrons stored in the electric field trap of a pixel will not be astronomical signal but rather noise. These thermal excitations are modelled in the simulations by adding to each pixel of the electron map $N_e(x, y)$ a realization of a Poisson distribution with some collective expectation value E_{TE}.

3.3 Simulating a digital image

3.3.1 From chip to circuit

After the exposure time is over, the chip is read out. In a frame-transfer CCD design, the charges leave the chip in two steps: first, the charges in the image array are quickly transferred to a neighboring storage array. Then, while the pixels in the image array can go back to integration mode, the electrons in the storage array leave the sensor area on a per-pixel basis towards the electronic circuit of the camera. Charges are shifted from pixel to pixel by means of changing the locations of the electric field traps.

3.3.2 Bias

Each pixel value is represented in the electronics as a voltage signal. Alongside the variable current this will produce, the electronic components on the camera's circuit board also require a steady bias current to work properly. In my simulations I assume that the bias can be translated back as a constant number of electrons per pixel, so that the values in $N_e(x, y)$ can be increased uniformly. In reality the bias is of course not a real constant, but a random variable. I account for this in the implementation of read-out noise. Also, oftentimes the mean bias is slightly pixel-dependent. I have ignored this fact in the simulations.

3.3.3 Thermodynamic motion

Whenever the electrons representing a pixel signal flow alongside the bias electrons through the electronic circuit of the CCD towards the analog-to-digital converter (ADC), they undergo thermal motion alongside their intended directional motion. This random motion can cause some of them to momentarily move astray from the direction they should be going. As there are so many electrons by virtue of the bias, the current will continue to flow in the intended direction. It is not hard to imagine that this thermodynamic motion causes the pixels's electrons, which should ideally travel in tight batches, to spread out spatially.

3.3.4 Amplification

As an ADC cannot accurately measure tiny currents, each pixel's signal is amplified by a certain factor. This factor is a parameter of the simulations. The amplification is not a perfectly accurate process though and brings noise into the final image.

3.3.5 Read-out noise

Hitherto, several forms of noise have been described that were not yet accounted for in the simulations:

- Noise occurring from shifting charges from the image array to the storage array and from the storage array towards the camera's circuit board
- Bias variations
- Electron diffusion within the electronic circuit
- Noise caused by imperfect signal amplification

Together, these forms of noise are called *read-out noise*. Rather than considering their effects independently, I have chosen to model them collectively. For each pixel, a draw from a Gaussian distribution with mean 0 and standard deviation σ_{RN} is added to the electron map. Although a normal distributed random variable produces non-integer realizations, we are still talking about electron numbers, and therefore every Gaussian draw was rounded off to the nearest integer value.

3.3.6 Digitization

The final steps to form a digital image $N_D(x, y)$ from the map $N_e(x, y)$ happen within a patch of circuitry that applies the effect of the chosen gain setting g (in electrons per ADU) and - finally - the ADC. The ADC converts every signal it receives into a string of ones and zeroes. The length of the string determines the number of illumination levels that the camera can discern, and is called the *ADC resolution*, *color depth* or *bit depth* (bpp). The number of discernible illumination levels is 2^{bpp}. The highest illumination level corresponds to an electron number of $(2^{\mathrm{bpp}} - 1)$ ADU g. If the number of electrons per signal exceed this limit, the returned illumination level will remain $2^{\mathrm{bpp}} - 1$. Therefore, if one wants an unsaturated image, it is required that $(2^{\mathrm{bpp}} - 1)$ ADU $g > N_{e,\max}$.

The bit depth dictates the number of discernible signal levels and the gain the spacing between the levels. As long as the gain does not equal 1 electron per ADU, most of the pixels's signals will not neatly correspond to any of the electron numbers n ADU g where $n \in [0, 2^{\mathrm{bpp}}\rangle$. For such signals, the ADC can only output a binary string that is only an approximate description of the number of electrons that were in the signal. As multiple electron numbers will result in the same binary string, information about the precise electron numbers is lost in the conversion from $N_e(x, y)$ to $N_D(x, y)$. This effect is called *quantization error*. The final image map $N_D(x, y)$ is given by

$$N_{D,\mathrm{unbounded}}(x, y) = \mathrm{round}(\frac{N_e(x, y)}{g \text{ ADU}}) \text{ ADU} \tag{3.11a}$$

$$N_D(x, y) = \begin{cases} 0 \text{ ADU} & \text{if } N_{D,\mathrm{unbounded}}(x, y) \leqslant 0 \text{ ADU} \\ 2^{\mathrm{bbp}} - 1 \text{ ADU} & \text{if } N_{D,\mathrm{unbounded}}(x, y) \geqslant 2^{\mathrm{bpp}} - 1 \text{ ADU} \\ N_{D,\mathrm{unbounded}}(x, y) & \text{otherwise} \end{cases} \tag{3.11b}$$

3.4 dOTF pupil plane phase map recovery

Digital image generation is a prerequisite to simulating PPPM reconstructions using the dOTF technique, to which we will proceed now.

3.4.1 Retrieving a raw dOTF PPPM

Suppose we have made two images $N_D(x, y)$ and $N'_D(x, y)$, using a regular and obscured aperture respectively. Again, the incoming wavefront and light intensity are identical. We follow the steps as outlined in Section 2.7:

$$\text{OTF} = \mathscr{F} N_D \tag{3.12a}$$

$$\text{OTF}' = \mathscr{F} N'_D \tag{3.12b}$$

$$\text{dOTF} = \text{OTF} - \text{OTF}' \tag{3.12c}$$

$$\phi_{\text{dOTF,raw}} = \text{Arg dOTF} \tag{3.12d}$$

The phase map obtained in this way is not a map we can directly compare with the input phase map ϕ_P. While ϕ_P might represent a wavefront that extends far and wide, only the part of the wavefront that passes through the transparent region of the pupil plane - the aperture disk - can possibly be reconstructed. It is therefore not surprising that the only reliable information in $\phi_{\text{dOTF,raw}}$ resides in a set of two disks containing the aperture phase values. Apart from the data in the pair of partially overlapping disks, the map is worthless. The disks contain the same information, and for this reason we can just select one of them without throwing away anything we know about our reconstruction of ϕ_P.

3.4.2 Selecting a disk

The centers of the disks $(x_D, y_{D\pm})$ in $\phi_{\text{dOTF,raw}}$ are given by

$$x_D = x_P \tag{3.13a}$$

$$y_{D\pm} = y_P \pm (r_P - \frac{1}{2} r_O) \tag{3.13b}$$

The disks have the same shape as the regular aperture, and therefore have a radius r_P. From the equation above it is clear that for any obscuration radius $r_O > 0$, there is an overlap region in the map $\phi_{\text{dOTF,raw}}$. Let Δy be the distance between the two centers of the disks. Then $\Delta y \equiv y_{D+} - y_{D-} = y_P + (r_P - \frac{1}{2} r_O) - (y_P - (r_P - \frac{1}{2} r_O)) = 2r_P - r_O < 2r_P$. In general, this overlap region does not contain reliable information about ϕ_P, and to be safe it should be removed from what we pretend is a trustworthy reconstruction of the PPPM.
Although both disks contain the same information, the simplest way to obtain a map ϕ_{dOTF} that can be directly compared to ϕ_P, is to rotate $\phi_{\text{dOTF,raw}}$ by 180°, select the upper disk and mask the overlap region.

ϕ_{dOTF} is an approximation of the part of ϕ_P that coincides with the aperture area, save the obscuration-determined overlap region.

3.4.3 Aligning the maps

After we have made our reconstruction, $\phi_P(x, y)$ and $\phi_{\text{dOTF}}(x, y)$ must be well-aligned.
The center of the part of $\phi_P(x, y)$ of which the wavefront sensor can know of, is given by the center of the aperture map: (x_P, y_P). We call the corresponding point in $\phi_{\text{dOTF}}(x, y)$ $(x_{P,\text{dOTF}}, y_{P,\text{dOTF}})$, which is given by $((N-1) - x_P, (M-1) - y_{D-}) = (N - 1 - x_P, M - 1 - y_P + r_P - \frac{1}{2} r_O)$. By using the definitions given, this boils down to

$$(x_{P,\text{dOTF}}, y_{P,\text{dOTF}}) = \begin{cases} (x_P - 1, y_P - 1 + r_P - \frac{1}{2} r_O) & \text{for even M and N} \\ (x_P, y_P + r_P - \frac{1}{2} r_O) & \text{for odd M and N} \end{cases} \tag{3.14}$$

To align the maps on top of each other, I have arbitrarily chosen to shift the actual PPPM until it is aligned well unto the dOTF PPPM.[13] The shifts necessary are now simply

$$(\Delta x, \Delta y) = \begin{cases} (-1, -1 + r_P - \frac{1}{2} r_O) & \text{for even M and N} \\ (0, r_P - \frac{1}{2} r_O) & \text{for odd M and N} \end{cases} \tag{3.15}$$

Although integer shifts are readily carried out using e.g. the `numpy.roll` routine, sub-pixel shifts require another solution. I used the Fourier shift property, which is for two dimensions given by

$$\mathscr{F}(f(x + \Delta x, y + \Delta y)) = \mathscr{F}(f(x, y)) e^{2\pi i (u\Delta x + v\Delta y)} \equiv F(u, v) e^{2\pi i (u\Delta x + v\Delta y)} \tag{3.16}$$

Equation 3.15 indicates that sub-pixel shifts are only possibly required in the row direction, due to the choice of the obscuration position. For our purposes, the functional form of the Fourier shift property thus is

$$\mathscr{F}(f(x, y + \Delta y)) = \mathscr{F}(f(x, y)) e^{2\pi i v \Delta y} \tag{3.17}$$

Here, v is one of the Fourier transform coordinates, taking on the values $0, \frac{1}{M}, \frac{2}{M}, ..., \frac{M-1}{M}$.
As we're interested in finding the shifted function $f(x, y + \Delta y)$, we need to do an inverse Fourier transform as well:

$$f(x, y + \Delta y) = \mathscr{F}^{-1}(\mathscr{F}(f(x, y + \Delta y))) = \mathscr{F}^{-1}(\mathscr{F}(f(x, y)) e^{2\pi i v \Delta y}) \tag{3.18}$$

Using the equation above, $\phi_P(x, y)$ was aligned on top of $\phi_{\mathrm{dOTF}}(x, y)$.

3.5 dOTF pupil plane phase map quality

3.5.1 The difference map

The reason for aligning the maps, is that the difference between the two can be used to quantitatively express the extent to which the dOTF PPPM approximates the actual PPPM.

Definition

The difference map is defined by

$$\phi_\Delta(x, y) \equiv \phi_P(x, y) - \phi_{\mathrm{dOTF}}(x, y) \tag{3.19}$$

As a phase difference of ϕ_Δ is equivalent to a phase difference of $\phi_\Delta + 2\pi$ rad, we perform the modulo operation on $\phi_\Delta(x, y)$ so that all its values lie in the range $[0, 2\pi\rangle$.

Interpretation

The difference map has an elegant interpretation. Although ϕ_P might represent the real wavefront incident to some telescope, the dOTF wavefront sensor nearby thinks the wavefront is represented by ϕ_{dOTF}. It sends its measurement to the AO system in the telescope, that adapts its deformable mirrors (DMs) to compensate for the suspected wavefront aberrations. If the DM system would be perfect, it could completely flatten the incoming wavefront *if it were true that* $\phi_P = \phi_{\mathrm{dOTF}}$. As the dOTF PPPM is an imperfect reconstruction of the actual PPPM, even a perfect DM system would not get rid of all wavefront aberrations. Thus ϕ_Δ represents the remaining wavefront aberrations when an ideal deformable mirror system would be deployed to flatten ϕ_P using the wavefront sensor data ϕ_{dOTF}.
In other words, ϕ_Δ expresses the extent of which dOTF wavefront sensing is the limiting factor in a wavefront flattening AO system.

[13] Of course, it would also be possible to move the dOTF PPPM until it matches the actual PPPM.

3.5.2 Root mean square

A perfect reconstruction would give rise to a flat difference map: $\phi_\Delta(x, y) = \mathscr{C}\ \forall(x, y)$. $\mathscr{C}$ might not necessarily be 0, as the actual and dOTF PPPMs might still differ a trivial constant from each other. Clearly, the degree in which $\phi_\Delta(x, y)$ deviates from being flat is an indication of the quality of the dOTF reconstructed PPPM. Fluctuations relative to some mean level can be quantified in terms of the variance. The slightly biased plug-in estimator and maximum likelihood estimator (MLE) of the variance is given by

$$\hat{\sigma}^2 = \frac{1}{MN} \sum_{i=1}^{M} \sum_{j=1}^{N} (\phi_{\Delta,ij} - \langle \phi_\Delta \rangle)^2 \tag{3.20}$$

where $\langle \phi_\Delta \rangle$ is the mean value of the difference map.
The reconstruction quality of a dOTF PPPM is measured in this research using a quantity that has radians as units, given by

$$\text{RMS} \equiv \sqrt{\hat{\sigma}^2} = \sqrt{\frac{1}{MN} \sum_{i=1}^{M} \sum_{j=1}^{N} (\phi_{\Delta,ij} - \langle \phi_\Delta \rangle)^2} \tag{3.21}$$

The lower the RMS, the better the reconstruction.

3.5.3 Phase wrapping

Description

In many cases, bluntly computing the RMS according to Equation 3.21 will overestimate the actual deviation of the map's values from the mean. This is due to *phase wrapping* - the already mentioned fact that to a wave of phase ϕ_Δ we could physically equally well allot a phase of $\phi_\Delta + 2\pi$ rad. Therefore, although a phase value of $2\pi - \delta$ rad for some $0 < \delta << 1$ might seem to lay far away from a phase of 0, the effective phase difference is just δ rad.

Example

Suppose for instance that ϕ_{dOTF} is a good reconstruction of ϕ_P, so that the values in ϕ_Δ lie closely packed together. Every now and then, the bulk location might happen to lie on the phase wrapping border, so that ϕ_Δ contains many values just below 2π rad and just above 0. One could imagine that computing $\langle \phi_\Delta \rangle$ in this case will result in a value that lies close to π rad. As all phase values lie either around 0 or 2π, the deviations from the mean will be roughly π rad for every pixel, so that we eventually obtain RMS $\approx \pi$ rad. This is clearly an unacceptable result, as all phase values physically lie very close together.
The problem here is of course that we attribute hugely different numerical values to quantify oscillation states that are almost the same.
A graphical overview that illustrates the phenomenon is shown in Figure 3.1.

Solution

As a solution to find a better RMS for some map ϕ_Δ, I use the following simple algorithm:

1. Make a histogram of all values in ϕ_Δ using n equally spaced bins that cover the complete phase range $[0, 2\pi \text{ rad}\rangle$.

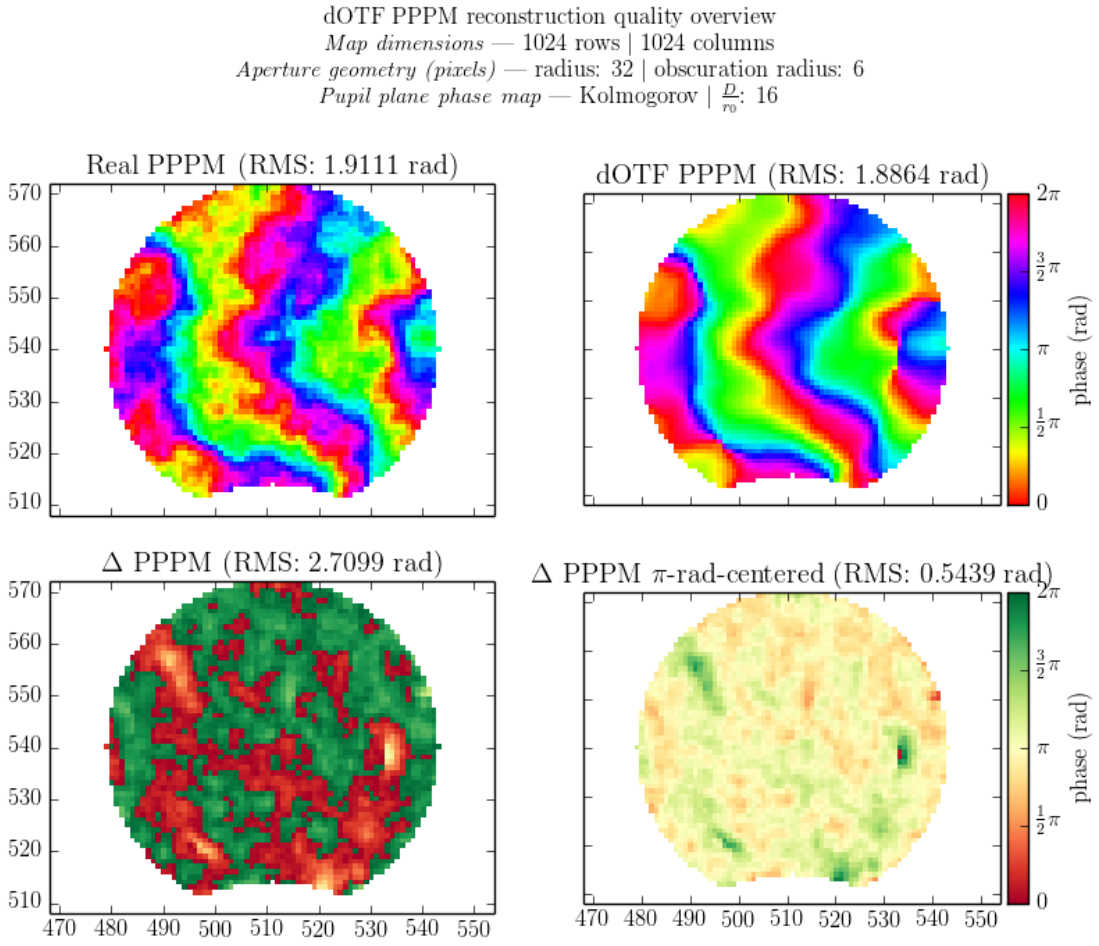

Figure 3.1: Overview of a dOTF pupil plane phase map reconstruction that outlines the problem of phase wrapping. Top left: ϕ_P. Top right: ϕ_{dOTF}. Bottom left: ϕ_Δ. Many of its phase values lie close to the borders of the phase range, so that the RMS is high. Bottom right: ϕ_Δ as well - but now piston-shifted so that the RMS is minimized. In this example, dOTF WFS with perfect DMs allows for a 72% RMS reduction relative to the same scenario without AO.

2. Identify the bin containing the most phase values, and find the central phase value ϕ_{most} of this bin.
3. Shift all phase values in the map with π rad $- \phi_{\text{most}}$, so that the most populated bin now resides at π rad, the center of the phase range.
4. Compute the RMS using this adjusted map.

3.6 Finding the best fixed obscuration radius

The obscuration is the defining feature of a dOTF wavefront sensor. In this section, we inquire how large it should be to optimize the performance of the device.

3.6.1 General considerations

Definition of the best obscuration

The best performing fixed obscuration is understood as the obscuration that minimizes the cumulative RMS of a large set of PPPM reconstructions. A small obscuration radius allows for greater detail in the dOTF PPPM than a big obscuration, but is more susceptible to noise at the same time. Somewhere in the trade-off between small-scale structure mapping and noise reduction, a 'sweet spot' obscuration radius can be discerned.

Fixed versus variable obscuration

The polarizing beamsplitter dOTF WFS design analyzed in this research uses a disk-shaped piece of polarizing material to effectuate an immobile obscuration of fixed size. The instrument consequently has no moving parts, making it resistent to the elements and free of internal technical maintenance. This section discusses the best obscuration sizes for various levels of atmospheric turbulence.
A more advanced implementation of the polarizing beamsplitter dOTF WFS design includes a liquid crystal. The crystal functions as an obscuration that continuously changes its size during observations in order to optimize performance based on the brightness of the sensor's target star and the current level of atmospheric turbulence. The feasibility and merits of using a variable obscuration size are discussed in Section 3.7.

Algorithm outline

The algorithms used to find the best fixed obscuration radius for a given light source and $\phi_P(x, y)$ are variations on the following idea:

1. Define a range of obscuration radii that need to be tested on their ability to maximize the wavefront reconstruction quality.
2. For each obscuration radius:
   (a) Generate a realization of an image using a regular aperture.
   (b) Generate a realization of an image using an obscured aperture.
   (c) Find the dOTF PPPM using these images and compute its reconstructive quality. A RMS value is obtained in this way.
3. After all obscuration radii in the predefined range have been tested, the best fixed obscuration radius is picked as the one minimizing its RMS.

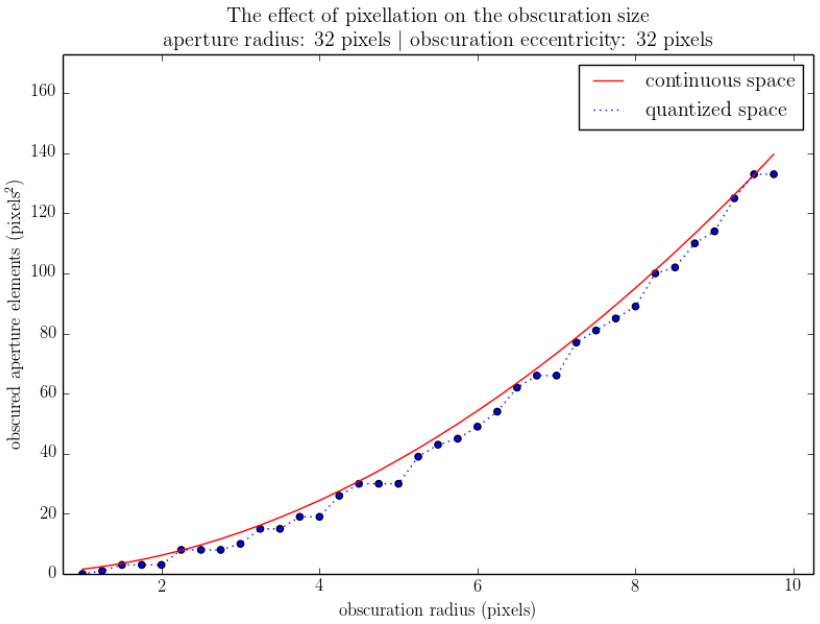

Figure 3.2: Comparison of the number of pixels in the obscured region of the aperture as a function of obscuration radius for continuous space (red) and quantized space (blue). Note that due to the choice to exclude pixels from the obscuration that lie exactly on its edge, we systematically use a smaller obscured area in the simulations than would be produced by the same obscuration radius in real space.

Pixellation

Due to the definition of the aperture, the chosen position of the obscuration and the phenomenon of pixellation, any obscuration radius $\leqslant 1$ pixel will not obscure the aperture. A small spacing between obscuration radii is desirable, although for small spacings the obscuration sometimes does not increase in size due to pixellation. In general, it is good to note that the number of pixels contained in the obscuration does not increase in a smooth quadratic fashion as one expects in continuous space. This is demonstrated in Figure 3.2.
It is important to mention this effect as it embodies a systematic error in the best obscuration radius determination.

Best obscuration: dependence on ϕ_P

An important observation to make is that the best fixed obscuration radius depends on the input PPPM ϕ_P that the dOTF WFS should measure. This is problematic: the aim of the wavefront sensor is to measure an unknown ϕ_P, but doing this in an optimized way would require knowledge of ϕ_P.
The best approach therefore is to distinguish between several input pupil plane phase patterns, and compute the best obscuration sizes for each of these individually. Atmospheric phase patterns are discussed in this section. Instrumental phase patterns are discussed in Appendix A.

Best obscuration: dependence on noise

Many of the noise sources and digitization settings that can be set in the simulations, vary from device to device. Although these simulations can be very handy to optimize the performance of a specific dOTF wavefront sensor, for this thesis general results that inquire the highest attainable quality of polarizing beamsplitter dOTF wavefront sensing are of greater interest. Therefore, in the coming sections, I will assume an ideal instrument, in the sense that its only noise source is photon shot noise. Would other noise sources be included, then mainly the reconstructions using small obscuration radii would deteriorate.

Best obscuration: dependence on light intensity

As photon shot noise is Poisson distributed, it is easy to see that the adverse effect of photon shot noise diminishes with increasing illumination. If the expectation value for the number of photons incident on some pixel during an integration equals $\mathbb{E}(N_\gamma(x,y))$, the Poisson distribution as given by Equation 3.10 and the definition of the variance yield $\mathbb{V}(N_\gamma(x,y)) = \mathbb{E}(N_\gamma(x,y))$. The signal-to-noise ratio for this pixel is then equal to

$$\frac{S}{N}(x,y) \equiv \frac{\mathbb{E}(N_\gamma(x,y))}{\sqrt{\mathbb{V}(N_\gamma(x,y))}} = \sqrt{\mathbb{E}(N_\gamma(x,y))} \tag{3.22}$$

It is thus apparent that higher illumination levels increase the signal-to-noise ratio of images. Small obscuration radii enable the identification of more details in the reconstruction of the pupil plane wavefront, but can become useless due to noise effects. For this reason, we expect that for higher illumination levels and thus an enhanced signal-to-noise ratio, the best fixed obscuration radius shifts downwards.

Further outline of this section

We conclude that without further specification, the question *'What is the best obscuration radius for a polarizing beamsplitter dOTF WFS?'* is ill-defined. To provide an unambiguous answer, we should at least specify the wavefronts we would like to measure and the illumination conditions under which we do this.
Let's recall that the main application for the polarizing beamsplitter dOTF WFS will be probing atmospheric turbulence as part of an AO system. For this reason, the wavefronts under consideration are Kolmogorov phase maps, which are discussed in Section 3.6.2, and the illumination conditions are set by stars. The case of bright star observation is explored in Section 3.6.3, for which the best obscuration radii are found. Finally, in Section 3.6.4 it is inquired how these obscurations hold up when dimmer stars are used for dOTF WFS.

3.6.2 Atmospheric wavefronts

The Fried parameter

The aberrations induced in ϕ_P by atmospheric turbulence vary from moment to moment, even for fixed values of the parameter that describe the turbulence statistically. This is due to the fact that the atmosphere is in constant motion from one state into another. The amount of turbulence in the atmosphere for a given wavelength is described by the *Fried parameter* or *Fried's coherence length* r_0, as quickly mentioned earlier. [2] A common definition of the Fried parameter states that r_0 is the diameter of a circular aperture that covers an area over which

the mean phase RMS is 1 rad. Quantitatively, the Fried parameter is often defined as

$$r_0(\lambda) \equiv 0.185\ \lambda^{\frac{6}{5}} \left(\int_0^\infty C_n^2(z) dz \right)^{-\frac{3}{5}} \tag{3.23}$$

where we can see that the wavelength dependence of the Fried parameter is $r_0 \propto \lambda^{\frac{6}{5}}$. In other words, the same amount of atmospheric refractivity inhomogeneities, expressed by the integral over the *refractive index structure constant* $C_n^2(z)$, gives rise to different seeing effects for different wavelengths. Larger wavelengths increase the Fried parameter, and imply observations less troubled by the dynamics of the atmosphere.

Order of magnitude of $\frac{D}{r_0}$ for optical wavelengths

For a given wavelength at a fixed observatory location, the variability of the Fried parameter is often limited. Exemplum gratia, at the William Herschel Telescope (WHT) on La Palma, the Fried parameter at a wavelength of 500 nm was found to lie between 6 and 28 cm for 90% of the time. The median value was 15 cm. [9][10] For a telescope diameter of 30 cm, $\frac{D}{r_0}$ would thus vary roughly between 1.1 and 5.0. To keep the scope of the simulations broad enough to apply to

- dOTF wavefront sensors with larger apertures than $D = 30$ cm
- Skies more turbulent than above Roque de los Muchachos, La Palma, one of the best observing sites of the world
- Shorter wavelengths than 500 nm

it makes sense to also inquire the best dOTF WFS design for higher values of $\frac{D}{r_0}$. Therefore, the forthcoming results show a variation in $\frac{D}{r_0}$ from 0.5 to 13.

Kolmogorov phase maps

The Kolmogorov turbulence model is a mathematical description of the turbulent flows conceived by Soviet mathematician Andrey Kolmogorov in 1941. [1] The theory can be used to predict the effects of turbulence on the light that arrives at ground-based telescopes. It asserts that energy is added to the fluidum of interest as large-scale disturbances, that continually break down in smaller structures. [6] In this research, based on the work of Emiel Por BSc, the Kolmogorov turbulence model has been used to construct phase maps for light waves traveling from space through the turbulent atmosphere towards detectors on ground.
For $\frac{D}{r_0} = 10$, an example atmospheric wavefront is shown in Figure 3.3.

Best fixed obscuration determination algorithm: the atmosphere

In contrast to instrumental aberrations, where $\phi_P(x, y)$ is a fixed pattern, realizations of the Kolmogorov atmosphere for a given value of parameter $\frac{D}{r_0}$ are subject to the whims of probability. By chance, some realizations locally exhibit flat wavefronts at the dOTF WFS aperture, while other realizations might be very turbulent at this area of the map.[14] This can be seen in Figure 3.3

[14]The concept of lucky imaging is based on the principle that for a given atmosphere, every now and then the seeing happens to be excellent. By only selecting the highest quality images produced by a high-speed camera and using digital processing to obtain a final image, the diffraction limit of a telescope can be reached without the aid of adaptive optics systems.

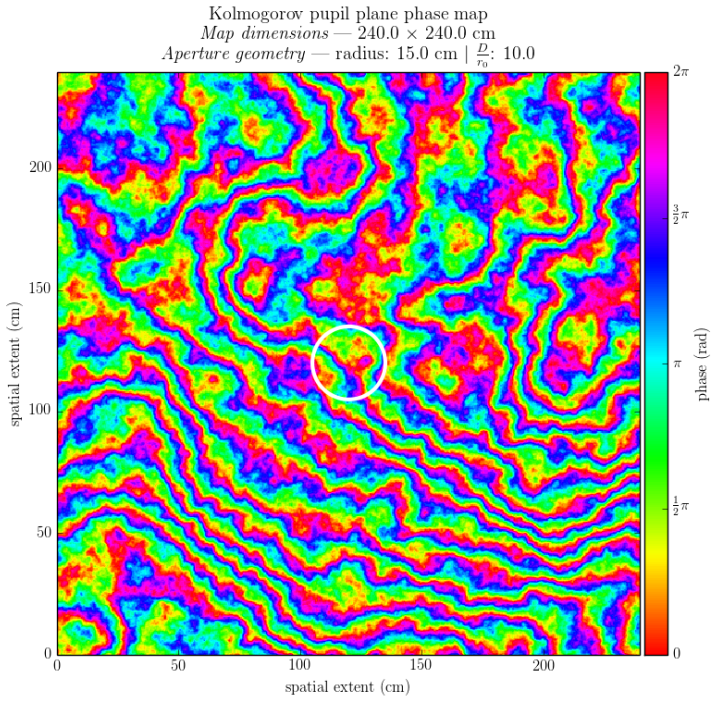

(a) Pupil plane phase map. The part that the dOTF WFS actually sees is surrounded by a white circle.

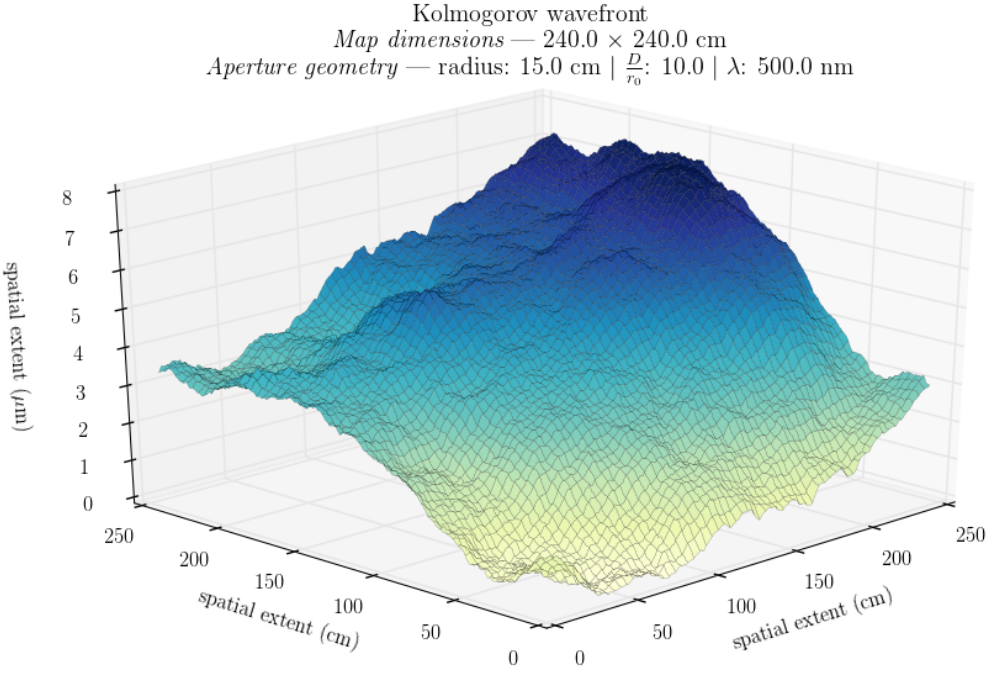

(b) Corresponding wavefront.

Figure 3.3: Realization of the Kolmogorov atmosphere for $\frac{D}{r_0} = 10$.

as well: we can easily find both quiet and very turbulent patches of the atmosphere by moving the white ring around.
For this reason, to find the best fixed obscuration radius for an atmosphere characterized by some value of $\frac{D}{r_0}$, many realizations of Kolmogorov turbulence have to be used. The following algorithm was used:

1. Define a set of n_O different obscuration radii to test. Note that every obscuration radius can be thought to correspond to a specific dOTF wavefront sensor design. Thus imagine the installment of n_O dOTF WFS prototypes at some astronomical observing site, where each prototype has a distinct obscuration. The wavefront sensors all look towards the same star and are confronted with the same incoming wavefront.[15]

2. We perform wavefront reconstruction with all wavefront sensors simultaneously on n_W uncorrelated realizations of the Kolmogorov atmosphere. In our Gedanken experiment, this would mean that the waiting time between two reconstruction commands is made long enough to completely lose the correlation of one Kolmogorov PPPM with the previous realization. Thus we obtain $n_O \times n_W$ wavefront reconstructions in total.

3. Each of the wavefront sensors has done n_W wavefront measurements. The quality of each of these measurements is computed. The sum of all RMS values is stored by the device, and represents the cumulative error it made in the course of the experiment.

4. As each dOTF WFS represents an obscuration radius, the best fixed obscuration radius can be found by selecting the WFS that minimized the cumulative RMS of its measurements (or equivalently, its mean RMS).

3.6.3 Bright star limit

For atmospheric wavefront sensing, the illumination conditions need to be based on the flux of a suitable target star in the color band that the main telescope is currently using. After all, the role of the wavefront sensor is to generate data of the turbulence in the right spectral domain along a line of sight that intersects with the cylindrical beam through which the main telescope observes.
To find the best attainable performance for atmospheric dOTF WFS, we will consider a sensor targeting one of the brightest stars available in the night sky.

Illumination level derivation

- Vega, or α Lyrae, is the fifth brightest star as seen from Earth during night time and the second brightest star in the northern celestial hemisphere, only after Arcturus.[16] At a wavelength of 500 nm, Vega's specific flux at Earth's surface is approximately F_λ = 1000 photons $s^{-1}\text{cm}^{-2}\mathring{A}^{-1}$. [8] We do not consider attenuation of the intensity by the atmosphere.

- It is reasonable to assume a 5% bandpass filter for our WFS. Assuming total transmittance within the band $[\lambda - \frac{1}{2}\Delta\lambda, \lambda + \frac{1}{2}\Delta\lambda]$ and no transmittance at all outside the band, we simply find $\Delta\lambda = 0.05\lambda = 250\mathring{A}$.

[15] This last assumption is unrealistic, as it would require the sensors to be located at precisely the same location in space, which is hard to do physically.
[16] At least, in the visible domain of the electromagnetic spectrum.

- To enable low-cost, mobile dOTF wavefront sensing devices, the pupil diameter D is projected to be roughly 30 cm, yielding $r_P = 15$ cm.
- One would like to maximize the number of PPPM reconstructions made per unit time, while also keeping up the reconstruction quality. When taking the variability of the atmosphere into account, we would like an AO system and therefore a PPPM reconstruction data stream of 1,000 fps. Therefore, the integration time per reconstruction Δt for a polarizing beamsplitter dOTF WFS design cannot exceed 1 ms.
- We should also take into account that the instrument will have a limited photon efficiency. We assume the feasible value of $\eta = 50\%$.

The expected number of photons that collectively form the image corresponding to the unobscured aperture of a polarizing beamsplitter dOTF WFS, is now given by

$$E_\gamma = F_\lambda \Delta\lambda S_P \Delta t \eta \frac{1}{2} \cdot \frac{1}{2} = \frac{\pi}{4} \eta r_P^2 F_\lambda \Delta\lambda \Delta t \tag{3.24}$$

The two factors of $\frac{1}{2}$ arise as a consequence of the polarizing beamsplitter dOTF WFS design. One factor reflects the fact that the beam of incident photons is split in two, so that two images can be made simultaneously. The other factor takes into account that starlight is unpolarized, and that upon passage of the Wollaston prism only one component of the original polarization directions is transmitted.[17]

For Vega, the expected number of photons per image per integration time is thus found to be $E_\gamma \approx 22,000$ *photons.*

Results: the high $\frac{D}{r_0}$ regime

For $\frac{D}{r_0} = 13$, the algorithm was executed for $n_O = 73$ and $n_W = 500$, leading up to a data grid containing 36,500 dOTF PPPM reconstructions. These can be visualized as shown in Figure 3.4a. It is clear from this plot that certain obscuration radii consistently tend to yield good reconstructions, which are indicated by their green color, despite some slight variations in the reconstructive quality.
One could now 'collapse' this data grid unto the horizontal axis, yielding for each obscuration radius a RMS sample mean and sample standard deviation.[18] The results can be visualized in a scatter plot like Figure 3.4b, from which we can distillate the best fixed obscuration radius for this degree of Kolmogorov turbulence. We find that the best fixed obscuration size is $\frac{D_O}{D} = 23.4\%$.

Results: the low $\frac{D}{r_0}$ regime

For $\frac{D}{r_0} = 2$, the algorithm was executed for $n_O = 31$ and $n_W = 500$, leading up to a data grid containing 15,500 dOTF PPPM reconstructions. These can be visualized as shown in Figure 3.5a. It is clear from this plot that for sufficiently large obscurations, all reconstructions tend to be good.
In contrast to the high turbulence regime, any obscuration radius larger than $\frac{D_O}{D} \approx 25\%$ performs well. Also note the fortunate property that the obscuration radii that minimize the cumulative error of their reconstructions, also minimize the *deviation* in their reconstructive quality. So when the best obscuration radius is taken, we do not only obtain the best reconstructions on average, we also minimize the uncertainty in reconstructive quality.

[17] The attenuation factor of $\frac{1}{2}$ was derived in Section 2.7.2.
[18] This step is the de facto implementation of step 3 of the outlined algorithm.

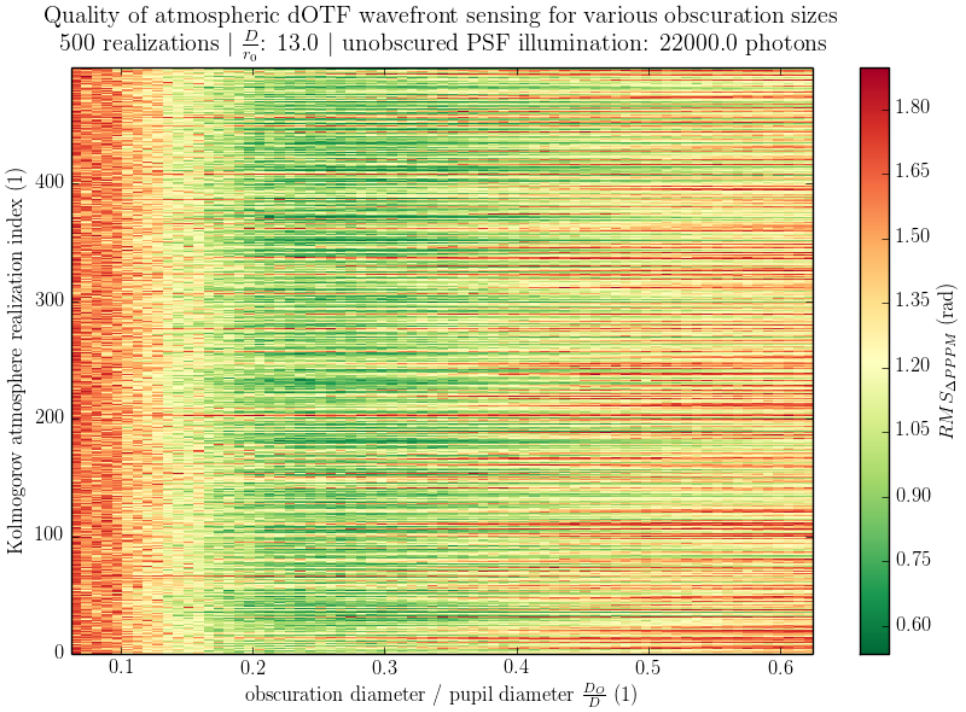

(a) Each reconstruction is visualized in this data grid.

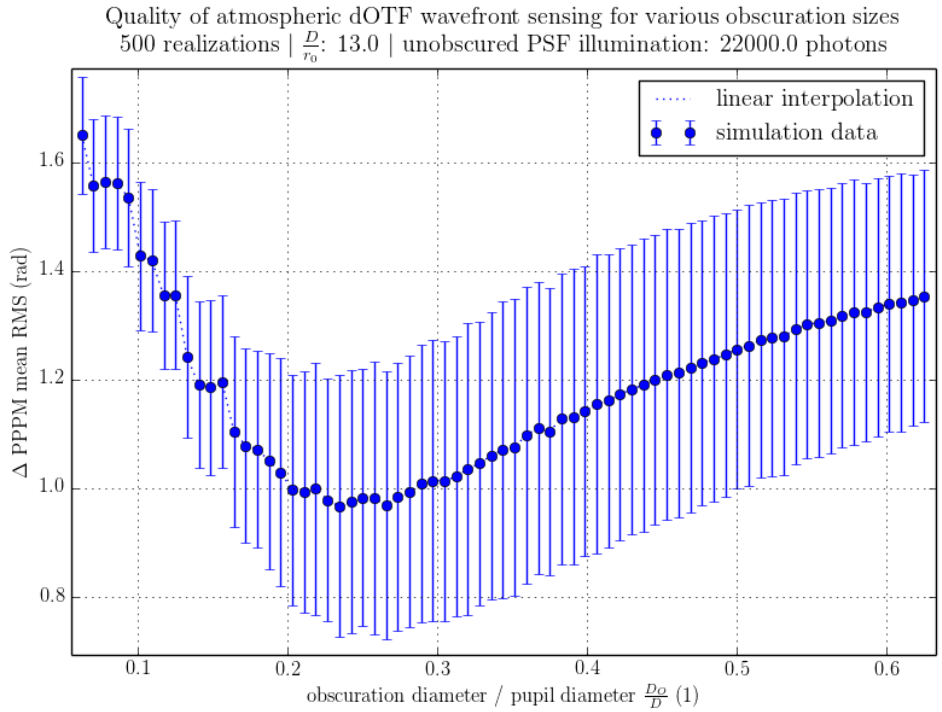

(b) Each column of the data grid is collapsed into a mean RMS ϕ_Δ with standard deviation.

Figure 3.4: Quality overview of $n_W = 500$ PPPM reconstructions performed by $n_O = 73$ different dOTF wavefront sensors observing Vega through a Kolmogorov atmosphere of $\frac{D}{r_0} = 13$.

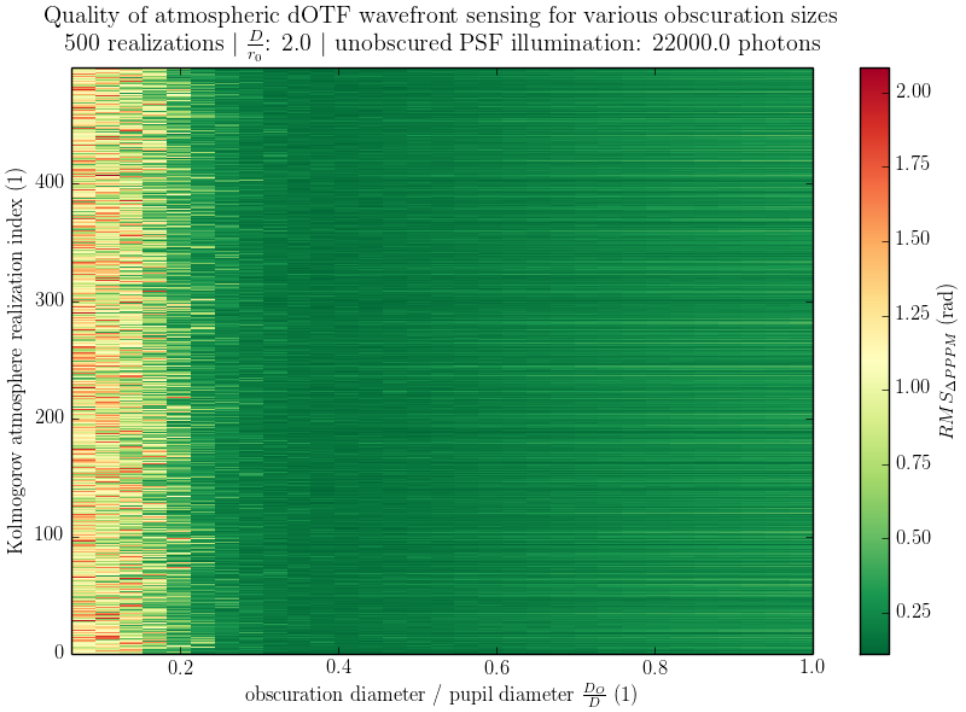

(a) Each reconstruction is visualized in this data grid.

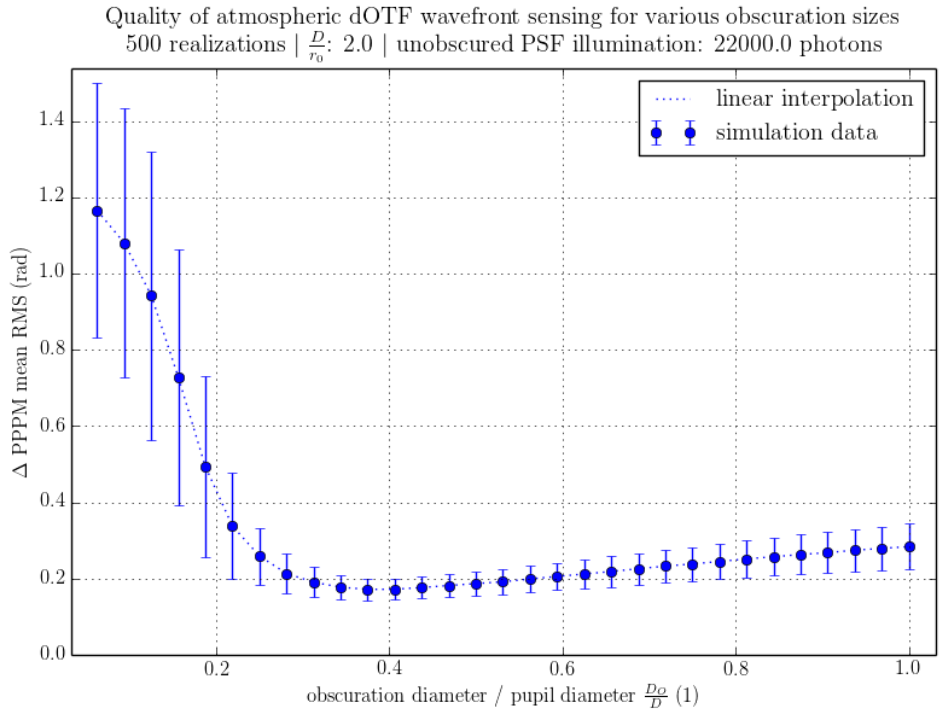

(b) Each column of the data grid is collapsed into a mean RMS ϕ_Δ with standard deviation.

Figure 3.5: Quality overview of $n_W = 500$ PPPM reconstructions performed by $n_O = 31$ different dOTF wavefront sensors observing Vega through a Kolmogorov atmosphere of $\frac{D}{r_0} = 2$.

Results: the complete $\frac{D}{r_0}$ range

The results as shown for $\frac{D}{r_0} = 13$ and 2 can be computed for other values of $\frac{D}{r_0}$ as well, and show the expected intermediate trends.
Upon comparison of Figures 3.4b and 3.5b, it is evident that we are close (within $\approx 10\%$) to optimal performance when an obscuration radius of 30% of the aperture radius is used.

This means that for observing in the bright star limit, we can use a fixed obscuration radius for all levels of atmospheric turbulence.

In a liquid crystal polarizing beamsplitter dOTF WFS design, it is no problem to adapt the obscuration size to the current value of $\frac{D}{r_0}$ to completely optimize the performance. The best obscuration radii for several degrees of atmospheric turbulence are visualized in the graph of Figure 3.6a.
Another way to visualize these data, which would be more appealing to a general audience, is the graphic of Figure 3.6b, that shows the liquid crystal aperture designs that the simulations suggest. The gray area in each aperture represents the disk-shaped obscured region.

3.6.4 Dimmer star targets

In the previous section, we found that for realistic Fried parameter values a fixed obscuration radius of 30% r_P always comes close to maximizing WFS performance. These results apply in the bright star limit - corresponding to the highest illumination levels we could hope for. Obviously, stars as bright as Vega are rare in the night sky, and the technique should also work using dimmer stars. In this section, we inquire which stars could be targeted by the WFS to maintain an acceptable reconstruction quality. Especially, it is relevant to inquire the lower bound to the brightness of stars for this purpose.

Results: the high $\frac{D}{r_0}$ regime

The influence of stellar brightness on the performance of various obscuration sizes is shown in Figure 3.7. We see that for higher illumination levels, the reconstruction improves, regardless of obscuration size. It is apparent though that the largest reconstruction quality gains are obtained for small obscuration radii.
For $\frac{D}{r_0} = 10$, as shown in Figure 3.7a, main results are tabulated below. For each star, the reduction in RMS when going from ϕ_P to ϕ_Δ is given in the rightmost column. The simulations yield that for this level of turbulence the mean RMS of ϕ_P is 1.78 rad.

Apparent visual magnitude m_V	$\langle$RMS$\rangle$ at $\frac{D}{D_O} = 30\%$ (rad)	RMS mitigation (%)
0	0.58	67
1	0.70	61
2	0.93	48
3	1.2	33
4	1.3	27

Whilst 67% wavefront flattening could be reached using a magnitude 0 star, only 27% wavefront flattening is possible using a magnitude 4 star.

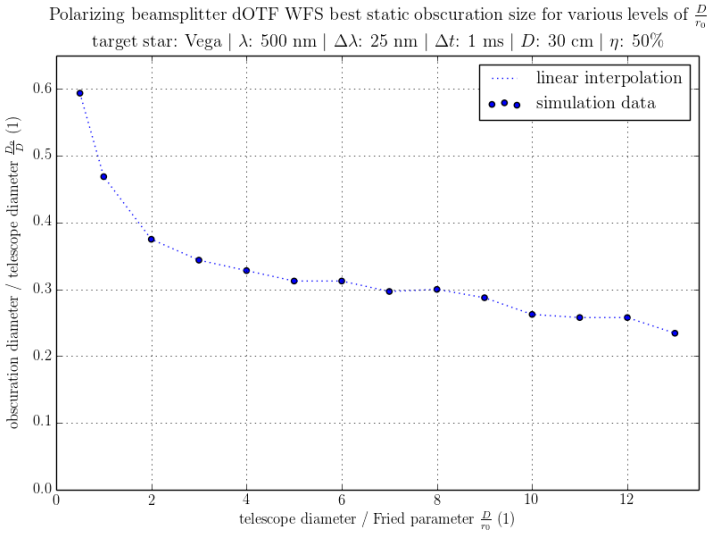

(a) Quantitative form.

Polarizing beamsplitter dOTF WFS aperture designs optimized for various levels of $\frac{D}{r_0}$

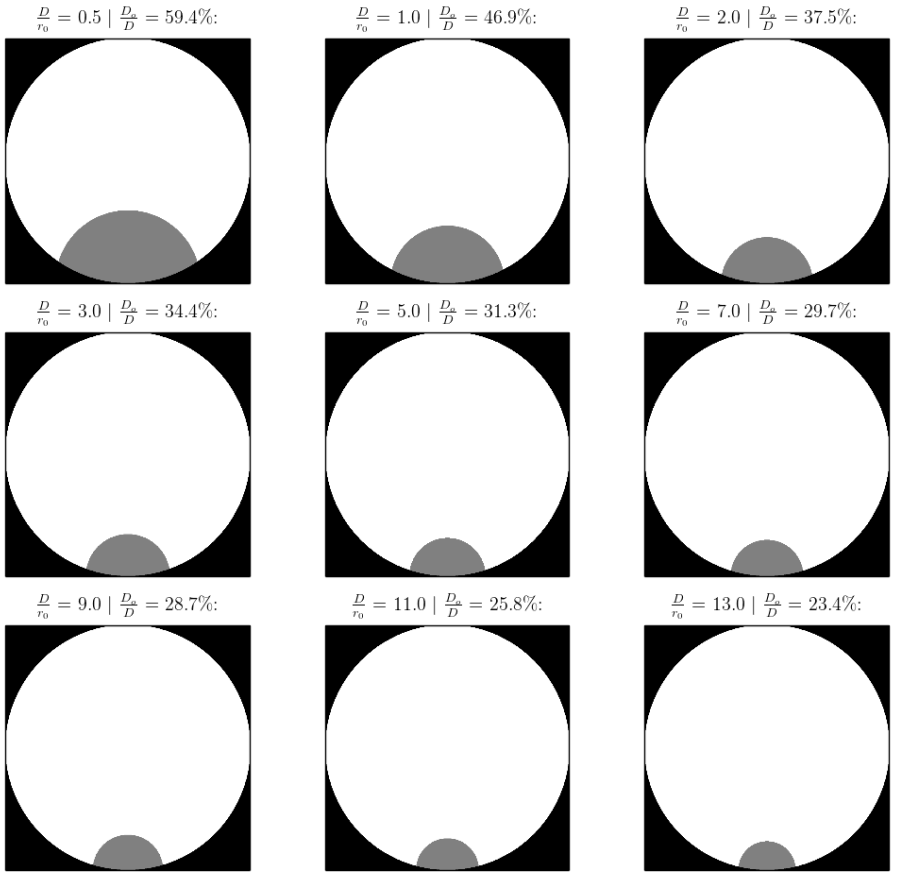

(b) Graphical form.

Figure 3.6: Overview of the best fixed obscuration radii in the bright star limit for various levels of $\frac{D}{r_0}$.

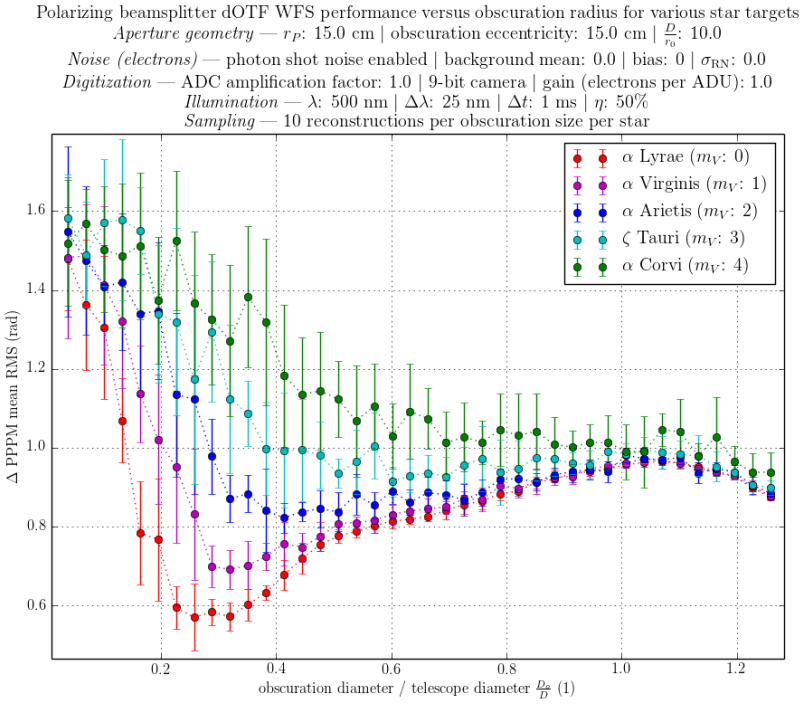

(a) Fried parameter $r_0 = 3.0$ cm.

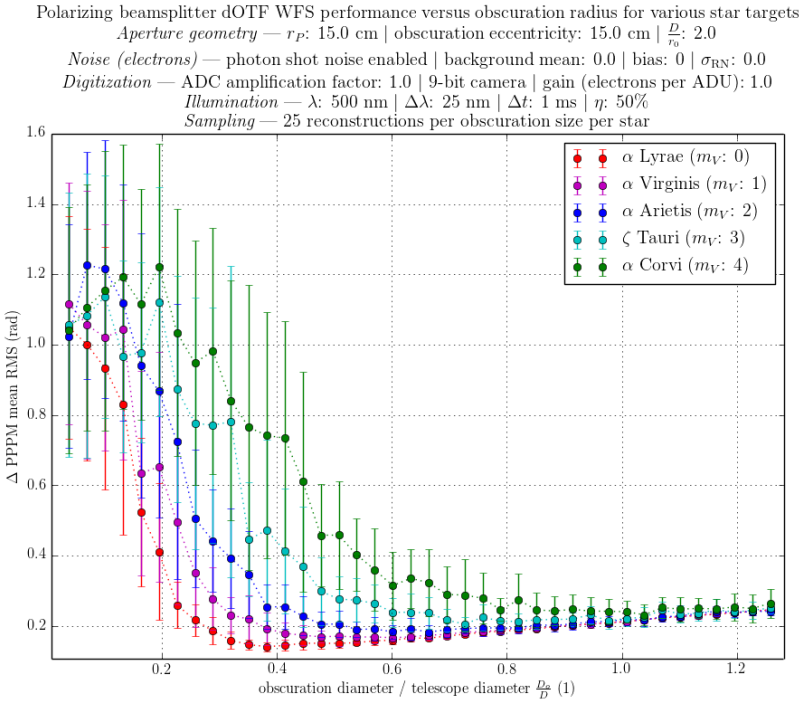

(b) Fried parameter $r_0 = 15.0$ cm.

Figure 3.7: Dependence of the performance of various obscuration sizes on the brightness of the target star in two different turbulent regimes.

Results: the low $\frac{D}{r_0}$ regime

For $\frac{D}{r_0} = 2$, as shown in Figure 3.7b, main results are tabulated below. For each star, the reduction in RMS when going from ϕ_P to ϕ_Δ is given in the rightmost column. The simulations yield that for this level of turbulence the mean RMS of ϕ_P is 1.16 rad.

Apparent visual magnitude m_V	$\langle$RMS$\rangle$ at $\frac{D}{D_O} = 30\%$ (rad)	RMS mitigation (%)
0	0.18	84
1	0.26	78
2	0.43	63
3	0.75	35
4	0.90	22

Whilst 84% wavefront flattening could be reached using a magnitude 0 star, only 22% wavefront flattening is possible using a magnitude 4 star.

Star target abundance

The results clearly show that the WFS quality deteriorates when the same wavefront reconstructions are performed using fainter stars. We should formulate a criterion to decide which stars are regarded as unsuitable for polarizing beamsplitter dOTF WFS. Exemplum gratia, we could say that wavefront sensing activities only still make sense if the attainable wavefront flattening is at least 25%.
For $\frac{D}{r_0} = 10$, this criterion imposes a limit of $m_V = 4.2$ on the brightness of target stars. 780 stars in the night sky are suitable for WFS. The mean solid angle subtended per star is $1.6 \cdot 10^{-2}$ sr. [11]
For $\frac{D}{r_0} = 2$, this criterion imposes a limit of $m_V = 3.7$ on the brightness of target stars. 444 stars in the night sky are suitable for WFS. The mean solid angle subtended per star is $2.8 \cdot 10^{-2}$ sr. [11]

3.7 Adaptive dOTF wavefront sensing

3.7.1 Adapting the obscuration radius as r_0 changes

The results in the previous section culminated into static aperture designs for several values of $\frac{D}{r_0}$. During a night of astronomical observations, the Fried parameter changes, as ground temperature, wind speeds and air humidity evolve. For a wavefront sensor with diameter D, $\frac{D}{r_0}$ will thus change as well. The ideal design of a dOTF WFS would therefore make use of an obscuration that can change in size to optimize its performance for the current value of r_0.[19]

3.7.2 Adapting the obscuration radius for a given r_0

In this section, we will inquire the feasibility of changing the obscuration radius *within* a given value of r_0. In concreto, we will look into adjusting the obscuration radius after each measurement, to prepare the dOTF WFS to maximize its performance for the next.

[19]This could be easily achieved in a design involving liquid crystals to form the obscuration. As the light incident on the crystals should be polarized, and starlight is not in general, this would require a polarization filter that dims the incident radiation. It might turn out that the photon loss that this brings along does not outweigh the merits of having exactly the right obscuration size.

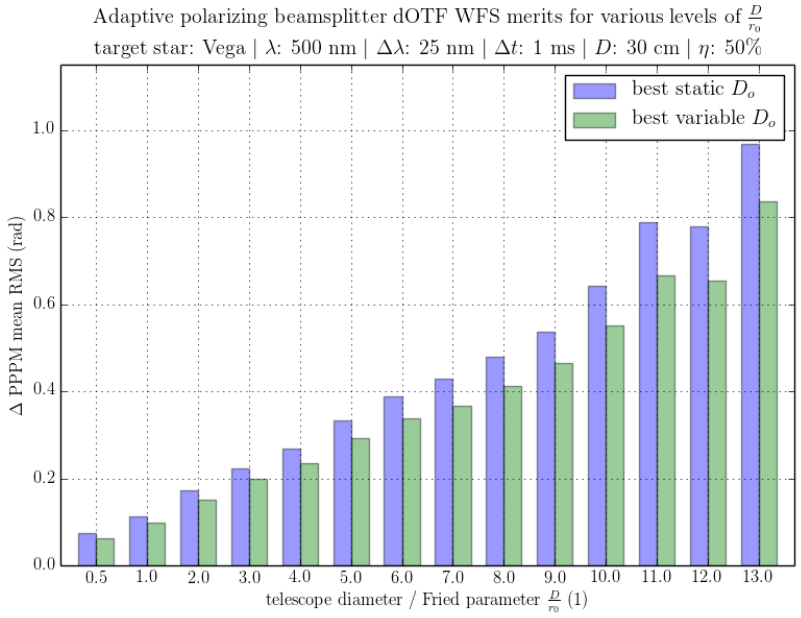

Figure 3.8: Comparison between best fixed obscuration dOTF WFS performance (blue) and ideal adaptive dOTF WFS (green) for several levels of atmospheric turbulence in the bright star limit.

The best possible performance

Let's recall that Figure 3.4a illustrates a data set obtained from measuring n_W wavefronts with n_O dOTF wavefront sensors. Each vertical line represents the n_W measurements done by a single dOTF WFS, while each horizontal line gives n_O reconstructions of the same wavefront, each done with a different device. The best performing dOTF WFS was found by selecting the column whose RMS sum was minimal.

Now assume we pick for each horizontal line the dOTF WFS that made the best reconstruction of that specific wavefront. If we sum up the corresponding RMS values, we get the minimum cumulative error that could possibly have been attained from this data set. Instead of sticking with one column of Figure 3.4a, representing a single dOTF WFS, we constantly hop from column to column as we pass all n_W Kolmogorov realizations.
In the example mentioned, this would be equivalent to first having all dOTF wavefront sensors measure the wavefront at some instant, then selecting (in some way) only the best of the n_O reconstructions as the one that is sent to the telescope, which finally uses DMs to flatten the wavefront with the received data.
In practice, constantly hopping from best performing WFS to WFS would require knowledge of the quality of each reconstruction - which we don't *have* in practice. Continuously choosing the obscuration radius that nails the reconstruction of the current ϕ_P would either require us a lot of luck or objective knowledge of the natural world in the sense only Laplace's Demon possesses.

Adaptive dOTF WFS versus best fixed obscuration dOTF WFS

Whether or not adaptive dOTF WFS is possible in practice, we know that the absolute best performance it could deliver would be expressed by the cumulative RMS of the best reconstruction for each realization - it is the best adaptive dOTF WFS one could ever hope for.
In Figure 3.8, for several values of $\frac{D}{r_0}$ at $E_\gamma = 22,000$ photons, the RMS of ideal adaptive dOTF WFS is compared to the RMS of best fixed obscuration dOTF WFS. The RMS percentage decrease is tabulated below.

$\frac{D}{r_0}$	Approximate upper limit to adaptive dOTF WFS RMS mitigation (%)
0.5	17.1
1	14.3
2	11.5
3	10.5
4	12.6
5	12.1
6	12.7
7	14.6
8	14.1
9	13.3
10	14.3
11	15.6
12	15.9
13	13.6

The gains of adaptive dOTF WFS, even for the most optimistic and unrealistic case of *ideal* obscuration adjustment, are limited to $\approx 15\%$. Depending on the implementation of *practical* adaptive dOTF WFS, the performance might only be marginally better in comparison with best fixed obscuration dOTF WFS.

3.7.3 Quality estimation of a reconstruction

The ability to estimate the quality of a reconstruction is a necessity for adaptive dOTF WFS ,and useful information for best fixed obscuration dOTF WFS. In the simulations, the quality (quantified by the RMS of the difference map ϕ_Δ can be precisely computed, as we know the actual incident wavefront. In practice, ϕ_P is unknown (otherwise we wouldn't have to measure it), and we need to estimate it in another way.
An obvious question would be: *Can we get an idea of the quality of a reconstruction by means of the reconstruction itself?* Exemplum gratia, we could see whether there would be a relation between the RMS of the reconstructed map (which we can always compute) and the RMS of the difference map (which we can only compute in simulations). The RMS of the reconstructed PPPM is denoted RMS_{dOTF}, where the subscript is used to distinguish it from the RMS of the difference map. RMS_{dOTF} is computed in the way outlined in Section 3.5.3.

In Figure 3.9, the reconstruction quality is plotted versus the reconstruction RMS for $\frac{D}{r_0} =$ 0.5 and 13. For each obscuration radius, the $n_W = 500$ data points have the same color. The colors of the smallest and biggest obscuration are indicated in the plot legends; the other colors lie interpolated between these two.
Let's take a look at the upper graph. For small obscuration radii relative to the aperture radius, one could discern a general trend in the measurements: higher reconstruction RMS's are

associated with lower reconstructive qualities. For big obscuration radii relative to the aperture radius, the reconstruction quality is high regardless of the RMS of ϕ_{dOTF}.
For $\frac{D}{r_0} = 13$, the picture changes. The RMS of ϕ_{dOTF} is unrelated to the reconstruction quality.

3.7.4 Adaptive dOTF WFS algorithm

A possible practical implementation of adaptive dOTF WFS would be the following.

1. As a preparation for adaptive dOTF WFS, simulate many (n_W) realizations of Kolmogorov PPPMs for the value of $\frac{D}{r_0}$ that corresponds to the current skies, so that graphs like in Figure 3.9 can be made.

2. Graphs as in Figure 3.9 show RMS ϕ_Δ and RMS ϕ_{dOTF} for all obscuration radii simultaneously, but we could of course also make graphs for each obscuration radius individually. Fit lines of the form $y = ax + b$ through the n_O resulting scatter plots, that approximate the trend between RMS ϕ_Δ and RMS ϕ_{dOTF} for that specific obscuration radius.[20]

3. Armed with the possibility to predict the reconstruction quality for every obscuration radius given some reconstruction RMS, we start the actual observations. We might e.g. start out at the best fixed obscuration radius for the relevant value of $\frac{D}{r_0}$.

4. After each PPPM reconstruction is made, calculate the reconstruction RMS.

5. Using the reconstruction RMS, we can use the polynomial approximation we computed using our simulations to calculate the suspected reconstruction quality.

6. Now, we change the obscuration radius by a small amount Δr_O. At first, there is 50% chance to increase the obscuration radius to $r_O + \Delta r_O$ and 50% chance to increase the obscuration radius to $r_O - \Delta r_O$.

7. We perform another PPPM measurement using the new obscuration radius. Again, we calculate the reconstruction RMS and use it to obtain an indication of the reconstruction quality.

8. If the suspected new reconstruction quality is higher than the suspected old reconstruction quality (quantitatively, we think RMS ϕ_Δ has decreased), we have probably adjusted the obscuration in the right way. Based on this, the odds for going to smaller and bigger obscuration radii for the next iteration will change. If e.g. the obscuration radius increased with the step size Δr_O, and this indeed likely lowered RMS ϕ_Δ, the probability to increase the obscuration for the next iteration will be increased from its current value of 50%.

9. Utilizing the new binary probability distribution, we take a random draw that decides whether we increase or decrease the obscuration radius. We perform another measurement, assess the reconstruction quality, compare it with the previous supposed reconstruction quality, and alter the obscuration adjustment probability distribution again. This distribution should be based on the successes and failures of the obscuration adjustment effectuations of the last few iterations.

[20] Although the use of linear approximations is proposed here, polynomials of higher degrees could be used as well.

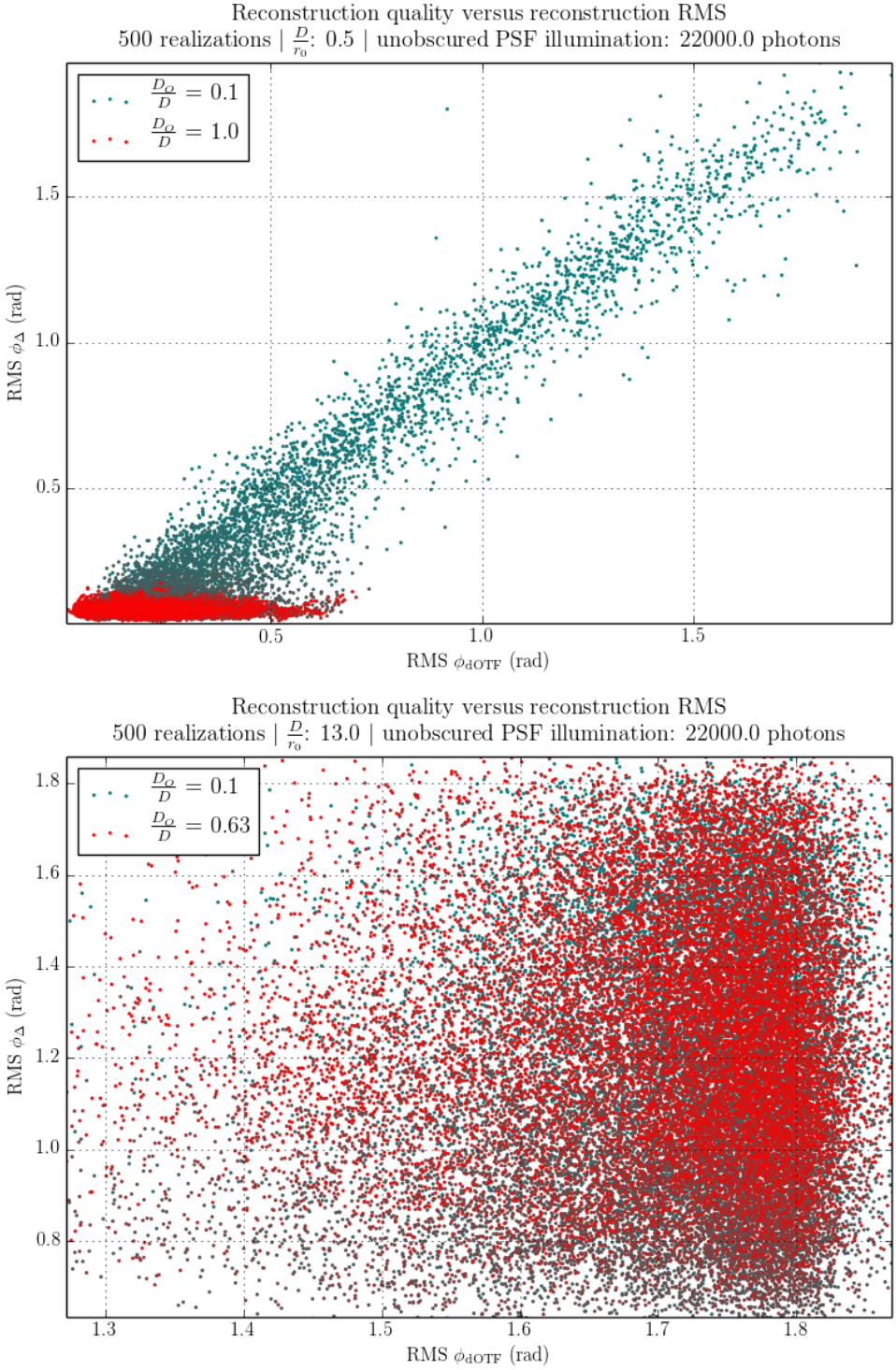

Figure 3.9: Relation between reconstruction quality and reconstruction RMS for several obscuration sizes, visually differentiated by their color. $\frac{D}{r_0} = 0.5$: 15,500 data points in total ($n_W = 500$ and $n_O = 31$). $\frac{D}{r_0} = 13$: 36,500 data points in total ($n_W = 500$ and $n_O = 73$).

10. In this way, we hope that the dOTF WFS adjusts its obscuration size to maximize its performance. Due to the randomness that is deliberately added to the algorithm, I hope that the dOTF WFS finds the most appropriate obscuration radius all the time.[21]

Unfortunately, due to limited project time and the unlikely feasibility of adaptive dOTF WFS, I did not implemented a test of this algorithm.
Its main message though is that adaptive dOTF WFS is not only a theoretical exercise, but a technique that could be put into practice.

[21] For this algorithm, I was inspired by the way bacteria hunt for food. Many bacteria have flagella that allow them to move around. The flagella of a bacterium change their orientation at random time intervals, causing the cell's direction of motion to change. Basically, this means that the cell's path will be a chaotic, random wander through the liquid it is immersed in. But whenever the bacterium detects a gradient in the concentration of nutrients, it alters the mean time between two orientation changes of its flagella. Whenever a nutrient increase is detected, the mean time is elongated; whenever a nutrient decrease is detected, the mean time is contracted. The net effect is that bacteria move towards places where high concentrations of food are present. Due to the fact that their motion is still random, they are also able to get around obstacles that hinder the direct route to their apparent destination.

Chapter 4

Laboratory experiments

4.1 Overview

In this chapter, I will discuss the lab work that has been done to test dOTF wavefront sensing using both a metal obscuration and an obscuration of polarized material.

Essentially, this chapter is structured in the same way as Chapter 2 and Chapter 3 were structured. First, it will be discussed how the Airy disk can be obtained. This time, we will not aim for a mathematical description nor a numerical map, but for lab images containing the characteristic pattern. Then, we will discuss general steps that lead up to a dOTF reconstruction of ϕ_P. Finally, laboratory results will be shown of dOTF PPPM reconstructions where the obscuration is implemented in various ways, ordered by their level of sophistication:

1. *A metal obscuration,* requiring manual insertion and removal, and sequential generation of the images with obscured and unobscured aperture.
2. *A polarized obscuration,* requiring manual polarizer rotation, and sequential generation of the images with obscured and unobscured aperture.
3. *A polarized obscuration,* requiring no moving parts, and enables simultaneous generation of the images with obscured and unobscured aperture.

4.2 Imaging the Airy pattern

The cornerstone of dOTF wavefront sensing is the ability to image the Airy pattern, the intensity profile at the focal plane of an imaging system generated by a point source at infinity whose unperturbed flat wavefronts fall through a circular aperture. The essential ingredients of my initial setup are therefore a circular aperture, a convex lens and a camera. I eventually used the following setup.

4.2.1 Initial setup

All components are listed in the order that corresponds to the path of light from source to detector.

1. *A monochromatic laser* was used as a source of approximately collimated light rays.

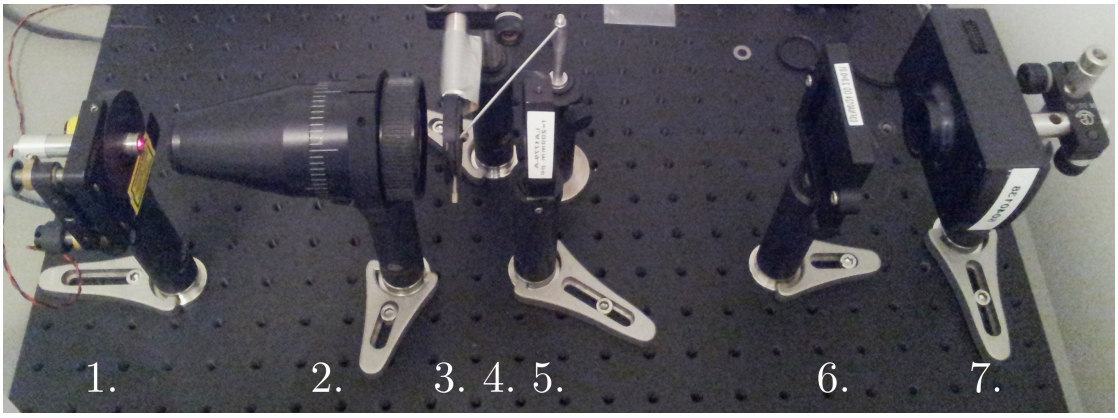

Figure 4.1: Setup for metal obscuration dOTF WFS. 1. laser; 2. beam expander; 3. aperture; 4. metal stick as obscuration, not used initially; 5. convex lens; 6. ND filter; 7. CCD camera.

2. The cross section of the laser beam exhibits a non-uniform intensity profile. The intensity decreases towards the edges of the beam, while we would ideally like to illuminate the aperture homogeneously.
   For this reason, the next element on the optical table is *a beam expander*, that has the effect of enlarging the laser beam cross section. As the aperture only 'sees' the central region of the beam, the beam expander has a homogenizing effect on the radiation field incident at the pupil plane.

3. *The aperture* is made by several partially overlapping blades that collectively form an approximately circular pupil. The aperture radius can be varied in size as the blades can rotate.

4. For making one of the two PSFs necessary for dOTF WFS, *an obscuration* is needed. In this setup, the obscuration is formed by the tip of a metal stick, which is placed as close as possible to the aperture.

5. After the light passes through the aperture, where it diffracts at the edges, it reaches *a convex lens* that focusses the light.

6. *A neutral density filter* (ND filter) was placed to attenuate the intense laser radiation. Without the ND filter, a large swath of detector pixels would be saturated even for the lowest supported CCD integration time of 1 millisecond.

7. *A CCD camera* was placed in the focal plane of the lens.

The setup is shown in Figure 4.1.

Laser properties

The laser emitted monochromatic linearly polarized light in the visible domain of wavelength $\lambda = 635$ nm. The polarizing property of the laser is not a design criterium, but an effect due to the use of a Brewster window, as is the case for many lasers. The apparatus did not offer a feature to attenuate the light at the source, and thus allowed for just two levels of radiative

power (on at 1 mW and off). The model of the laser diode module is named Thor Labs CPS 240.[1] The device was powered by a Thor Labs LDS1 5 VDC regulated power supply.

Lens properties

The lens used was a Thor Labs plano-convex lens with focal length of 200.0 mm. The specific model was named LA1979-A.

Neutral density filter properties

The ND filter utilized in the setup had an optical density (OD) of 2.0 for the wavelength of the laser light. The fraction of photons still transmitted by the filter is $10^{-\mathrm{OD}} = 0.01$.

Camera properties

The camera used in this research was a Lu125M (from *Lumenera Corporation*), a monochromatic 10-bit CCD camera able to make images up to 1280 x 1024 pixels. Each pixel measures 6.7 μm x 6.7 μm. At maximum resolution, the camera could attain a frame rate of 15 frames per second (fps), while 60 fps can be reached at a resolution of 640 x 480 pixels. The detector did not feature a shutter. The camera was USB bus powered, and delivered uncompressed images over the USB 2.0 digital interface to a Windows 7 controlled computer. Driver software could be used to change camera settings such as gain, integration time and resolution.

4.2.2 Outlining the setup

Outlining procedure

1. Outlining the setup started with placing the laser and the camera in correct orientation with respect to each other. This turned out to be surprisingly simple. When laser light shines on the pixels of the detector, light is reflected back. Thus, a regular pattern of reflections shines on the wall of the dark laboratory, as can be seen in Figure 4.2. Each reflection spot represents a single pixel. The brightest spot corresponds to the pixel that is hit most directly by the laser beam. Therefore, the detector is oriented perpendicular to the incident beam if the brightest reflection shines its rays back as close as possible to the beam emitted by the laser source. Ideally, the reflected beam should re-enter the laser source.

2. After this alignment step, the CCD chip might be perpendicular to the incoming laser beam, but we might still shift the camera in the plane it resides. This allows us to ensure that the laser beam hits the central part of the CCD chip, so that all visible Airy rings are completely caught by the camera.

3. Next, the aperture was installed, followed by the beam expander. Incorporation of these elements should not change the location of the laser beam on the detector chip.

4. Then, the convex lens was installed at a focal length distance from the camera. The position and orientation of the lens relative to the incident laser beam was adjusted until the lens made the tiniest spot possible at the center of the CCD chip.

5. Finally, the ND filter was installed. By placing this element at the end, the bright spot generated by the laser on the chip remains easily visible during the previous outlining steps.

[1] This model is not sold anymore. Its replacement is called CPS 180.

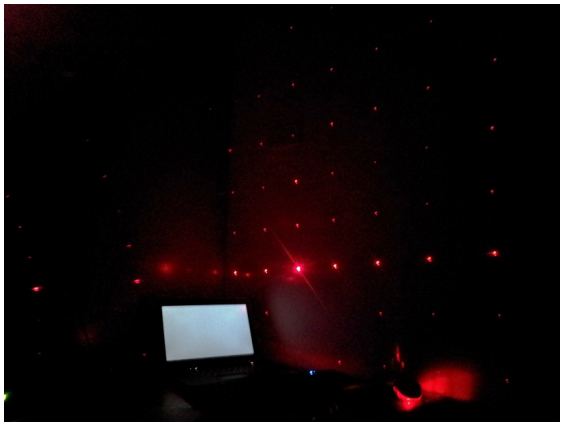

Figure 4.2: The first step in the outlining process of a simple imaging system entails perpendicular orientation of the laser beam on the detector chip. Due to the regular structure of pixels on the CCD chip, a pattern of reflection dots appear at the opposite laboratory wall, which can be used to outline laser and camera.

Outlining feedback

A very handy tool was written in `Python` that allows the user to continuously receive feedback on the quality of the alignment of the optical elements.[2] The outlining routine commands the camera to continuously make images using an integration time ad libitum. These images are then shown on a computer screen, so that video feedback is attained. By using long integration times ($\sim 500\ ms$), more and more outer Airy rings appear, and we can make sure they all fall on detector pixels. By using short integration times ($\sim 100\ ms$), the video feedback is more responsive of alignment adjustments due to the higher fps, although less features of the Airy pattern are visible.

4.2.3 Data reduction

Having made a proper setup, the first images of saturated point spread functions were obtained. As a standard procedure for processing digital images, routines for master bias and master flat creation were developed.

Master bias creation

As has been explained in Chapter 3, the bias voltage gives rise to an artificial signal in the final images as sent from camera to computer. To correct the images for this signal, a master bias should be subtracted. A master bias is a digital image containing an approximation of the statistical mean of the bias level in ADUs, for each pixel individually. By subtracting the master bias, we thus hope to remove any *systematic effects* of bias from the images, so that only random bias *fluctuations* remain that might cancel out when multiple images are combined together.[3]

As a master bias should contain no signal from the outside world, the laser was turned off, alongside all other present light sources. n_B bias frames were taken, using the shortest possible

[2] See LuCamOutline.py in the Code library section.
[3] Addition of several images to cancel out noise sources, is discussed later.

integration time of 1 ms. The higher n_B, the better; in this research I mostly used $n_B \sim 50$.

To form a master bias using n_B bias frames, I developed a `Python` sigma clipping routine. The idea behind this procedure is that the master bias should be the mean of n_B images, where outliers are removed first. An outline of the algorithm is now given.

1. First we combine the n_B images that have M rows and N columns each into an image cube $\mathscr{I}$, which we regard as a three-dimensional cube of voxels that extends N pixels into the x-direction, M into the y-direction, and n_B into the z-direction. For $n_B = 50$, $M = 1024$ and $N = 1280$, the image cube thus contains 65,536,000 voxels.

2. If we travel along the z-direction for a fixed set of image coordinates (x, y), we pass along a stack of values, attained at that pixel position by different frames. Now for every such stack $\{(x, y, 0), (x, y, 1), ..., (x, y, n_B - 1)\}$, we do the following until convergence is reached:

   (a) Determine the stack median $m(x, y)$ and standard deviation $\sigma(x, y)$.

   (b) Throw away all values from the stack that lie further away from the median than some predefined number of standard deviations n_σ.[4] In concreto, let z pass the values $\{0, 1, ..., n_B - 1\}$, and throw away the data point $\mathscr{I}(x, y, z)$ if $|\mathscr{I}(x, y, z) - m(x, y)| > n_\sigma \sigma(x, y)$.

   (c) Let's assume we have removed n outliers in this way, where $n \geqslant 0$.
   If $n > 0$, a trimmed stack remains whose median and standard deviation will be different than they were before. We perform another iteration of data selection.
   In case $n = 0$, the sigma clipping procedure did not remove any values from the stack. The median and standard deviation therefore remain unchanged and doing another iteration would be pointless, for it would again not remove any data points. We say that convergence is reached for this stack.

3. After convergence is reached for all stacks, the image cube will have lost many of its voxels. From a solid block, it has gone to a shaky structure with cavities everywhere. Now we collapse the structure altogether, by computing the mean $\mu(x, y)$ along the z-axis for every trimmed stack.[5] The resulting map is the master bias $B(x, y)$.

Master flat creation

Where the master bias reflects pixel-dependent systematic offsets in an image caused *in absence* of light, the master flat reflects pixel-dependent systematic deviations in pixel sensitivity *in presence* of light. These deviations might occur due to CCD fabrication flaws or tiny dust speckles on the optics of the imaging system. We can correct pixels that have a low sensitivity by digitally amplifying their signal, while we can tune down the signal of pixels that have higher sensitivity than average.
The master flat creation routine is straightforward:

1. Take n_F flat fields, where it is important that the CCD is lit homogeneously. For this reason, we should not use the laser - it produces approximately an Airy pattern on the detector chip. We also cannot just use the laboratory lighting, as the illumination comes from above in this case, resulting in shadows cast on the CCD. My practical solution

[4] I arbitrarily decided on $n_\sigma = 3$ for the master biases created in this research.

[5] It is considerably better to use the mean $\mu(x, y)$ here instead of the median $m(x, y)$. By definition, the median can only attain integer and half-integer values, as the values presented in each stack are integers - they represent ADUs. The mean is able to get closer to the center of the approximately normal distributed bias values.

involved placing a smartphone with a blank screen on the optical axis, covered by a thin plastic bag, so that the outgoing light was diffusely scattered in many directions.
To reduce noise, the flat field integration time Δt_F was chosen as long as possible, while avoiding saturation.

2. $B(x, y)$ was subtracted from each of the n_F flat fields.

3. The flat fields were combined by addition to form a cumulative map, that contains the total number of photons caught by each pixel (x, y) during a time $n_F \Delta t_F$.

4. Now, the cumulative map is divided by its mean, so that the resulting map expresses for each pixel the susceptibility to photon detection relative to the mean susceptibility of the map. This is the master flat $F(x, y)$.

Regular imaging: the problem

As mentioned before, the images produced by the camera resemble *saturated* Airy patterns, at least for sufficiently long integration times Δt. If Δt is decreased until the Airy peak is unsaturated, all ring-shaped structures around the central maximum vanish. For dOTF PPPM reconstruction though, we need the ability to measure complete Airy patterns, containing both peaks and the much fainter concentric rings.
Although the camera used has a bit depth of 10, and thus should enable the detection of $2^{\mathrm{bbp}} = 2^{10} = 1024$ different intensity levels, I found that the CCD saturated already at a level of $N_{D,\mathrm{sat}} \sim 700$ ADU. The effective dynamic range was therefore just around 68% of the claimed value.
It can be reasoned that under these circumstances, it is nearly impossible to image the Airy disk accurately with a single frame. Namely, suppose we tuned Δt perfectly so that the Airy peak signal level was $N_{D,\mathrm{sat}}$, just on the verge of saturation. Also suppose that the detector was placed precisely in the focal plane of the lens, so that no defocus is present and an Airy pattern is realized. In this case, the intensity is concentrated to the maximum attainable level wave optics allows. In Chapter 2, it was discussed that the maximum intensity of the first Airy ring relative to the peak was 1.75%. In this example, this amounts to $0.0175\ N_{D,\mathrm{sat}} \approx 12$ ADU. Photon shot noise is always present, and even without inclusion of any other noise source the signal-to-noise ratio for the most intensely lit pixels of the first Airy ring is just $\sqrt{12} = 3.5$. In practice, the signal-to-noise ratio for this ring will be even lower, and outer rings will not be visible at all. See Figure 4.3 for a realistic simulation.

High dynamic range imaging: simple stacking

Therefore, as a single image will not be sufficient to probe the Airy pattern, we need to collect multiple images and digitally combine them to boost each pixel's signal-to-noise ratio. For this, I implemented a simple algorithm, which I call *simple stacking*.

1. Make n_I images, each of integration time Δt. Δt is chosen such that the combination of Airy peak and bias does not exceed $N_{D,\mathrm{sat}}$.

2. Reduce each image by master bias subtraction and master flat division to obtain a final image $N_D(x, y)$. In concreto,

$$N_D(x, y) = \frac{N'_D(x, y) - B(x, y)}{F(x, y)} \tag{4.1}$$

where $N'_D(x, y)$ is the raw image.

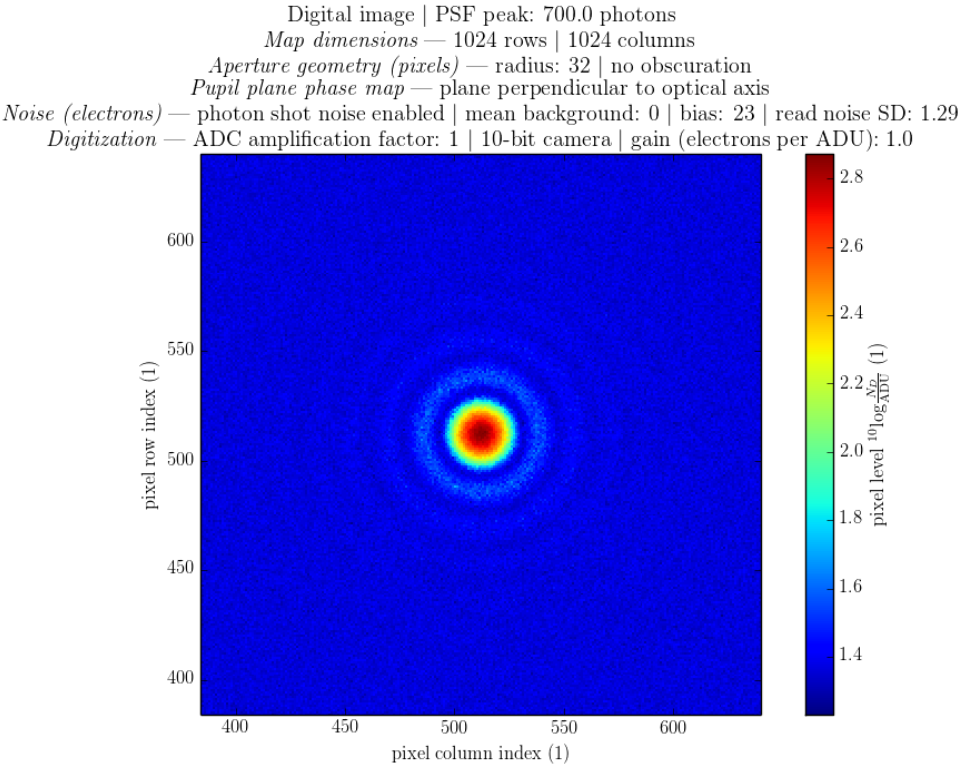

Figure 4.3: Logarithmic plot of a simulated image of the best attainable unsaturated Airy pattern using the 10-bits camera in my setup. We assume Δt is tuned just right so that $\mathrm{PSF}_\gamma(x_{\max}, y_{\max}) = N_{D,\mathrm{sat}}$ and use bias and read noise values from measurements. We assume that the aperture is circular, a flat wavefront perpendicular to the optical axis is incident at the pupil plane, no instrumental aberrations are present and there are no electrons due to CCD lattice vibrations nor background photons. Even under these mild conditions, the first Airy ring is very faint.

3. Combines the n_I frames by addition to form a cumulative map. The hope is that random noise fluctuations will cancel out, while the systematic signal of Airy pattern photons keeps adding up, revealing more Airy rings as n_I is increased.

This approach was unsuccessful, as no additional Airy rings were revealed with the method, even when hundreds of images were combined. No explanation was found as to why this approach did not work.

High dynamic range imaging: selective stacking

Another method of HDRI was then employed, which I call *selective stacking*. In this method, I did not sum many images of a *single* integration time Δt, but first defined a range of n_t different integration times $\{\Delta t_0, \Delta t_1, ..., \Delta t_{n_t-1}\}$ and took n_I images for each of them. Short exposure times were used to probe the Airy peak, while long exposure images were utilized to reveal the Airy rings.
Now follows a concise description of the algorithm.

1. The range of integration times was generated as a geometric progression (also called a *geometric sequence*) with common ratio ξ, so that $\{\Delta t_0, \Delta t_1, ..., \Delta t_{n_t-1}\} = \{\Delta t_0, \xi\Delta t_0, ..., \xi^{n_t-1}\Delta t_0\}$.

2. For each integration time, n_I images were made.

3. All of the $n_I \times n_t$ images were then reduced in the way of Equation 4.1.

4. For each image, all pixel values above some threshold value $N_{D,\text{thres}}$ were thrown away. These are regarded as saturated, or lacking linear scaling with respect to exposure time. The rest of the pixel values were then employed for image stacking.

5. To obtain comparable signals representing 1 milliseconds of integration each, each pixel selected for stacking was divided by its frame's integration time (in ms).

6. A cumulative image was formed.

7. The value at each pixel coordinate (x, y) of this image was then divided by the number of values that contributed to it. After this normalization, we have obtained an image of 1 ms exposure time that contains all features of the PSF realization we wanted to map.

For atmospheric dOTF WFS, it is important that PPPM reconstructions can be made in short succession. Thus, the total integration time necessary to build a single realization of the PSF, should be limited. Using the approach outlined above, probing one PSF takes at least

$$\Delta t \equiv \sum_{i=0}^{n_t-1} n_I \Delta t_i = n_I \sum_{i=0}^{n_t-1} \xi^i \Delta t_0 = n_I \Delta t_0 \frac{1-\xi^{n_t}}{1-\xi} \tag{4.2}$$

This method was successful, and realizations of Airy patterns were obtained.

4.3 dOTF PPPM recovery: general

Now the methods have been discussed that enable the imaging of arbitrary intensity patterns, it is time to discuss in general how a dOTF PPPM reconstruction is done in the lab and how we can check whether it makes sense.

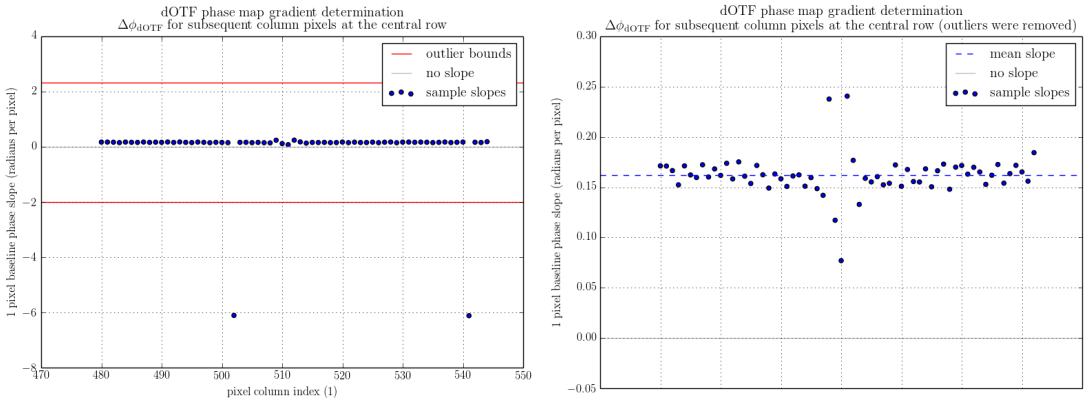

(a) (b)

Figure 4.4: Lab dOTF PPPM gradient determination procedure. Left: per pixel phase differences are plotted. The outliers are due to phase wrapping. Right: per pixel phase differences with outliers removed.

4.3.1 Computing A_{dOTF} and ϕ_{dOTF}

The images were first cut to form squares. The OTFs of images with unequal dimensions have different spatial frequency spacing, and therefore the dOTF as well. The result would be an elongated dOTF PPAM and PPPM.
Next the methods described in Section 2.7 are used to obtain A_{dOTF} and ϕ_{dOTF}. These maps contain information on the aperture and incident wavefront. Examples of how these look like are shown in Figure 4.5a and 4.5b respectively.

4.3.2 ϕ_{dOTF} gradient removal

Unless the setup is outlined perfectly, the reconstructed pupil plane phase map will contain a phase gradient as the detector surface will never be perfectly perpendicular to the optical axis. Although a gradient in ϕ_{dOTF} could also represent a genuine feature of ϕ_P, it is in my setups most likely attributable to an alignment error. Therefore, we remove it.
The procedure that is used is the following:

1. To determine the phase gradient aberration ϕ'_P, we determine the two components of the gradient vector $(\vec{\nabla}\phi'_P)_x$ and $(\vec{\nabla}\phi'_P)_y$. We discuss the determination of $(\vec{\nabla}\phi'_P)_x$; the other component is found analogously.

2. To determine the gradient in the column direction, a sample of pixels $\{(x_P - r_S + 1, y_P), (x_P - r_S + 2, y_P), ..., (x_P + r_S + 1, y_P)\}$ is taken, where r_S is some arbitrary 'radius' determining the number of pixels present in the sample $(2r_S + 1)$. For each pixel (x, y_P) in the sample, the phase difference $\Delta\phi_{\mathrm{dOTF}}(x, y_P)$ with the pixel left of it is computed. An overview of these one-pixel baseline gradient component approximations is shown in Figure 4.4a.

3. The standard deviation of the set $\{\Delta\phi_{\mathrm{dOTF}}(x_P - r_S + 1, y_P), ..., \Delta\phi_{\mathrm{dOTF}}(x_P + r_S + 1, y_P)$ is computed. All $\Delta\phi_{\mathrm{dOTF}}(x, y_P)$ that lie further than n_σ standard deviations away from the median value of the set, are regarded as outliers and removed from the sample.[6] The

[6] Quite arbitrarily, I settled on $n_\sigma = 2$ to generate research results.

remaining values are plotted in Figure 4.4b.

4. $(\vec{\nabla}\phi'_P)_x$ is found by taking the mean slope from this selection.

When $\vec{\nabla}\phi'_P$ is found, the gradient is subtracted from the dOTF PPPM and the underlying pattern is revealed. Exemplum gratia, compare Figures 4.5b and 4.5d.

4.3.3 Finding the aperture center

Now the 'true' dOTF PPPM is revealed, it is desirable to find out which values of the map are sensible approximations of ϕ_P. Ideally, we would like to cut out the region from the dOTF PPPM that corresponds to the aperture region, so that I could unambiguously provide you the phase value relative to some reference point for each position of the aperture. This requires us to find the center of the aperture and its radius.

Clipped aperture

To start the procedure of determining the aperture position and radius, an aperture approximation is computed from the measurements by clipping the dOTF PPAM at some arbitrary value. In this way, Figure 4.5c was generated from Figure 4.5a.

Model aperture

To find the center and radius of the aperture from the clipped aperture map, we perform a fitting procedure. We vary r_P and offsets Δx and Δy, corresponding to aperture centers $(x_C - \Delta x, y_C - \Delta y)$ and $(x_C + \Delta x, y_C + \Delta y)$, and calculate the model aperture map this would result in. The clipped aperture and model aperture are compared and the best model is selected as the map that looks most like the clipped aperture map. An example of the resulting fitted aperture is shown in Figure 4.5e.

4.3.4 Obtaining the final ϕ_{dOTF}

By knowing the aperture centers and radius, we can cut out the useful part of the dOTF PPPM. We arbitrarily choose one of the aperture centers and mask out all values that lie outside the aperture disk. Additionally, the overlap region is excluded as it does not contain reliable phase information. As the dOTF PPPM contains an arbitrary piston and the RMS of a phase map is piston-dependent due to phase wrapping, we shift the map as a last step in such a way that its RMS is minimized. A result akin to Figure 4.5f is obtained.

4.3.5 Validating the technique

In the simulations we could compare ϕ_{dOTF} with ϕ_P to see how good the reconstruction is. In reality, ϕ_P is unknown and so we cannot use this method to verify that our dOTF WFS is working.
The following tests have been conceived to validate the technique without knowing ϕ_P:

- If the obscuration would be placed at the other side of the pupil, the orientation of the partially merging disks and thus also the location of the overlap region will be mirrored.
- If two measurements of the unobscured PSF are used for dOTF WFS, results inconsistent with a dOTF reconstruction should emerge. For example, the dOTF PPAM should not resemble two partially overlapping disks.

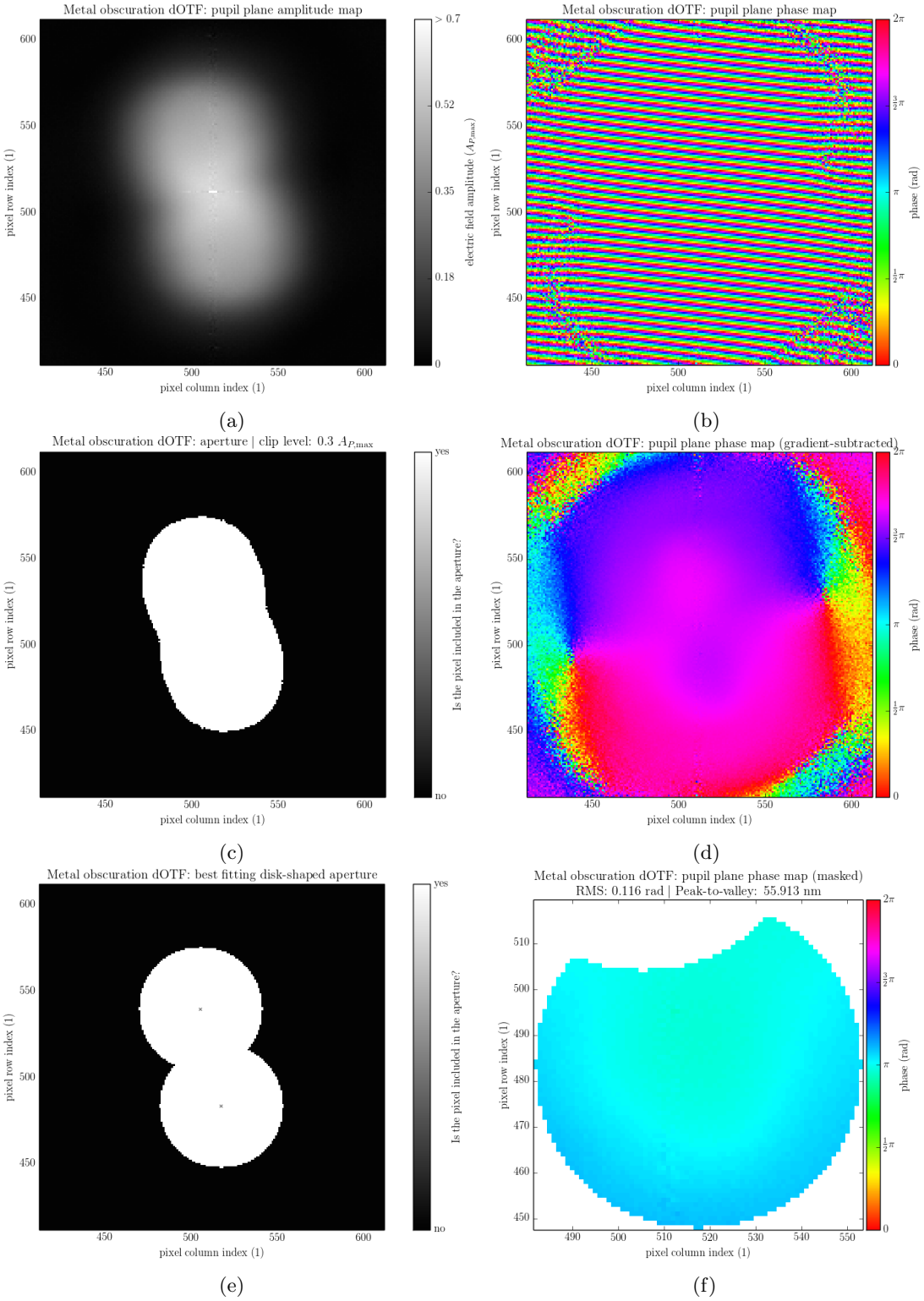

Figure 4.5: Overview of all important lab dOTF reconstruction steps. Metal obscuration defocused dOTF using selective stacking parameters $\Delta t_0 = 1.0$ ms, $\xi = 2$, $n_t = 11$ and $n_I = 1$.

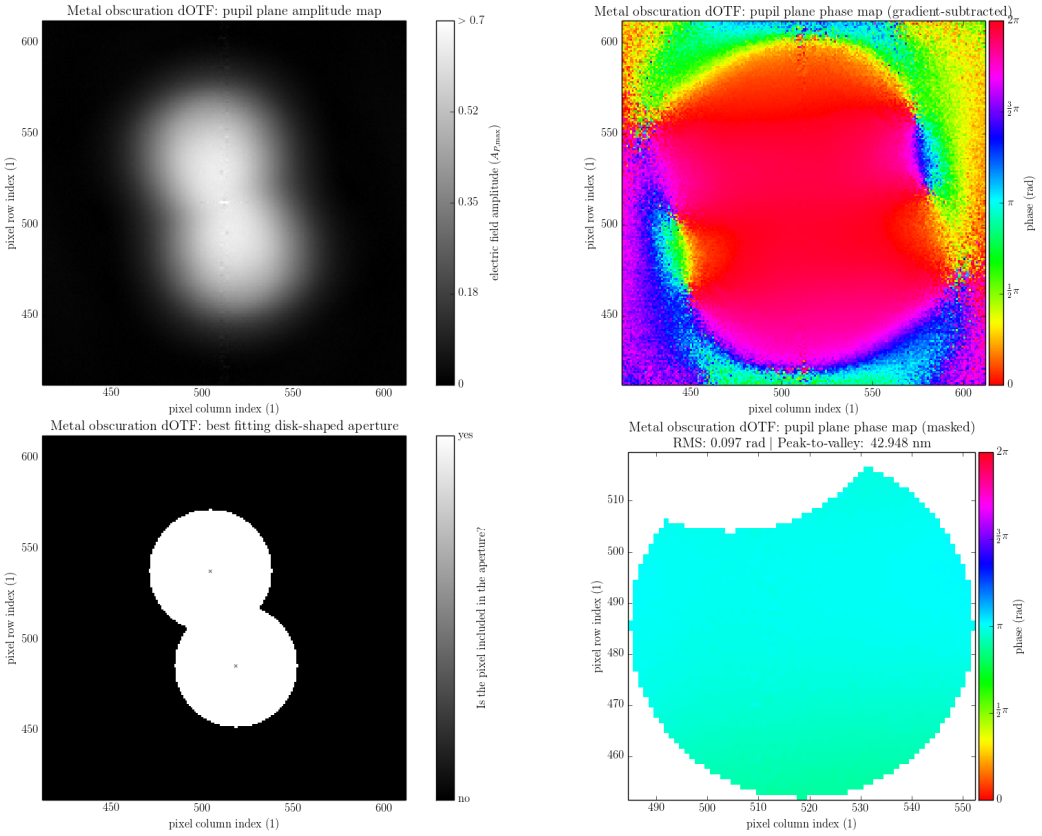

Figure 4.6: Metal obscuration dOTF using selective stacking HDRI parameters $\Delta t_0 = 1.0$ ms, $\xi = 2$, $n_t = 11$ and $n_I = 1$.

- If defocus is deliberately added to the setup by changing the lens position, defocus should emerge in the dOTF PPPM.

4.4 dOTF PPPM recovery: metal obscuration

The initial setup was meant to do dOTF wavefront sensing using a metal obscuration that needs to be placed and removed by hand. A demonstration of a dOTF reconstruction using this setup was already shown in Figure 4.5. In this section, some more results follow.

4.4.1 Focused setup

First we use a focused setup, where the detector is placed in the focal plane of the imaging lens.

Regular dOTF reconstruction

All images are built using the selective stacking HDRI method discussed before. In Figure 4.6, we see a dOTF reconstruction using $\Delta t_0 = 1.0$ ms, $\xi = 2$, $n_t = 11$ and $n_I = 1$.

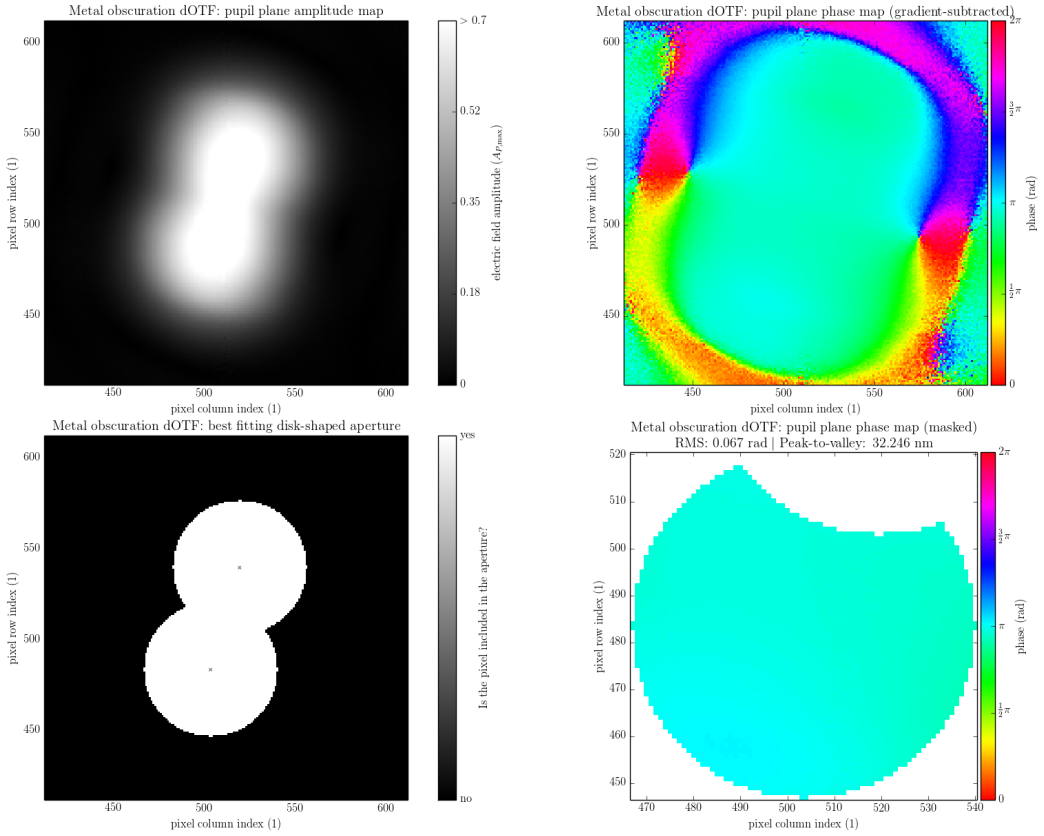

Figure 4.7: Metal obscuration dOTF using selective stacking HDRI parameters $\Delta t_0 = 1.0$ ms, $\xi = 2$, $n_t = 11$ and $n_I = 4$.

Relocated obscuration

To verify that the setup is really doing dOTF WFS, the obscuration was made to obscure the other edge of the aperture. In Figure 4.7, we see a dOTF reconstruction using $\Delta t_0 = 1.0$ ms, $\xi = 2$, $n_t = 11$ and $n_I = 4$. We indeed see that the dOTF PPAM is mirrored.

No obscuration

Another way to check that the setup is doing dOTF WFS, is by performing the dOTF reconstruction algorithm on two unobscured images. This is done in Figure 4.8. We see that the PPAM indeed does not resemble two merging disks in this case. The cropped aperture reflects this even more.

4.4.2 Defocused setup

Now we use a defocused setup. This has two reasons. First of all, by inducing defocus, the light intensity is smeared out over more detector pixels. This means that the dynamic range required to image a realization of the PSF is reduced and thus fewer exposure times n_t are required to probe the complete PSF using selective stacking HDRI. Another reason is that deliberately

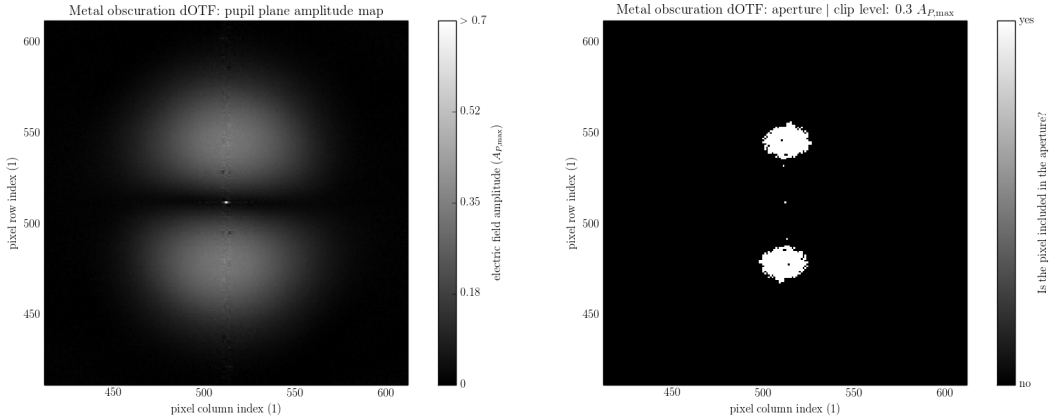

Figure 4.8: Metal obscuration dOTF using selective stacking HDRI parameters $\Delta t_0 = 1.0$ ms, $\xi = 2$, $n_t = 11$ and $n_I = 4$.

adding defocus can be used as a control mechanism to verify that dOTF WFS is working in practice.
One example has been shown in Figure 4.5. Another example, where we indeed lowered n_t, is shown in Figure 4.9. Convincing defocus is shown. Whilst $n_I = 8$ is used here, we might at the cost of a lower signal-to-noise ratio also use $n_I = 1$. In this case, the time necessary to make a single image is, according to Equation 4.2, at least 2,044.0 ms. This limits the frame rate of continuous metal obscuration dOTF WFS to $\frac{1}{2\Delta t} \approx 0.24$ fps, in the unrealistic case where we would be able to instantly place and remove the obscuration.

4.5 dOTF PPPM recovery: rotating polarizer

To do dOTF WFS for wavefronts that change rapidly in time, it is necessary to conceive a design in which the time between creation of an image with unobscured aperture and one with an obscured aperture is short. After all, dOTF WFS is based on the assumption that the image of the obscured aperture and the unobscured aperture are both made using the same ϕ_P. If the time between creation of the two images is too long, the incident wavefront has changed and the reconstruction becomes unreliable. Atmospheric wavefronts for instance, change on a timescale of 10 ms or so. [7]
It might be feasible to use a design with a rotating polarizer to take images in quick succession without removing the obscuration.

4.5.1 Rotating polarizer design

The obscuration consists in this case of a piece of polarizing material, and remains static in front of the aperture.
The incident light is either unpolarized, or linearly polarized in one of the two directions that make an angle of $\theta = \frac{\pi}{4}$ rad with the direction of polarization of the obscuration. For both unpolarized light and linearly polarized light with $\theta = \frac{\pi}{4}$ rad, we found in Section 2.7.2 that the intensity I after passing a polarizer is half the initial intensity I_0.
During operation of the dOTF WFS, a polarizer that is further along the optical path continuously changes it polarization direction from parallel to the obscuration to perpendicular to it,

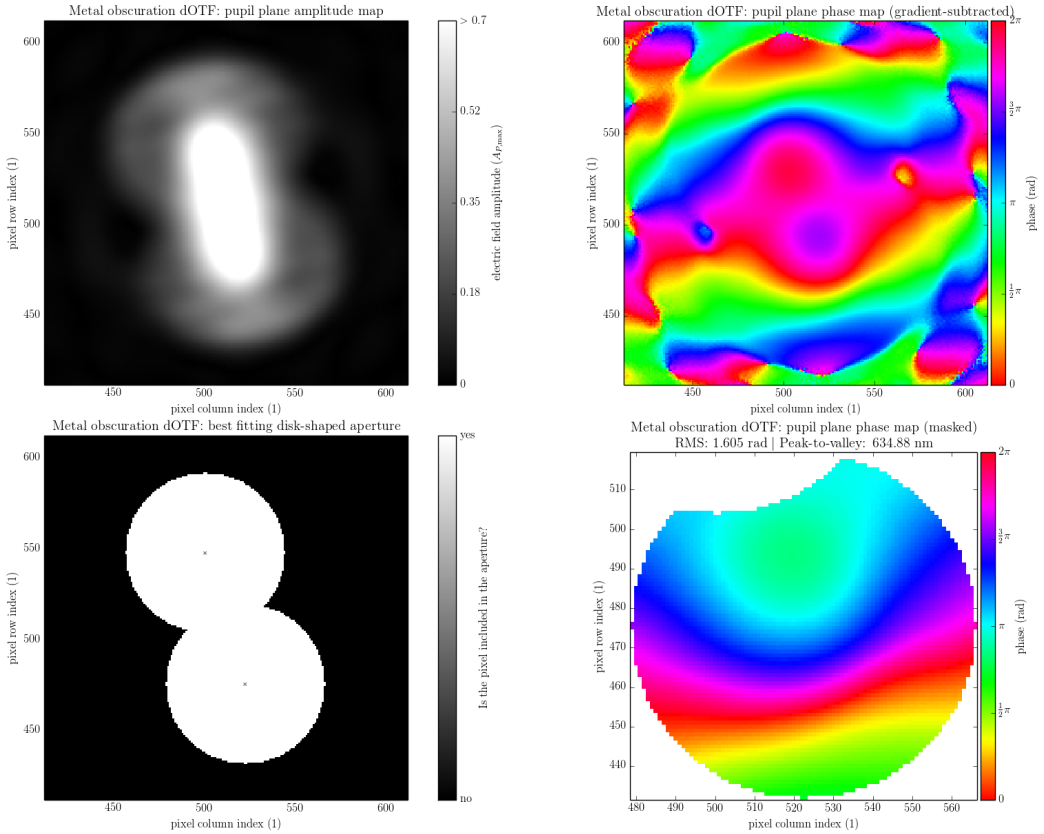

Figure 4.9: Metal obscuration defocused dOTF using selective stacking HDRI parameters $\Delta t_0 = 4.0$ ms, $\xi = 2$, $n_t = 9$ and $n_I = 8$.

and back to parallel again.

The parallel orientation

Let's first discuss the parallel orientation, as shown in Figure 4.10a. Assume the aperture is homogeneously lit with intensity I_0. Most light falls through the aperture unchanged - only the light that passes the polarizing finger sees its intensity going down to $\frac{1}{2}I_0$ and its polarization direction aligned with the finger. Now when the light arrives at the polarizer, *all* light that passed through the polarizing finger is transmitted, so that the final intensity in this region remains $\frac{1}{2}I_0$. The light that did not pass the finger was still unpolarized, so it loses half its intensity at the polarizer and ends up with $\frac{1}{2}I_0$. The final result is that *all* light is equally diminished in intensity, and the camera will 'see' the aperture as shown in Figure 4.10b.

The perpendicular orientation

Now assume the polarizer is rotated by $\frac{\pi}{2}$ rad, so that the configuration form Figure 4.10c is obtained. Again, the light incident at the polarizer has intensity $\frac{1}{2}I_0$ in the obscured region and intensity I_0 elsewhere. As the polarization direction of the light originating from the obscuration is perpendicular to the polarizer direction, nothing gets through, and the intensity goes to 0. The rest of the light waves, that were still unpolarized, pass the polarizer and have a final intensity of $\frac{1}{2}I_0$. The camera will 'see' the aperture as shown in Figure 4.10d.

4.5.2 High-speed dOTF wavefront sensing

The rotating polarizer design could be used to make a video with dOTF PPPM reconstructions. Instead of making 2 new images for each reconstruction, we could just create one new image per video frame. In this way, the frame rate can be boosted by a factor 2. The procedure is now illustrated.

1. To start with, we need to make an image with the circular aperture C_1 and an image with an obscured aperture O_1. C_1 and O_1 are then combined to generate video frame 1.

2. Then the polarizer rotates to parallel orientation and the second image with circular aperture C_2 is made. C_2 and O_1 are combined to generate video frame 2.

3. The polarizer rotates to perpendicular orientation and the second image with obscured aperture O_2 is made. C_2 and O_2 are combined to generate video frame 3.

4. Et caetera. The polarizer continuously switches between parallel and perpendicular orientation, and the two newest images are used to form a frame.

Due to the unavailability of programmable rotating polarizers, this setup was not realized.

4.6 dOTF PPPM recovery: polarizing beamsplitter

In the polarizing beamsplitter setup, the polarization property of light is exploited to create two images using a regular and obscured aperture simultaneously. This removes the need to rotate a polarizer, so that the setup does not contain any moving parts. Also, as now the two images can be built up simultaneously instead of sequentially, we save a factor of 2 in the time needed to create a single PSF image. Thus, polarization-induced dOTF WFS at a higher frame rate could be achieved in this way.

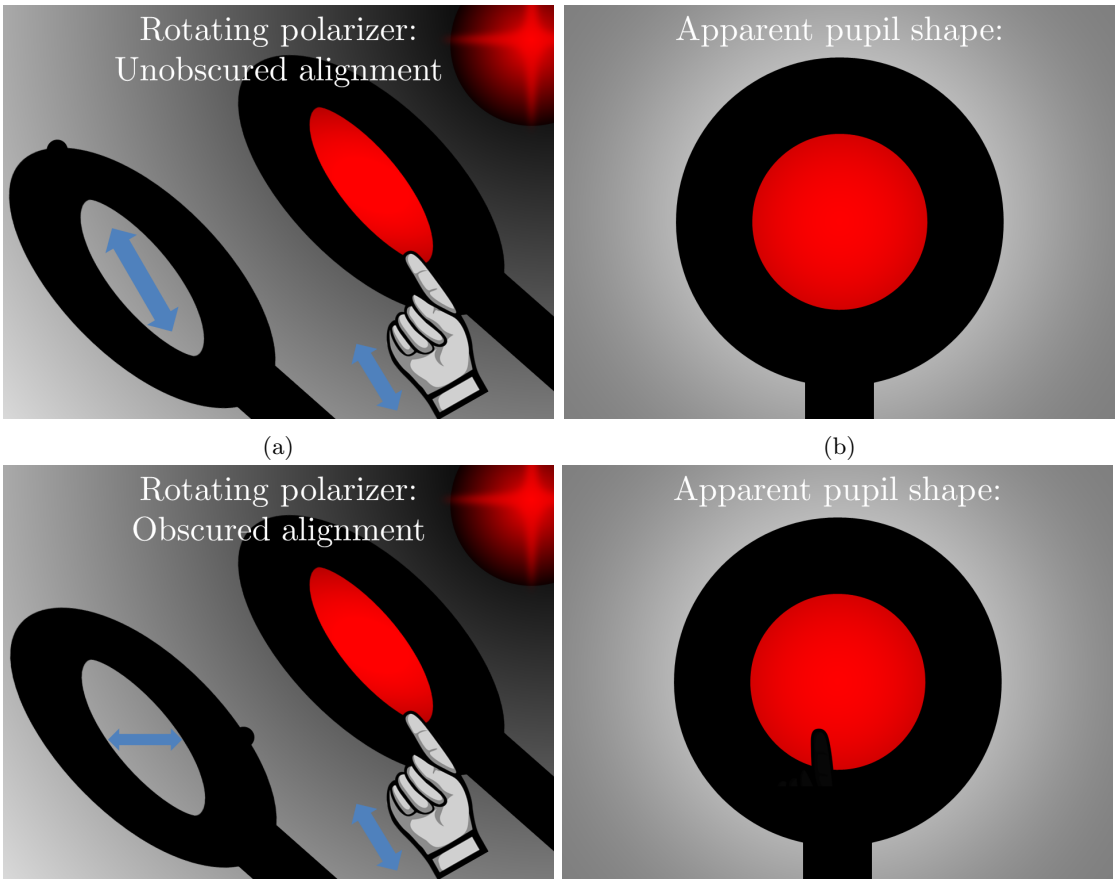

Figure 4.10: Principle of dOTF WFS using a rotating polarizer. Either unpolarized light or linearly polarized light making an angle of $\frac{\pi}{4}$ rad with the obscuration polarization direction is assumed. In the configuration of Figure 4.10a, the aperture effectively looks like Figure 4.10b. In the configuration of Figure 4.10c, the aperture effectively looks like Figure 4.10d.

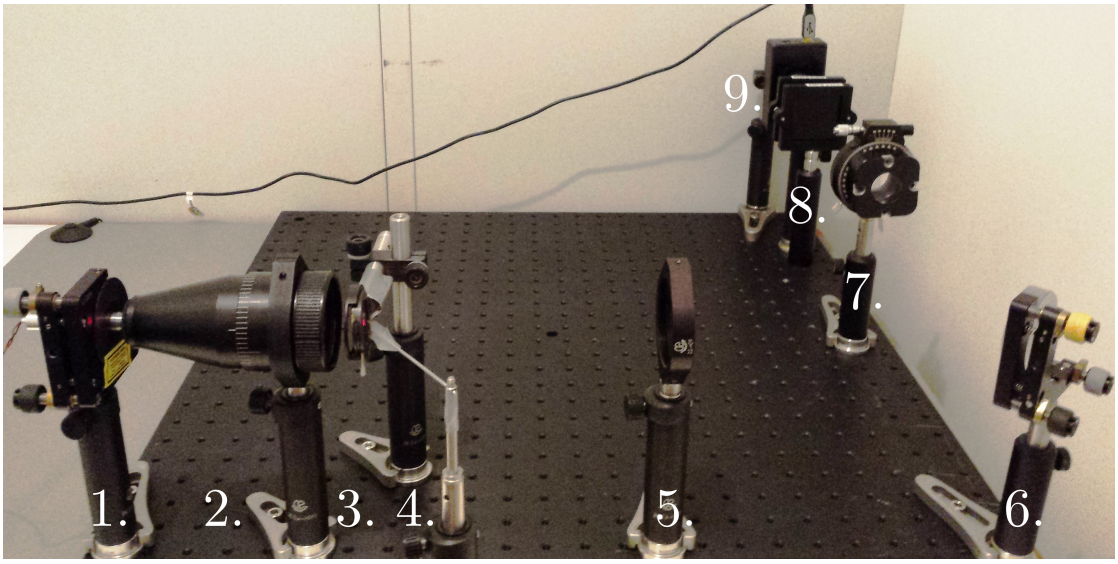

(a)

(b)

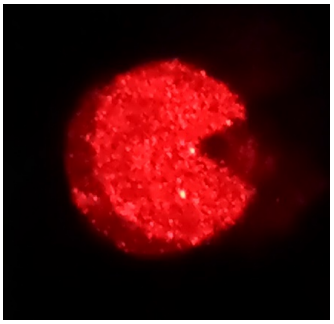

(c)

Figure 4.11: Setup for polarizing beamsplitter dOTF WFS. 1. laser; 2. beam expander; 3. aperture; 4. fixed polarized obscuration; 5. convex lens; 6. mirror; 7. polarizing beamsplitter; 8. ND filters; 9. CCD camera.

4.6.1 Setup

1. *The same laser* was used as the light source.
2. *The beam expander* is used again to homogenize the beam that is incident in the pupil plane.
3. *The bladed aperture* is utilized again.
4. In this setup, *the obscuration* has a fixed position in the pupil plane and does not need to be moved. A piece of polarizing material is used. A close-up is shown in Figure 4.11b. With the obscuration in place, the pupil looks like Figure 4.11c.
5. The beam reaches *a convex lens* that converges the light. This lens has a focal length of 750.0 mm.

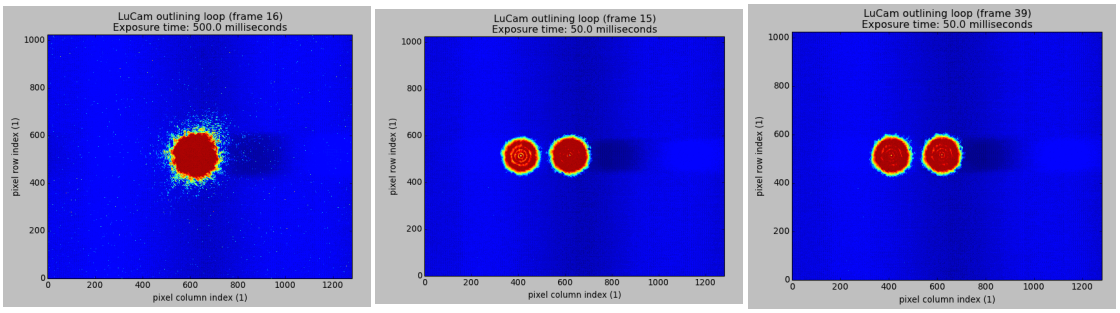

(a) (b) (c)

Figure 4.12: Overview of three stages in the polarizing beamsplitter outlining procedure.

6. *A mirror* changes the direction of the beam by 90°.
7. *A polarizing beamsplitter* is used that splits the beam in two sub-beams with orthogonal polarization directions. One beam represents the regular aperture, while the other represents the obscured aperture.
8. *Two neutral density filters* (ND filters) were utilized to attenuate the laser radiation, one with OD = 1 and one with OD = 2.
9. *The same CCD camera* was placed in the focal plane of the lens.

The setup is shown in Figure 4.11a.

Polarizing beamsplitter properties

The polarizing beamsplitter in the setup is a Wollaston Prism from the company Thor Labs. The beam separation effected is 0.5°.

4.6.2 Outlining the setup

A correctly aligned setup would be most easily achieved using unpolarized light. This would only require one of the polarization directions of the polarizing beamsplitter to coincide with the polarization direction of the obscuration. Unfortunately, the laser used in the setup produces linearly polarized light. We can overcome this problem by choosing a specific orientation for the orthogonal polarization directions of the beamsplitter relative to laser polarization direction. Both beamsplitter polarization directions should make an angle of $\frac{\pi}{4}$ rad with the laser polarization direction. In this way, equal attenuation is achieved in both beams for the light not passing through the obscuration. The obscuration polarization direction should correspond to one of the beamsplitter directions.

The best way to outline the setup is given below.

1. Place the obscuration in such a way that it covers the complete aperture. In this way, the attenuation of light is the same for every position in the aperture.
2. Now rotate the polarizing beamsplitter until one of the two realizations of the PSF vanishes. When this happens, we know that one of the polarization directions of the beamsplitter

is equal to the obscuration polarization direction, while the other is perpendicular to it. This can be done using the video outlining routine. For the best alignment, use a long integration time so that if there is still a weak image, its traces become visible. After proper alignment, the focal plane should look like Figure 4.12a.

3. Now remove the obscuration entirely. Most likely, the two images will now not be of equal intensity, and the outlining feedback looks something along the lines of Figure 4.12b.
4. Rotate the laser diode until both PSF realizations are equally bright, and the outlining video looks like Figure 4.12c.
5. Now the obscuration can be used to partially block the aperture.

4.6.3 Reconstruction algorithm

Polarizing beamsplitter dOTF reconstructions are made in the following way.

1. To image the two PSFs, selective stacking HDRI was employed again.
2. The resulting frame is cut in two in a way that both pieces contain a PSF image.
3. The image centers are determined by picking the brightest pixel of each piece. Two aligned, square cutouts are made.
4. The image centers are stored in lists, and the image centers for all reconstructions after the first are found by taking the mean value of these lists. In this way, even when a noise source would make the image center shift a few pixels in a certain reconstruction, the eventual mean image centers converge to the real positions of the realizations of the PSFs on the CCD.
5. Sub-pixel shifts are performed to perfectly align the PSFs. A demonstration of the variability of the dOTF PPAM for shifts smaller than one pixel in both column and row directions is shown in Figure 4.13b. To find the best sub-pixel shift, the following procedure is used.
   (a) First, a range of sub-pixel shifts in the column and row direction is defined.
   (b) For each shift, the dOTF PPPM is calculated. An overview as in Figure 4.13b is acquired.
   (c) Inspection of this figure shows that misaligned PSF realizations give rise to a discontinuity in the dOTF PPPM around the map center. To detect this discontinuity, we compute an error measure that is equal to the sum of the standard deviations of a small set of column pixels and a small set of row pixels at the map center.
   (d) The sub-pixel shift that gives rise to the lowest error measure is selected as best shift.
   (e) Around the detected best shift, possibly another iteration of this process is performed, as the image alignment needs to be accurate to within hundreths of pixels.
6. The two cropped images are used for dOTF PPAM and PPPM reconstruction in the usual way.

4.6.4 Results

For a well-aligned setup, obscuring the whole aperture with the polarized material will make one PSF image vanish, and removing the obscuration completely results in two equally bright images. First these conditions were guaranteed. Then, the reconstructions from Figure 4.14 were made.

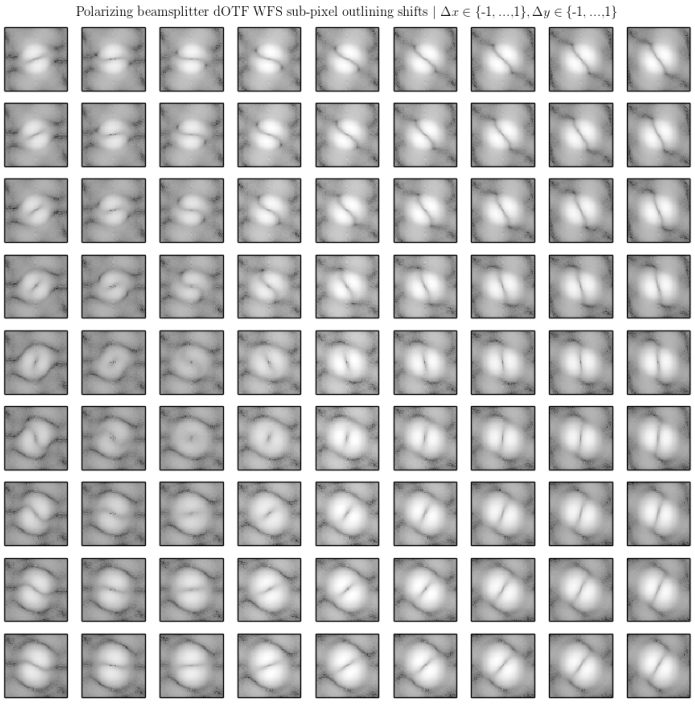

(a) dOTF PPAMs using lab data.

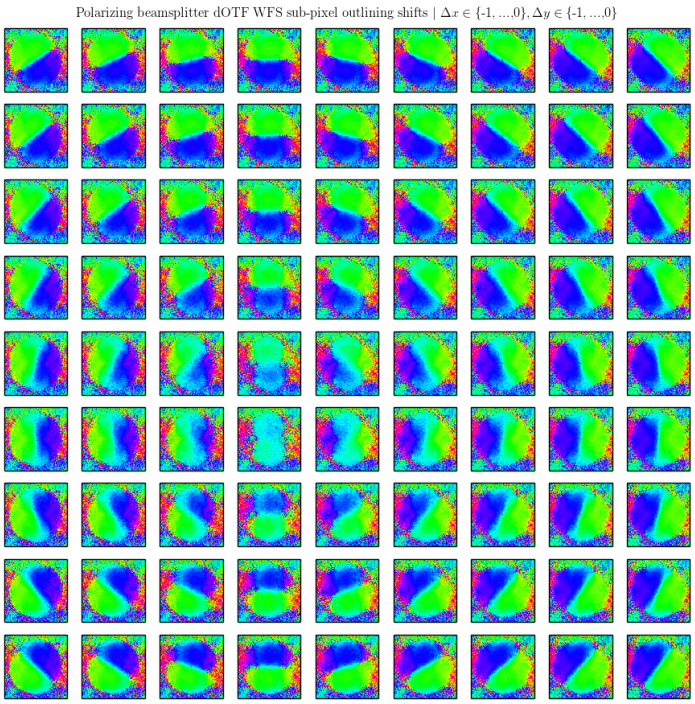

(b) dOTF PPPMs using simulation data.

Figure 4.13: Demonstration of the sensitivity of the dOTF reconstruction to small shifts in the relative orientation of the two PSF realizations.

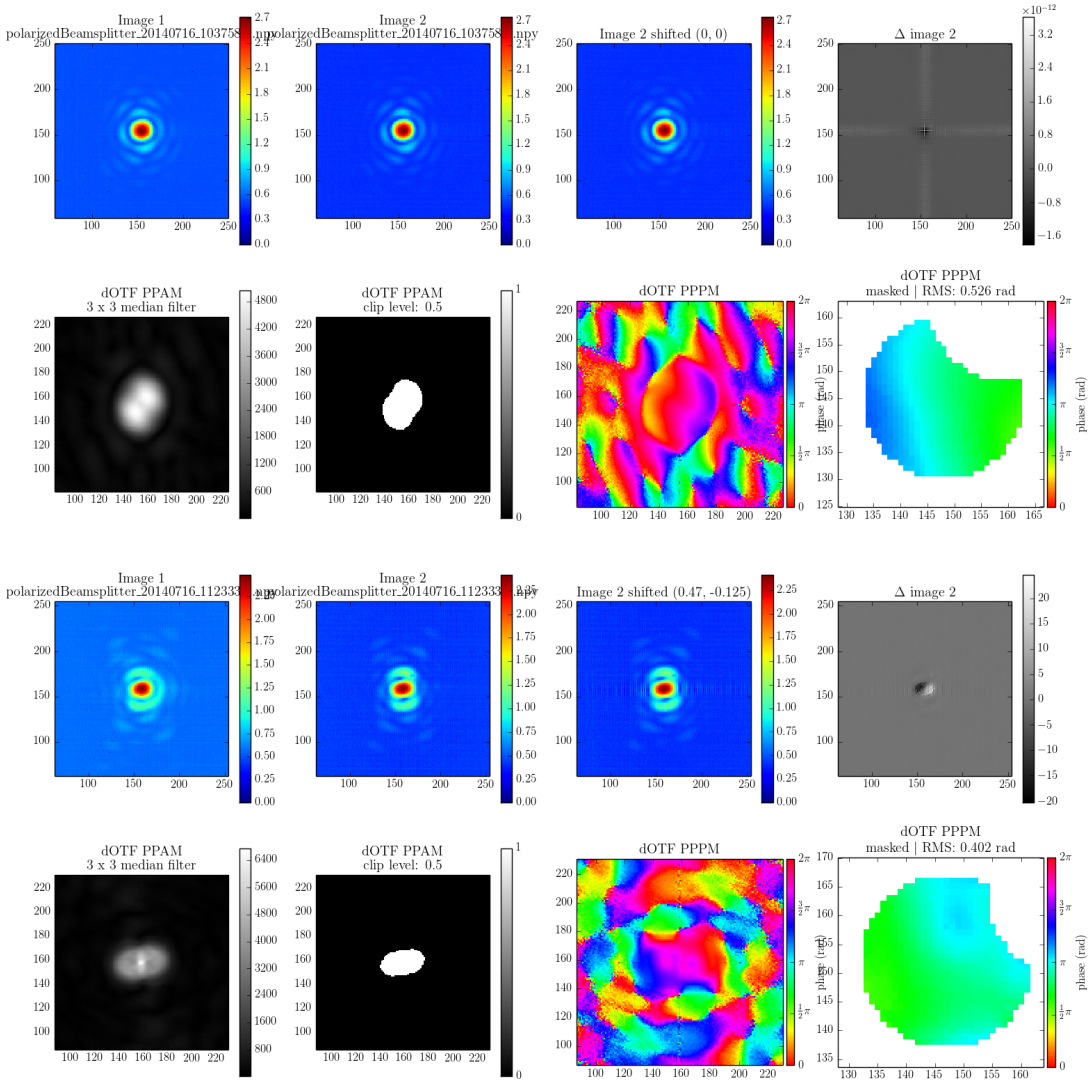

Figure 4.14: Polarizing beamsplitter dOTF WFS using selective stacking HDRI. The used integration times were $\{1, 1, 3, 8, 16, 32, 64, 128, 256, 512, 1024, 1024\}$ ms. Both reconstructions were made using the triangular obscuration.

Chapter 5

Future prospects

In this chapter, I briefly summarize possibilities for future research on polarization-induced dOTF WFS.

5.1 Simulations

- **Adaptive dOTF WFS:** It would be great to test the adaptive dOTF WFS algorithm described in Section 3.7.4 to see whether it would increase the mean reconstructive quality of the measurements. If the method would not work, we obtain more evidence that sticking with a fixed obscuration, at least for constant $\frac{D}{r_0}$, is the way to go for real dOTF wavefront sensors.
- **Wavelength bands:** The current simulations have been limited to monochromatic light. In reality, all dOTF wavefront sensors will have to cope with radiation from a spectral band that contains a continuum of wavelengths. For practical purposes, it would therefore be necessary to simulate the effect of multiple wavelengths on the reconstruction quality.
- **Regular polygon aperture shapes:** Currently, the simulations work with circular apertures only. In my setup though, a bladed aperture is utilized. To allow for better comparison between simulations and experiment, it would be useful to add the option to create these bladed apertures. Ideally, the procedure to do this is generalized, so that any regular polygon can be taken as an aperture.
- **More obscuration shapes:** An immediate question that comes to mind for many people when they hear about dOTF WFS, is how the reconstruction quality is affected when other types of obscurations are used. How would triangular, rectangular or line-shaped obscurations perform compared to a disk-shaped obscuration?
- **Simulating measurements:** The last and most involving suggestion for future work would be to simulate real measurements, using Kolmogorov phase maps that change in time. There is a balance between integrating long enough so that every pixel's signal-to-noise ratio is increased, resulting in a higher quality reconstructions, and integrating short enough so that the Kolmogorov atmosphere does not change too much. The best integration time and obscuration size could be found for a given star flux. This information is valuable in real situations - if a dOTF WFS is commanded to observe a certain star, it could determine the star's brightness from known star catalogi to find the best integration time and obscuration radius.

Figure 5.1: Night view of the South African Large Telescope, one of the world's largest optical telescopes. A polarization-induced dOTF WFS prototype might be tested here.

5.2 Lab experiments

- **Rotating polarizer experiments:** It is unfortunate that the rotating polarizer setup has not been tested. This should happen in the near future and would decisively show whether a polarization-induced dOTF WFS can work.
- **Polarizing beamsplitter experiments:** The polarizing beamsplitter setup generates a PPPM reconstruction video with a frame rate of about 0.2 fps. It is clear that for implementation in an AO system, the frame rate has to be increased by three to four orders of magnitude. To guarantee trustworthy PPPM reconstructions, the PSF realization alignment algorithm has to be refined. Moreover, an absolute proof of polarizing beamsplitter dOTF WFS could be done by demonstrating that the reconstructions made using a metal obscuration and a polarizing obscuration are the same. This should be the case for reconstructions using long integration times, where the wavefront distortions are due to the optical elements in the setup alone.

5.3 Field experiments

An exciting outlook for dOTF wavefront sensing is Professor Kenworthy's current agreement to install a prototype of a polarization-induced dOTF wavefront sensor at the Southern African Large Telescope (SALT) at the South African Astronomical Observatory (SAAO). This observatory lies on a hilltop in a nature reserve, near the small town of Sutherland in North Cape province, South Africa. The SALT is the largest optical telescope in a single structure on the Southern Hemisphere. [4] The telescope is special in its design in the sense that it observes the sky at a fixed altitude. Azimuthal rotations are possible. The specifications of this polarization-

induced dOTF WFS prototype will be based on my simulations and laboratory work! It would be great to stay involved in this exciting development.

Chapter 6

Summary and conclusion

In this research, a new, simple and image-based wavefront sensing technique called *differential optical transfer function wavefront sensing* (dOTF WFS) has been studied.
The technique reconstructs a wavefront by recording two images of the same source with two different apertures. In this research, one aperture was assumed to be circular; the other deviated from this shape by the exclusion of a disk-like region centered on the edge of the regular aperture that we dubbed *the obscuration*.
We simulated and built a polarizing beamsplitter dOTF WFS design that contains no moving parts and creates the two images required for a wavefront reconstruction simultaneously.

6.1 Main simulation results

The size of the obscuration determines the quality of the wavefront reconstruction. When bigger obscurations were used, the reconstructions were less noise-sensitive, but lacked the detail of reconstructions made with smaller obscuration radii. It was found that the obscuration size that allows for the best wavefront measurement depends on both the wavefront and the source intensity.

For a polarizing beamsplitter design with a pupil diameter of 30 cm observing at a wavelength of 500 nm with a 5% bandpass filter, a photon efficiency of 50% and a WFS frame rate of 1,000 fps, the best static obscuration radius was found to be 30% of the aperture radius for Fried parameter values between 2 and 15 cm. These results were found assuming Vega, one of the brightest stars in the sky, as target star. It was established that to maintain at least 25% wavefront flattening, only target stars brighter than magnitude 4 stars should be used. Next, for various levels of turbulence, numerical results were found for the obscuration radii that maximize dOTF WFS performance if the obscuration could change in size.

Finally, it was inquired whether continuous adaptation of the obscuration size - even for a fixed statistical description of atmospheric turbulence - could be effective. The gains were found to be roughly 15%.

6.2 Main laboratory results

Using a metal obscuration, dOTF wavefront sensing was performed in the lab and verified by means of several controls. A rotating polarizer setup has been described that removes the need of manual addition and removal of an obscuration. Furthermore, an extensive code infrastructure was built that allows for various measurements, checks and visualizations involving dOTF WFS, that can be used to perform wavefront measurements measurements in this setup whenever the required parts come available.

Finally, a polarizing beamsplitter setup has been built that contains no moving parts and allows for the simultaneous creation of the two images required for wavefront reconstruction. Results suggest that this design is viable for dOTF wavefront sensing.

6.3 Conclusions

dOTF wavefront sensing is a promising technique for correcting both static and time-dependent aberrations. It has been demonstrated to work in the lab. For atmospheric observations, it would be necessary to adapt the obscuration size whenever the Fried parameter changes, as the best obscurations for low turbulence levels perform badly when confronted with highly turbulent skies. For a constant Fried parameter, adapting the obscuration offers only modest gains at best and should not be a priority.
A polarization-induced dOTF WFS design might be suitable for astronomical wavefront sensing. Using an adaptable obscuration via liquid crystals, the instrument could continuously optimize its performance for the level of atmospheric turbulence at its observing location and the brightness of its target star. Also, the fact that a polarizing beamsplitter design would not require any moving mechanical parts makes it practical for outdoor applications. Lab experiments using this setup have shown that the technique is feasible, although practical implementation in AO systems is still far away.

Chapter 7

Acknowledgements

7.1 People

First of all, I would like to thank Professor **Matthew Kenworthy**, my main supervisor (representing Astronomy), for introducing me to dOTF wavefront sensing and his numerous contributions to my project on the subject. Not only did I learn a lot from our progress meetings, I feel I've also taken over some of your boundless enthusiasm for optics and astronomical instrumentation. I enjoyed doing the project a lot - both the comfort of programming simulations at home as the practical work in the lab. Along the way, I also greatly expanded my skills in `Python` and LaTeX. Many thanks for putting trust in me to do this new and exciting research!

I would like to thank **Gilles Otten** for his benevolence of freeing time to answer my questions and to get me up to speed in the lab. Gilles, it is great that you are always helpful and willing to think along. There were several points in the project where your suggestions were of great importance. I was especially amazed by your effort in hunting down a bug in my dOTF reconstructions - after I left your office, you programmed the necessary code yourself and sent me an e-mail detailing the solution to the problem that same night.

A great deal of the results of the simulations rely on the work of **Emiel Por**. Emiel, thank you for the opportunity to use your code for the creation of Kolmogorov phase maps, and the time you've taken to explain your code to me.

Professor **Martin van Exter** has been my secondary supervisor (representing Physics). I would like to express my gratitude for your critical eye on the project during our meetings and your involvement in grading my research project.

My good friend **Jacob Bakermans** can not remain unmentioned here. Jacob, you have helped me with the project in numerous ways, and offered me advice when I needed it. Your ability to identify the essential elements of a problem and to find appropriate solutions, always impresses me. It was also great to be able to use your laptop for the lab work. Lastly, I was honored by your inclination to attend my final presentation a week before the actual date.

I would also like to say thank you to **Niek Doelman**, **Tiffany Meshkat** and **Stijn Debackere** for their suggestions.

7.2 Software

- Much of this research has been powered by `Python`, a powerful programming language of increasing popularity, with a clean syntax and very high speed of development. This makes it ideal for most scientific projects where computational efficiency is not the key priority. For more information on `Python`, see `python.org`.
- For this research, I used the convenient code editor `TextWrangler`. It supports `Python` color coding and offers terminal code execution in a two mouse clicks.
  See `barebones.com/products/textwrangler`.
- My thesis and lab notebook would never have looked so great and well-structured as they do now without LaTeX, a typesetting system much used in the production of scientific documents. See `latex-project.org` for more.
- I used `TeXShop` as a LaTeX editor and compiler for Mac OS X. I like that it is so easy-to-use. For more information, check `pages.uoregon.edu/koch/texshop`.

Appendix A

Simulations of instrumental aberrations

I have modelled two simple instrumental aberrations: tip-tilt and defocus. For instrumental aberrations in optical setups, the amount of photons hitting the detector per exposure time E_γ depends on the intensity of the light source used, which can vary wildy.

Tip-tilt

Tip-tilt in optical setups occur when a flat wavefront is not parallel with a predefined pupil plane, in the sense that the wavefront's wave vector $\vec{k}$ would make a non-zero angle with the normal of the reference plane. It we would be able to detect tip-tilt, this could be used in practice to align beams that should be perpendicular to certain planes.
As a $\phi_P(x, y)$ containing only the tip-tilt aberration amounts to a smooth phase gradient, we do not expect that small obscuration radii are desired - there are no fine details to probe in the PPPM, while noise effects play a bigger role than for larger obscuration radii.
In Figures A.1a and A.1b, we see the best fixed obscuration radii for two wildly varying levels of tip-tilt under different illumination levels. It is apparent that if one was to make a dOTF WFS specifically for measuring tip-tilt, the obscuration should be made large.[1]

Defocus

Another common aberration in optical setups is defocus. There are two ways a defocused image can be obtained:

- A wavefront with the shape of a paraboloid is incident at the pupil plane of an optical system in focus. An imaging device is placed at the focal plane of the focussing convex lens.
- A flat wavefront is incident at the pupil plane of an optical system out of focus. An imaging device is placed before or behind the focal plane of the focussing convex lens.

The way defocus is obtained in these simulations is by using a paraboloidal ϕ_P as described by Equation 3.5.

[1] Although larger obscuration radii go along with lower RMS values in this case (which is good), they also have the consequence of increasing the overlap region (which is bad).

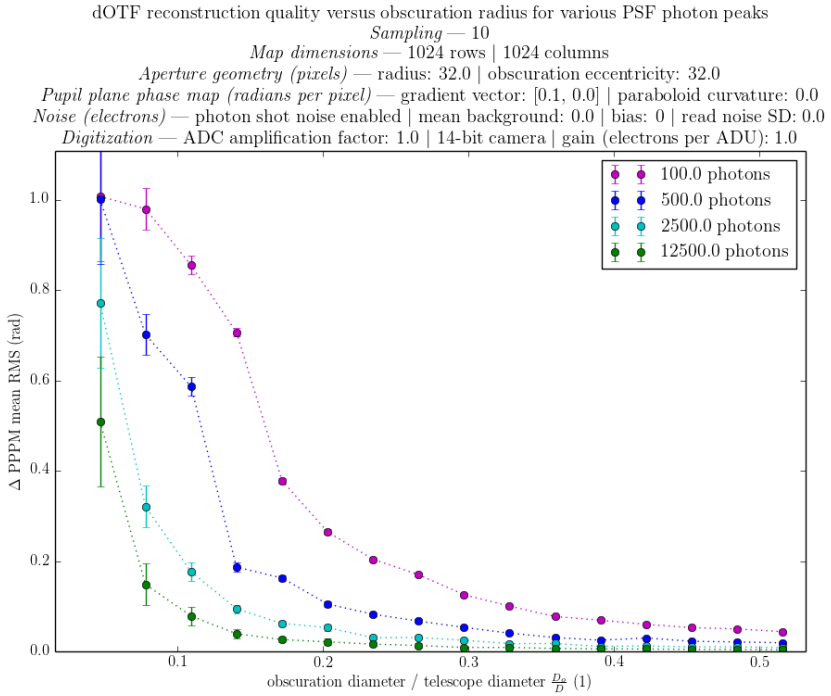

(a) Weak tip-tilt aberration: $||\vec{\nabla}\phi_P|| = 0.1\,\frac{\text{rad}}{\text{pixel}}$.

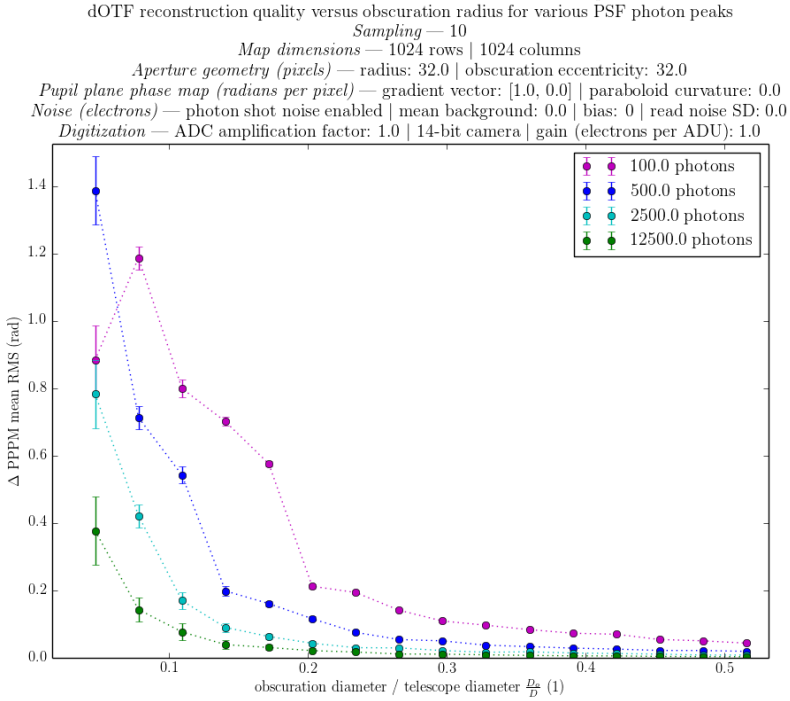

(b) Strong tip-tilt aberration: $||\vec{\nabla}\phi_P|| = 1\,\frac{\text{rad}}{\text{pixel}}$.

Figure A.1: Dependence of the performance of various obscuration sizes on the light intensity incident at the pupil plane for a weak and a strong tip-tilt aberration.

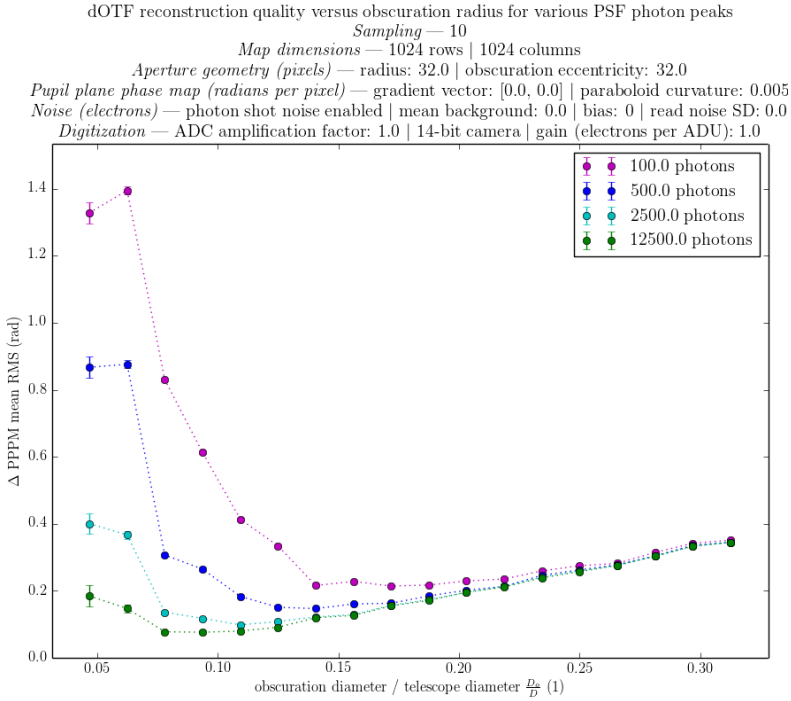

(a) Weak defocus aberration: $\xi = 0.005\ \frac{\text{rad}}{\text{pixel}^2}$.

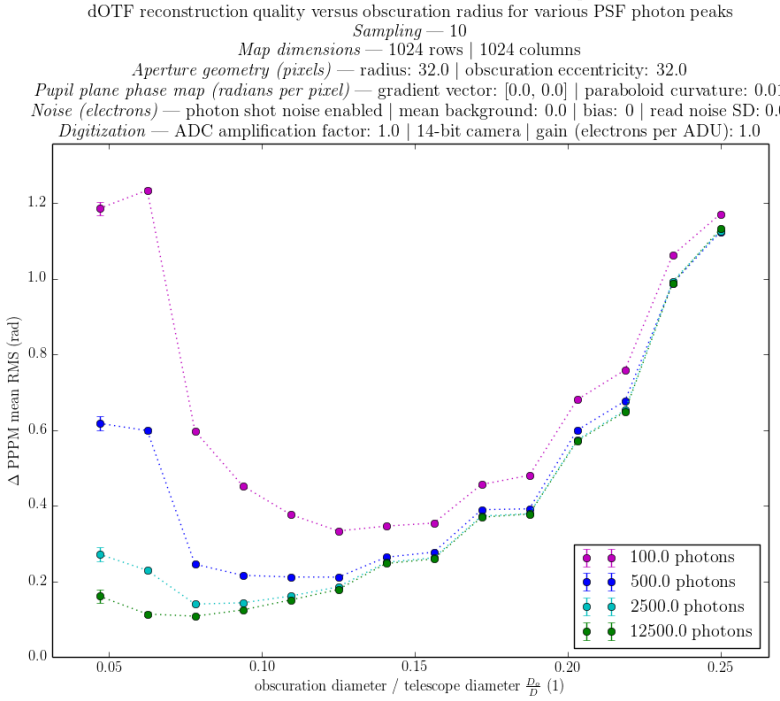

(b) Strong defocus aberration: $\xi = 0.01\ \frac{\text{rad}}{\text{pixel}^2}$.

Figure A.2: Dependence of the performance of various obscuration sizes on the light intensity incident at the pupil plane for a weak and a strong defocus aberration.

Figures A.2a and A.2b show the PPPM reconstruction performance of dOTF wavefront sensors using various obscuration radii under different illumination levels for two different paraboloid curvatures ξ. The results can be summarized as follows.

For a defocus of $\xi = 0.005\ \frac{\text{rad}}{\text{pixel}^2}$:

$\text{PSF}_\gamma(x_{\max}, y_{\max})$ (photons)	Best $\frac{D_O}{D} = \frac{r_O}{r_P}$ (%)	Best $\langle \text{RMS} \rangle$ (rad)
100	17	0.214
500	14	0.147
2,500	11	0.098
12,500	9.4	0.076

For a defocus of $\xi = 0.01\ \frac{\text{rad}}{\text{pixel}^2}$:

$\text{PSF}_\gamma(x_{\max}, y_{\max})$ (photons)	Best $\frac{D_O}{D} = \frac{r_O}{r_P}$ (%)	Best $\langle \text{RMS} \rangle$ (rad)
100	13	0.333
500	13	0.211
2,500	7.8	0.140
12,500	7.8	0.108

For a defocus of $\xi = 0.02\ \frac{\text{rad}}{\text{pixel}^2}$:

$\text{PSF}_\gamma(x_{\max}, y_{\max})$ (photons)	Best $\frac{D_O}{D} = \frac{r_O}{r_P}$ (%)	Best $\langle \text{RMS} \rangle$ (rad)
100	7.8	0.448
500	6.3	0.246
2,500	6.3	0.141
12,500	6.3	0.110

For this aberration type, in contrast to tip-tilt, there is a clear sweet spot for the best fixed obscuration radius, depending on both the amount of defocus and the PSF peak. Optimized measurements of defocus PPPMs require smaller obscuration radii as ξ increases; higher pupil plane intensity (or, as an alternative option for static aberrations in an optical setup like defocus, longer integration times) favors smaller obscuration radii as well.

Appendix B

Code library

For both the simulations and the laboratory experiments, an extensive library of `Python` code was written. The routines in this library may very well be suitable for follow-up research. Therefore, for each program, a short description is given. The code is available by contacting the author. The programs are ordered in the way their contents are discussed in this thesis.

B.1 Simulations

- `imageSimulation.py` enables the user to interactively create and visualize a PSF or digital image using the simulation parameters discussed. An obscuration can be added to the aperture, a specific gradient and defocus pupil plane phase map can be created (though Kolmogorov phase maps are not yet implemented) and all mentioned noise sources can be added. The final data can be stored in `.bin`-files, that are accompanied by text files detailing all parameters used in creating the data.
- `dOTFSimulation.py` takes in two PSFs or digital images created using `imageSimulation.py` and performs dOTF PPPM reconstruction on it. The program offers visual comparison with the input PPPM and also visualizes the difference map between actual and reconstructed PPPM.
- `dOTFQuality.py` contains routines to assess the quality of dOTF wavefront sensing. All routines extensively visualize their results. The simplest routine looks for the best obscuration radius for a given phase map (either Kolmogorov or gradient and defocus) and parameter set. Another routine does the same, but now for various levels of the unobscured PSF peak value. A third function is solely designed for simulating atmospheric dOTF WFS and thus uses Kolmogorov wavefronts only. For each wavefront, a single reconstruction is made for n_O different obscurations, and the data is stored in a text file. Coupled to this function is a feature that loads in a sequence of n_W associated text files, and performs data analysis on it. It finds the best fixed obscuration radius, inquires the maximum merit of adaptive dOTF WFS and the relation between reconstruction quality and reconstruction RMS. The file also contains two routines that were not mentioned in this thesis. One routine implements best fixed obscuration radius determination for atmospheric dOTF WFS in another way, by selecting the best fixed obscuration radius per Kolmogorov phase map, so that it builds a histogram of n_W best fixed obscuration radii. Another routine simulates a time series of atmospheric dOTF WFS observations, where the Kolmogorov phase maps evolve from one into another by means of wind and turbulence.

- `dOTFFunctions.py` lists a series of functions that can be used in other files. One function allows the user to obtain a digital image for a given PPPM and parameter list in a single line. Other functions calculate the RMS of a phase map, do a dOTF phase map reconstruction, analyse the quality of a reconstruction with an elaborate self-updating overview, and find the center of a bright spot on an image.
- `kolmogorovPhaseMapCreation.py` lists a series of related functions that together provide the functionality of creating Kolmogorov phase maps. It is used in other files.
- `kolmogorovPhaseMapTesting.py` contains visualizations and verifications of the functions written in `kolmogorovPhaseMapCreation.py`. For either uncorrelated phase maps, or maps related to each other by wind and turbulence, it can plot an overview of how such maps and their corresponding PSFs look. Moreover, it is possible to save the PSF images as a video, so that the time evolution of the PSF as it is without adaptive optics can be shown.
- `plotApertureDesigns.py` visualizes the best aperture designs for various levels of $\frac{D}{r_0}$ by means of both a plot and a graphical overview.
- `plotAdaptiveWFS.py` outputs a bar plot and a list of the possible gains of adaptive dOTF WFS.

B.2 Laboratory experiments

- `LuCam.py` is a program by Christoph Gohlke that enables the user to control the Lumenera camera using Python commands.
- `LuCamOutline.py` is a program that continuously creates images and shows them on screen in a video fashion, and is used for outlining a setup.
- `LuCamControl.py` enables the user to shoot images using the LuCam and store them in FITS-files. 4 modes can be chosen: single image recording, bias frame recording, flat frame recording and recording of a set of frames suitable for selective stacking HDRI.
- `masterBiasCreation.py` creates a master bias from a set of FITS-files and visualizes the result.
- `masterFlatCreation.py` creates a master flat from a set of FITS-files and visualizes the result.
- `imageDifference.py` loads in two FITS-files for comparison. Statistical information about both images are given, and a visualization and histogram of the difference map are made.
- `dataReduction.py` loads a FITS-file and performs data reduction on it. At each step of the data reduction process, a visualization is made. The steps are, in this order, bias subtraction, flat division, PSF center determination, disk-shaped masking of the PSF for background subtraction, and cropping of the final image. The result can be stored again as a FITS-file.
- `dataReductionStack.py` loads in a stack of FITS-files and performs bias subtraction and flat division using a given master bias and master flat. The images are stored again in FITS-files.

- `HDRIMean.py` stacks a set of reduced images made with `dataReductionStack.py` together to obtain a mean image with lower noise levels. The result can be visualized and saved.
- `HDRISelectiveStacking.py` loads in a set of raw images taken with `LuCamControl.py` and performs selective stacking HDRI.
- `dOTFData.py` asks the user to input the names of two images to perform dOTF PPPM reconstruction, which could for example be made using `HDRISelectiveStacking.py` or `HDRIMean.py`. It contains extensive visualization options for the dOTF PPAM, pupil plane intensity map and PPPM. A gradient in the dOTF PPPM can be removed. The center of the aperture is determined and the dOTF PPPM is given a disk-shaped mask.
- `LuCamPolarizedBeamsplitter.py` is a culmination of the routines in many of the previous files. Using the `LuCam.py` module, it enables continuous dOTF PPPM reconstruction in a video-like fashion using the Lumenera camera. It records a set of frames and performs data reduction on them, combines them into a normalized continuous PSF realization using selective stacking HDRI. The image is split in two, so that two images containing one point source each is obtained. They are aligned, and dOTF PPPM reconstruction is performed. The reduction steps of `dOTFData.py` were followed and an auto-updating overview of the complete wavefront reconstruction process is shown on screen. The PSF realizations are saved.
- `dOTFPolarizedBeamsplitter.py` takes two saved images of `LuCamPolarizedBeamsplitter.py` and performs an alignment algorithm to adequately position the images on top of each other. Visualisations can be made of the process.

Appendix C

List of abbreviations

Here follows an overview of all abbreviations used in this thesis for easy reference. The order is alphabetical.

ADC	analog-to-digital converter
ADU	analog-to-digital unit
AO	adaptive optics
bpp	bits per pixel
CCD	charge-coupled device
CMOS	complementary metal-oxide-semiconductor
DFT	discrete Fourier transform
dOTF	differential OTF
E-ELT	European Extremely Large Telescope
FFT	fast Fourier transform
FITS	Flexible Image Transport System
fps	frames per second
HDRI	high-dynamic-range imaging
ND	neutral density
OD	optical density
OTF	optical transfer function
PDF	probability density function
PMF	probability mass function
PPAM	pupil plane amplitude map
PPPM	pupil plane phase map
PSF	point spread function
RMS	root mean square

SAAO	South African Astronomical Observatory
SALT	Southern African Large Telescope
WFS	wavefront sensing *or* wavefront sensor

Appendix D

List of mathematical symbols

Here follows an overview of the most important mathematical symbols used in this thesis for easy reference. The order is thematic.

(M, N)	number of rows and columns of a map
(x_C, y_C)	central coordinates of the map
(x_P, y_P)	central coordinates of the pupil
(x_O, y_O)	central coordinates of the obscuration
r_P	pupil radius
D	pupil diameter; equals $2r_P$
S_P	regular pupil surface area; equals πr_P^2
r_O	obscuration radius
D_O	obscuration diameter; equals $2r_O$
$A_P(x, y)$	regular pupil plane amplitude map
$A'_P(x, y)$	obscured pupil plane amplitude map
$A_{\mathrm{dOTF}}(x, y)$	reconstructed pupil plane amplitude map
$\vec{\nabla}\phi_P$	phase gradient vector
$\phi_P(x, y)$	actual pupil plane phase map
$\phi_{\mathrm{dOTF}}(x, y)$	reconstructed pupil plane phase map
$\phi_\Delta(x, y)$	difference between ϕ_P and ϕ_{dOTF}
$\mathscr{F}$	Fourier transformation operator
$\Psi_P(x, y)$	pupil plane complex amplitudes
$\Psi_F(x, y)$	focal plane complex amplitudes
E_γ	expected total number of photons per regular aperture image
$N_\gamma(x, y)$	photon map
$N_e(x, y)$	electron map

$N_D(x, y)$	digital image
r_0	Fried parameter
$\vec{k}$	wave vector
$n(\vec{r}, t)$	refractive index
n_O	number of simulated obscuration radii
n_W	number of simulated Kolmogorov pupil plane phase maps
m_V	visual apparent magnitude
λ	central observing wavelength
$\Delta\lambda$	filter bandwidth
Δt	total integration time per image
η	dOTF WFS photon efficiency
f	focal length of the imaging lens
n_B	sigma clipping number of bias frames
n_σ	sigma clipping exclusion level
$\mathscr{I}(x, y, z)$	sigma clipping image cube
$B(x, y)$	master bias
$F(x, y)$	master flat
Δt_0	selective stacking HDRI lowest integration time
ξ	selective stacking HDRI integration time increment factor
n_I	selective stacking HDRI number of images per integration time
n_t	selective stacking HDRI number of integration times

Bibliography

[1] A. N. Kolmogorov, *The local structure of turbulence in incompressible viscous fluid for very large Reynolds numbers*, Dokl. Akad. Nauk SSSR, vol. 30, 299303, reprinted in 1991 (1941)

[2] D. L. Fried, *Statistics of a geometric representation of wavefront distortion*, JOSA 55, 11 14271431 (1965)

[3] J. L. Codona and M. Kenworthy, *Focal plane wavefront sensing using residual adaptive optics speckles*, The Astrophysical Journal, 767:100 (26pp) (2013)

[4] *Introduction*. Retrieved July 5 2014, from `www.salt.ac.za` (2014)

[5] E. Hecht, *Optics*, Addison Wesley, San Francisco, Fourth Edition (2002)

[6] J. Hardy, *Adaptive Optics for Astronomical Telescopes*, Oxford University Press, New York (1998)

[7] C. R. Kitchin, *Astrophysical Techniques*, CRC Press, Boca Raton, Fifth Edition (2009)

[8] A. N. Cox, *Astrophysical Quantities*, Springer, New York, Fourth Edition (2000)

[9] *The Intrinsic Seeing Quality at the WHT Site*. Retrieved July 5 2014, from `www.ing.iac.es/Astronomy/development/hap/dimm.html` (1994)

[10] J. Vernin and C. Muñoz-Tuñón, *Optical seeing at La Palma Observatory; II. Intensive site testing campaign at the Nordic Optical Telescope*, Astronomy and Astrophysics 284 311-318 (1994)

[11] *SIMBAD Astronomical Database*. Retrieved July 15 2014, from `www.simbad.u-strasbg.fr/simbad/` (2014)

[12] J. L. Codona, *Theory and application of differential otf (dotf) wavefront sensing*, Proc. SPIE 8447, 84476P (2012)

[13] J. L. Codona and N. Doble, *Experimental evaluation of differential OTF (dOTF) wavefront sensing*, Proc. SPIE 8447, 84476R (2012)

[14] J. L. Codona, *Differential optical transfer function wavefront sensing*, Optical Engineering Vol. 52(9) 097105 (2013)

[15] V. Korkiakoski, N. Doelman, J. L. Codona, M. Kenworthy, G. Otten and C. Keller, *Calibrating a high-resolution wavefront corrector with a static focal-plane camera*, Applied Optics Vol. 52 No. 31 (2013)